



EOM-3901
Master's Thesis in
Energy and Environment in the North

**Marine Target Characteristics in
Satellite SAR Imagery**

Stine Skrunes

February, 2011

FACULTY OF SCIENCE AND TECHNOLOGY
Department of Physics and Technology
University of Tromsø



EOM-3901
Master's Thesis in
Energy and Environment in the North

**Marine Target Characteristics in
Satellite SAR Imagery**

Stine Skrunes

February, 2011

FACULTY OF SCIENCE AND TECHNOLOGY
Department of Physics and Technology
University of Tromsø

Abstract

In this thesis, marine targets in Synthetic Aperture Radar (SAR) imagery are studied. The aim is to evaluate how different marine targets appear in different polarization channels, to investigate their scattering behaviour, and to study their contrast measures and geometric properties. RADARSAT-2 data containing ships, oil rigs and icebergs in ocean and/or sea ice background are evaluated with corresponding auxiliary data.

To be able to detect a target in a SAR image, a significant contrast between target and background is needed. In this thesis, peak-to-background ratios (PBR) and target-to-background ratios (TBR) are used to evaluate the contrasts for different target types and background classes. The relations between contrast measures and incidence angle, target size and weather conditions are addressed.

In order to track, identify or classify targets, reasonable features for discrimination must be chosen. In this project, Hu's 1st geometric moment is used as a geometric feature to investigate the elongatedness of the targets.

It is found that cross-polarization ($|S_{HV}|$ and $|S_{VH}|$) gives better contrast than co-polarization ($|S_{HH}|$ and $|S_{VV}|$), especially at low incidence angles. Where quad-polarimetric data is available, enhanced contrast can be obtained through polarimetric decompositions. Pauli decomposition components can be directly related to physical properties of the targets, and it is seen that for man-made targets, the contrasts are dominated by the volume scattering and double bounce components, i.e. $|S_{HV} + S_{VH}|$ and $|S_{HH} - S_{VV}|$.

For man-made targets in ocean background, the contrast increase with incidence angle for co-polarization channels and $|S_{HH} + S_{VV}|$, probably due to lower ocean clutter levels, while a decrease is seen in PBR for cross-polarization channels and $|S_{HV} + S_{VH}|$. The contrast measures also seem to increase with target size, especially for cross-polarization and PBR. In the case of ocean background, an indication of degraded contrast for higher wind speeds is seen.

Comparison of contrasts for different target types show that PBR is larger for man-made targets in sea ice than in ocean areas, while the opposite is seen for TBR. Comparison of man-made targets versus icebergs shows that the latter have highest mean PBR while man-made targets have highest mean TBR. Ships in sea ice have higher contrasts than icebergs in both PBR and TBR. More data would provide more reliable results and a more accurate comparison.

It is seen that Hu's 1st moment may be a useful feature for distinguishing between small and large ships, or between larger ships and other target types.

Acknowledgement

First of all, I would like to thank my supervisor, Associate professor Camilla Brekke, for giving me an interesting project to work on, and for supporting me throughout the project work. Thank you for reading my thesis countless times, for giving me lots of feedback and advice, and for being a source of inspiration.

I also want to thank Professor Torbjørn Eltoft for being co-supervisor for the pilot study, and for looking through my thesis.

I want to thank Kongsberg Satellite Services for providing the SAR data, and Silje Eriksen Holmen at the Norwegian Meteorological Institute for supplying the weather data.

Thanks to my family for their motivation and belief in me, and for always supporting my decisions in all aspects of life. A big thanks also to all my friends and my fellow students for making every day better.

Finally, I want to thank my dear Håvard for his help and advice, and for reading through my thesis. Thank you for your patience, support and encouragement, and for always making me smile.

Stine Skrunes
Tromsø, February 2011

Contents

List of Abbreviations	ix
1 Introduction	1
1.1 Aim of project	2
1.2 Summary of thesis	2
1.3 Organization of report	2
2 SAR theory	5
2.1 Radar basics	5
2.1.1 Geometry of a SAR system	6
2.1.2 Range resolution of SAR	6
2.1.3 Azimuth resolution of SAR	7
2.2 Speckle	8
2.2.1 Multi-looking	8
2.3 Polarization	9
2.4 Scattering	10
2.4.1 Volume scattering	10
2.4.2 Surface Scattering	10
2.4.3 Bragg scattering	11
2.4.4 Double- and even-bounce scattering	12
2.5 Polarimetric decompositions	12
3 SAR application: marine environments	15
3.1 SAR imaging of ocean areas	15
3.2 SAR imaging of ships	18
3.2.1 Research on ship contrasts	21
3.3 SAR imaging of sea ice	24
3.4 SAR imaging of icebergs	27
3.5 Discrimination between icebergs and ships	29
4 Methods	31
4.1 Polarimetric decompositions	31
4.1.1 Pauli decomposition	31
4.1.2 Interpretation of Pauli decomposition	32
4.1.3 The Pauli image	32
4.1.4 Entropy and anisotropy	33
4.2 Semi-automatic target detection	34
4.2.1 Segmentation of small targets	34

4.2.2	Segmentation of large targets	36
4.3	Calibration	36
4.4	Calculation of incidence angles	38
4.5	Ground range correction	38
4.6	Contrast measures	39
4.6.1	Peak-to-background ratios in the pilot study	41
4.6.2	Peak-to-background ratios in the current project	41
4.6.3	Target-to-background ratios	42
4.7	Geometric measures	42
4.7.1	Basic region descriptors	42
4.7.2	Ship length estimation	44
4.7.3	Moments	44
4.8	Other relevant methods	46
4.8.1	Total Degree of Rotation	46
4.8.2	Symmetric Scattering Characterization Method	47
5	Data	49
5.1	RADARSAT-2	49
5.2	Automatic Identification System	50
5.3	Data set 1: Man-made targets in ocean background	51
5.3.1	AIS data	53
5.3.2	Weather data	54
5.4	Data set 2: Ships in sea ice background	57
5.4.1	Ground truth data	57
5.4.2	Weather data	58
5.5	Data set 3: Iceberg targets in mixed background	59
5.5.1	Weather data	62
6	Results and discussions	63
6.1	Results from the pilot study	63
6.2	Contrast characteristics	64
6.2.1	Data set 1: Man-made targets in ocean background	64
6.2.2	Data set 2: Ships in sea ice background	86
6.2.3	Data set 3: Iceberg targets in mixed background	94
6.2.4	Comparison of the data sets	103
6.3	Geometric characteristics	105
7	Conclusions	107
7.1	Future work	109
	Appendices	113
	A Segmentation parameters	113
	B Image details	115
	C Results of method from pilot study	121
	D Results based on amplitude images	125

Bibliography	125
List of Figures	131
List of Tables	134

List of Abbreviations

AIS	Automatic Identification System
AP	Alternating Polarization
ASAR	Advanced Synthetic Aperture Radar
CFAR	Constant False Alarm Rate
FYI	Firstyear Ice
HH	Horizontal transmit, Horizontal receive polarization
HV	Horizontal transmit, Vertical receive polarization
KSAT	Kongsberg Satellite Services
MYI	Multiyear Ice
PBR	Peak-to-Background Ratio
RCS	Radar Cross Section
RGB	Red Green Blue
SAR	Synthetic Aperture Radar
SLC	Single Look Complex
TBR	Target-to-Background Ratio
TCR	Target-to-Clutter Ratio
VH	Vertical transmit, Horizontal receive polarization
VV	Vertical transmit, Vertical receive polarization

Chapter 1

Introduction

Surveillance of marine environments is an important application of Synthetic Aperture Radar (SAR). Fisheries and pollution control, and ship traffic monitoring for marine safety and security reasons are some areas of interest. With increasing activity in ice-infested waters, e.g. due to the opening up of the North East and North West Passages, monitoring of sea ice and icebergs is also getting more important, as sea ice can pose a threat for shipping and fishing vessels, and for other coastal and offshore constructions and operations.

Areas at high latitudes are covered in darkness large parts of the year, and often also by clouds. SAR provides its own illumination source, and can penetrate clouds and most precipitation, making this sensor an important tool for obtaining information in these areas, independent of weather and lighting conditions. With new SAR sensors like RADARSAT-2, ALOS PalSAR and TerraSAR-X, advanced image modes with dual-polarization and quad-polarimetry, high resolution and large flexibility in imaging geometry are now available, permitting a better characterization of illuminated targets. The data used in this project are obtained with RADARSAT-2, one of the most advanced spaceborne C-band SARs available.

In SAR images, man-made targets such as ships and oil rigs appear as bright areas towards a darker background, with the background brightness depending on its composition, e.g. ocean or sea ice. Icebergs will also appear bright compared to its background, and when comparable in size to ships, they may be difficult to distinguish from man-made targets.

Significant contrast between target and background is necessary to make *detection* and *segmentation* possible. In this project, contrast measures in form of peak-to-background ratios (PBR) and target-to-background ratios (TBR) are evaluated. Different polarization channels and Pauli decomposition components are investigated in order to describe the scattering mechanisms of the targets, and to identify the polarization options which will maximize target contrast. The dependency of target contrast on incidence angle, target size and weather conditions are addressed.

In order to *track*, *identify* or *classify* targets, we must select reasonable features for characterization. Several features proposed in the literature for target characterization are described in this thesis, e.g. geometric measures. Geometric measures in form of Hu's 1st geometric moment, which provide an elongatedness measure, are calculated and compared for different target types.

1.1 Aim of project

The overall goal of this project is to study marine target characteristics in satellite SAR imagery. The specific aim of the thesis is to evaluate how marine targets such as ships, oil rigs and icebergs appear in the different polarization channels, to investigate the scattering behaviour of those targets, to evaluate how PBR and TBR are affected by incidence angle, target size and weather conditions, and to study their geometric properties. Three RADARSAT-2 data sets with marine targets and ground truth information are studied:

- Quad-polarimetric data containing man-made targets in ocean background, acquired at the Norne field on the Norwegian coast.
- Dual-polarimetric data, $|S_{VV}|$ and $|S_{VH}|$, of ships in sea ice, acquired east of Svalbard.
- Single-polarization data, $|S_{HH}|$ or $|S_{HV}|$, of icebergs, acquired over Antarctica.

Corresponding ground truth information available for the different data sets, including weather data, are used during interpretation.

1.2 Summary of thesis

The main elements of the project work are:

- Literature study on backscatter properties of different marine features, and methods used for target characterization.
- Semi-automatic detection and segmentation of targets from the data sets.
- Calculation of contrast measures and geometric measures for selected targets.
- Investigation of backscatter response with respect to polarization, incidence angle, target size and weather conditions.
- Comparison of contrast measures and geometric measures with respect to target type and background classes.

1.3 Organization of report

This report starts with a theoretical part, composed of chapter 2 and 3. Chapter 2 describes basic radar properties, including geometry, resolution, speckle and polarization. It also describes different types of scattering. Chapter 3 concerns SAR imaging of the marine environment including ocean areas, ships, sea ice and icebergs, and their respective scattering properties. It also summarizes some research done on ship-sea contrast and discrimination between icebergs and ships.

Chapter 4 describes the methods applied in the experimental part of this project, and some related methods on marine target characterization. Chapter

5 describes the data used in the experimental part, both SAR data and corresponding auxiliary data. A discussion of the results are given in chapter 6. Chapter 7 concludes the thesis and some areas for future work are suggested.

Chapter 2

SAR theory

SAR is an active, imaging microwave sensor, meaning it both transmits microwaves and records the backscattered signal, making a two-dimensional image of the ground. High resolution SAR was developed in the 1950s for military purposes, and became commercially available in the 1960s [27].

As the microwave radiation can penetrate clouds and most weather conditions, images can be obtained in all weather, both day and night. This property makes SAR very suitable for imaging in the North, where the weather and lighting conditions are not the best.

Many satellites carrying a SAR instrument follow a near-polar orbit. This is an orbit in north-south direction, with an inclination relative to a line between the North and the South pole. As the Earth rotates, this orbit allows the satellite to cover most of the Earth's surface in a certain amount of time. The satellite will pass the areas furthest to the north and south more often than areas closer to Equator, which is another reason for using these remote sensing systems at high latitudes. Some of the applications for SAR data are geological mapping, monitoring of snow cover, sea ice identification, ship detection, slick detection, vegetation mapping and crop condition monitoring [27].

This chapter will describe the basic properties of a radar, including SAR geometry, resolution, speckle, polarization, polarimetric decompositions and the different scattering mechanisms.

2.1 Radar basics

A RADAR (RADio Detection And Ranging) consists of a transmitter, a receiver, an antenna and an electronics system. The transmitter generates short pulses of microwaves that is focused by the antenna, making a beam which illuminates the surface at an oblique angle, perpendicular to the direction of movement. Some of the reflected energy is received at the antenna, and as it moves, a 2D image of the surface is made. The time delay between transmitted and received signal can be used to compute the distance (range) to the surface and targets [27].

The microwave part of the electromagnetic spectrum spans from ca 1 mm to 1 m, or from 3×10^8 to 3×10^{11} Hz [21]. It is divided into several frequency bands, called X-band, S-band etc. The data used in this project are images from RADARSAT-2, using C-band with a frequency of 5,405 GHz.

2.1.1 Geometry of a SAR system

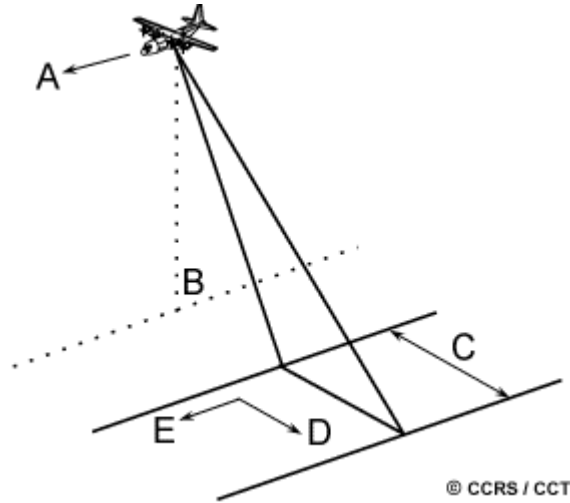


Figure 2.1: Geometry of a radar, where A-E indicates flight direction, nadir, swath width, range direction and azimuth direction respectively (figure from [27]).

In figure 2.1, we can see the geometry of a radar system (here illustrated with an airplane, but the principle is the same for satellites). The satellite with the platform travels in flight direction (A), and the point directly below the platform is called nadir (B). The microwave signal is transmitted obliquely in a direction perpendicular to flight direction, illuminating the swath (C). The across-track direction perpendicular to the flight direction is called range (D), and the along-track direction parallel to flight direction is called azimuth (E). The part of the swath closest to nadir is the near range, and the part of the swath farthest away from nadir is the far range. In figure 2.2, some more geometric concepts are illustrated. The angle between the radar beam and the normal to the ground surface, is called the incidence angle (A). The angle at which the radar looks at the surface is the look angle (B). The radar measures the distance to a target along the line of sight, called the slant range distance (C), while the true horizontal distance is called the ground range distance (D) [27].

2.1.2 Range resolution of SAR

Range resolution is the minimum distance two points on the ground can have between them in range direction, and still be separated by the sensor [10]. Two points can be distinguished if the pulse echo from the most distant point arrives later than the pulse echo from the nearest point [8]. The ground range resolution is given by

$$R_{rg} = \frac{c\tau}{2\sin\phi} \quad (2.1)$$

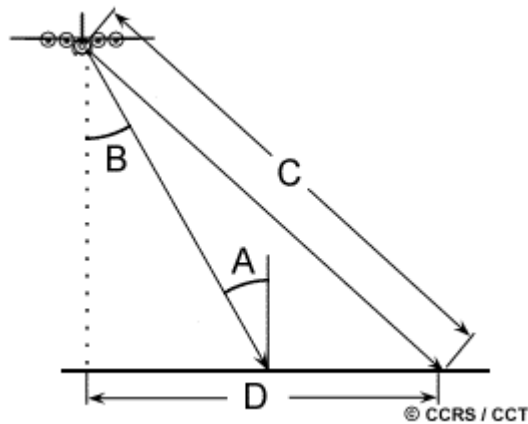


Figure 2.2: Geometry of a radar, where A-D indicates incident angle, look angle, slant range distance and ground range distance respectively (figure from [27]).

where R_{rg} is the range resolution, c is the speed of light, τ is the pulse length and ϕ is the look angle [21]. From this we see that the resolution can be enhanced by decreasing the pulse length. This would however demand more energy [21]. It could also give too small signal-to-noise ratio [8], i.e. the signal would be too weak compared to the amount of noise. To obtain a satisfactory resolution, a chirp signal is used instead of a cosine signal. By doing this, the effective pulse length is reduced from microseconds to nanoseconds, improving the resolution. Hence, the range resolution is determined by the type of pulse coding and the processing of the returned signal, which is done the same way in both conventional systems and in SAR. SAR is however distinguished from other systems by a better resolution in azimuth direction, as described in the next section [8].

2.1.3 Azimuth resolution of SAR

Azimuth resolution corresponds to the minimum separable distance between two points along an azimuth line, and is equal to the radar beam width W [10]. This means that two objects on the ground can only be resolved if they are not in the radar beam at the same time [8]. For a real aperture radar the resolution is given by

$$R_{az} = W = \frac{Z\lambda}{L} \quad (2.2)$$

where W is the beam width, Z is the slant range distance to the object, λ is the wavelength and L is the length of the antenna. As the resolution depends on the distance to the object, a satellite platform would not give a very good resolution. A better resolution could be obtained by a longer antenna, but that would involve several problems, e.g. difficulties in deploying in space.

In SAR, a longer antenna is synthesized by sending out many short pulses [21]. These will hit the target at slightly different angles with respect to the

moving radar, giving different Doppler frequency shifts. The Doppler shift is given as

$$v_d = v' - v \quad (2.3)$$

where v_d is the Doppler shift, v is the frequency of the radiation source and v' is the frequency of the signal received by the observer [10].

From a target first enters the beam, and until it leaves, echo pulses will be recorded by the moving satellite, and the synthesized antenna will have a length B as shown in figure 2.3. The SAR azimuth resolution, R_{az} , is given as

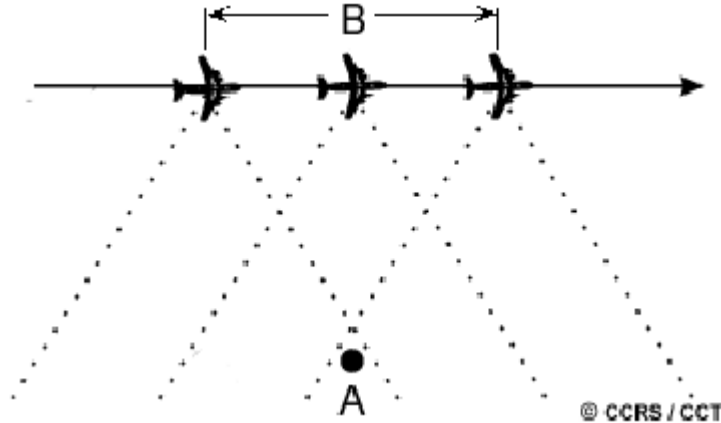


Figure 2.3: Echo pulses from target A is recorded by the moving antenna as long as the target is within the radar beam, and the synthesized antenna length is given by B (figure from [27]).

$$R_{az} = \frac{L}{2} \quad (2.4)$$

As R_{az} now only depends on the length of the antenna, a better resolution is obtained, improving as the length of the antenna decreases [21].

2.2 Speckle

Speckle is grainy salt-and-pepper noise, present in SAR images due to the coherent nature of the radar wave. Constructive and destructive interference between the many scattering events within one resolution cell cause random bright and dark areas in the radar image. The amount of speckle is often a problem in SAR data interpretation [18].

2.2.1 Multi-looking

Speckle can give rise to poor contrast between a target and its background, but can be reduced by processing separate portions of an aperture individually, and

recombine these portions afterwards. This is called multi-looking. Multi-looking of the data reduce the noise, but at the cost of degraded resolution. During multi-looking, an averaging takes place, and the azimuth resolution, $R_{az,ml}$ becomes

$$R_{az,ml} = \frac{L}{2}(\#looks) \quad (2.5)$$

where $\#looks$ is the number of looks used in the multi-looking [18].

Single Look Complex (SLC) data without any multi-looking, are used in the experimental part of this study (described in chapter 5).

2.3 Polarization

An electromagnetic wave has one electric field component and one magnetic field component. The term polarization refers to the orientation of the electric field. The signal transmitted by a radar is either horizontal (H) or vertical (V) oriented, as illustrated in figure 2.4. The same applies for the received backscatter signal.

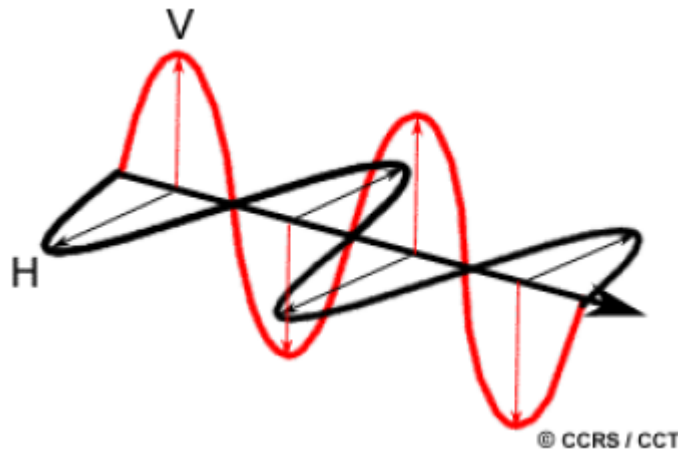


Figure 2.4: Horizontal (H) and vertical (V) polarization (figure from [27]).

We have four combinations of transmitted and received signal: HH, HV, VH and VV. In this report, the first letter describes the polarization of the transmitted signal, and the second letter describes the polarization of the received signal. The combinations HH and VV are called like-polarized or co-polarized, while VH and HV are referred to as cross-polarized.

The polarization affects how a radar "sees" a surface, as different polarizations interact in different ways with objects and surfaces, and produce various types of backscattering. Different polarizations can provide different information, and complement each other.

Some radars can only transmit in either horizontal or vertical direction, and also receive only one polarization. These are called single-polarization radars. Dual-polarization radars can provide the combinations (HH,HV), (VV,VH)

or (HH,VV). Polarimetric radars can transmit and receive in both horizontal and vertical direction, providing all four combinations HH, HV, VH and VV [27]. These are called full-polarimetric or quad-polarimetric radars. Multi- and quad-polarimetric radars have become more common and can be found in e.g. RADARSAT-2, Envisat Advanced Synthetic Aperture Radar (ASAR), TERRASAR-X, CosmoSkyMed and Alos PalSAR. As the different polarization channels are sensitive to different properties of the surface, quad-polarimetric data can improve detection and discrimination of targets.

2.4 Scattering

In active remote sensing, a microwave signal is sent out, and the reflected (backscattered) signal that reaches the satellite is recorded. There are different types of scattering mechanisms, depending on the surface or target the transmitted signal interacts with. Some factors that will influence the backscattered signal are the incidence angle, wavelength and polarization of the radar, geometry and roughness of the surface, and size, structure and movement of targets. Some main types of scattering are discussed in the following sections.

2.4.1 Volume scattering

Volume scattering is a type of scattering that arise when the transmitted signal is able to penetrate through a surface and into the media, as shown in figure 2.5. The scattering is a result of many scattering events within the media, e.g. in dense vegetation and dry snow. The backscatter will depend on the density of the media, geometry of the elements within and on the moisture content. Volume scattering can both increase and decrease the brightness in the image, depending on how much of the energy is being scattered out of the volume and back to the radar [27] [43].

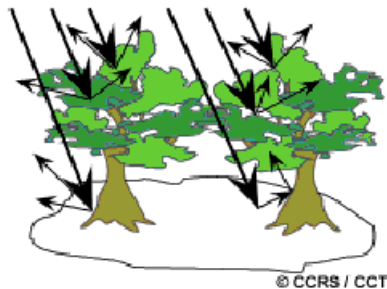


Figure 2.5: Volume scattering (figure from [27]).

2.4.2 Surface Scattering

Surface scattering occurs at the boundary between two homogeneous media, such as lakes, oceans and bare soil. The scattering is a function of moisture content (reflectivity increases as moisture increases) and roughness of the surface.

Roughness is the average height variations of the surface cover compared to the wavelength of the radar. Hence, different satellites will see different surfaces as smooth and rough, depending on their wavelength and incidence angle. For smooth surfaces, e.g. a calm water body, we get a specular reflection, where very little energy is sent back to the satellite. For a rough surface, the reflected energy goes in many different directions, depending on the orientation of the reflecting surfaces. This is called diffuse scattering. A perfect diffuse reflector, where the radiant flux leaving the surface is constant in all directions, is called a Lambertian surface [18]. From rough surfaces, more energy is backscattered to the satellite, as illustrated in figure 2.6. Because of this, rough surfaces appear brighter than smooth surfaces in SAR images [27] [43].

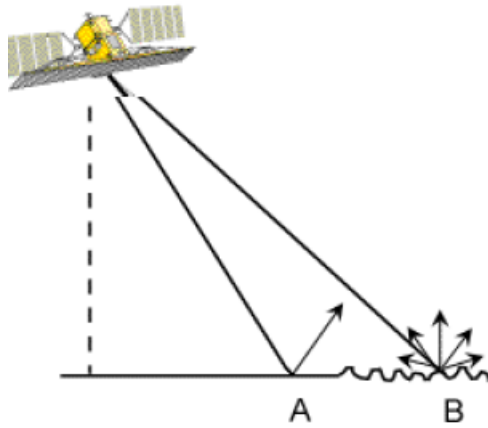


Figure 2.6: Surface scattering from a smooth surface (A) and a rough surface (B) (figure from [43]).

2.4.3 Bragg scattering

For slightly rough surfaces of a homogeneous medium (no volume scattering), with a root mean square (rms) height variation less than $\lambda/8$, the scattering can be described by the Bragg model. This model states that the backscattered energy will be dominated by the surface spectral components that resonate with the incident wave [8].

Bragg models are most often used for describing scattering from sea surfaces, which is exclusively surface scattering. On the ocean surface we have both short and longer waves present, but due to the height variation limitation of the model ($< \lambda/8$), only small capillary waves (length ~ 2 cm) or short gravity waves (length ~ 50 cm) exhibit Bragg resonance. The Bragg wavelength λ_s of the ocean resulting in Bragg resonance is given by

$$\lambda_s = \frac{\delta \lambda_r}{2 \sin \theta} \quad (2.6)$$

where δ is the order of resonance, λ_r is the radar wavelength and θ is the incidence angle. This formula assumes that the travel direction of ocean waves is in the radar line of sight [7].

By using the Bragg model, wave direction, wavelength and wave height can be measured. This information can be used in ocean wave forecast models and global climatology [8].

2.4.4 Double- and even-bounce scattering

If a feature has two (or more) perpendicular surfaces we get a corner reflection. Two perpendicular surfaces will give us double- or even-bounce scattering, as illustrated in figure 2.7, where a large amount of energy is reflected back to the satellite, producing bright areas in the SAR image. Ships on water and urban areas with man-made structures such as buildings, streets and bridges, can produce this type of scattering [27][43].

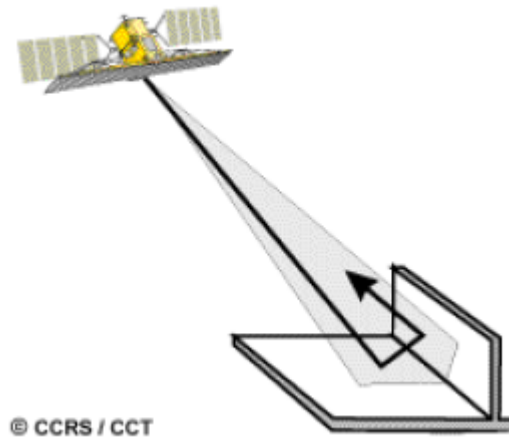


Figure 2.7: Double bounce scattering (figure from [27]).

Two perpendicular surfaces, as in figure 2.7 is called a dihedral. If we have three perpendicular surfaces, it is called a trihedral.

2.5 Polarimetric decompositions

For quad-polarimetric data, a scattering matrix S , also called the Sinclair matrix, can be constructed:

$$S = \begin{bmatrix} S_{HH} & S_{HV} \\ S_{VH} & S_{VV} \end{bmatrix} \quad (2.7)$$

The four elements of S are complex images, and are obtained from the magnitudes and phases measured by the radar. For many targets, particularly natural targets, the reciprocity theorem assumes that $S_{HV} = S_{VH}$. However, it is observed that this is not always true for ships. A possible reason for this can be reflections from sharp edges and corners [24].

The scattering matrix S can characterize the scattering process from a target, and hence the target itself. A decomposition of the scattering matrix can be

done, with the objective of expressing the measured matrix as a sum of scattering responses of simpler objects. This can be written as

$$S = \sum_{i=1}^k w_i S_i \quad (2.8)$$

where S_i is the scattering response of the k simpler objects, and w_i is the weight of this scattering. Only some sets of S_i are useful for interpreting the information in S . Examples of decompositions are Pauli, Krogager and Cameron decompositions [11]. The Pauli decomposition is described in more detail in chapter 4. Describing the Krogager and Cameron decompositions is beyond the scope of this report.

Chapter 3

SAR application: marine environments

Remote sensing of marine environments and marine targets are useful for many applications. For maritime safety, SAR is used in cost-effective traffic control, validating Automatic Identification System (AIS) information and for locating vessels which are not providing AIS. Other applications are fisheries control and pollution control. Detection of possible oil spills and indication of pollution sources are important applications for SAR. SAR is also used for maritime security reasons, e.g. anti-terrorism, anti-piracy, border surveillance and in revealing illegal immigration and smuggling [13].

Monitoring of ship traffic and sea ice, and discrimination between these, are important when operating at high latitudes, both in the Northern and Southern Hemisphere, for environmental, economical, health and security reasons. Sea ice is an important factor in shipping and fishing industries, as well as in construction operations and climate change studies. Ice floes, icebergs and pack ice can be barriers for navigation of ships, as most ships and fishing vessels cannot penetrate ice. Also, landfast ice can be a barrier for reaching a port. Offshore platforms and harbours on the coast require stronger construction in ice-infested waters. Sea ice monitoring and forecasts are hence of primary importance. Satellite images can provide us with information about ice type, concentration and movement, and help locating the best navigation routes, or cracks in the ice called leads. Lately, SAR has been established as a main data source for ice monitoring in several countries [46] [25].

The scattering mechanisms and SAR appearance of ocean, ships, sea ice and icebergs are described in this chapter. A summary of some research done on discrimination between ships and icebergs are also included.

3.1 SAR imaging of ocean areas

SAR imaging of oceans is used in many applications, e.g. for wind observations and weather forecasts. In this project we are looking at different marine targets and their appearance in SAR images, and as ocean areas often compose the background, it is also important to know how the sea surface are imaged by SAR.

The backscattering from ocean areas depends on how the transmitted signal interacts with the surface. It hence depends on surface characteristics, e.g. roughness and dielectric constant, but also on the radar properties such as frequency, polarization and viewing geometry.

Water has high dielectric constant, and therefore low penetration depth. It reflects microwaves very well, resulting in low backscattering and dark images. As SAR only penetrates the topmost layer of an ocean surface, we can only see the underlying features if they interact with and modulate the surface wave field [22].

As described in section 2.4.2, the sensors impression of surface roughness depends on the height variations of the surface compared to the radar wavelength. Smooth surfaces produce specular reflection and low backscatter. Therefore, some wind is needed to be able to see the surface characteristics, and the backscatter increase with increasing wind speed as this roughens the sea surface. For a given radar and incidence angle, the dependency of radar backscatter on wind speed, u_s , is given by

$$\sigma^0 \sim |u_s|^\gamma \quad (3.1)$$

where σ^0 is the normalized radar cross section and γ is a function of the radar parameters. The ocean backscattering will be largest when the wind direction is towards the radar, and smallest when the wind direction is across the radar look direction [7].

An example of how ocean areas can look in a SAR image is seen in figure 3.1. This is an Envisat ASAR image of the Norne field from September 2003 in HH-polarization.

For incidence angles above 20° , Bragg resonance is the dominating mechanism for surface scattering. As most operational SAR systems operate at incidence angles above 20° (note that rough seas can affect local incidence angle), the Bragg model usually applies. This model is described in section 2.4.3. From equation 2.6, we see that the Bragg wavelengths are affected by the radar wavelength and incidence angle, and these will in turn affect the backscatter σ^0 [7]. Many studies have revealed that ocean backscattering will decrease with increasing incidence angle, especially in co-polarization. Cross-polarizations have lower sea clutter levels than co-polarization, and in some cases this level can be at the instrument noise floor. The ocean backscatter will decrease with increasing radar frequency [56] [7].

Ocean reflectivity is also affected by polarization. VV polarization usually reflects more than HH, and the difference depends on incidence angle. The decrease in backscatter when incidence angle increase is faster for HH than for VV for a C-band SAR [7] [3].

Figure 3.2 illustrates how ocean backscatter decrease with incidence angle for co-polarization in different wind strengths. The plot is based on the CMOD (C-band Scatterometer Model Function) model for backscattering.

In SAR images of ocean areas, many processes and features can be seen, such as atmospheric winds and storm fronts, heavy rain, ocean swell, breaking waves, bottom topography, man-made and natural slicks and films, sea ice, ships and wakes, islands, oil rigs, shoals etc. Some of these can have similar appearance, and be difficult to discriminate, e.g. can icebergs, oil rigs, breaking waves and islands cause false alarms during ship detection [7].

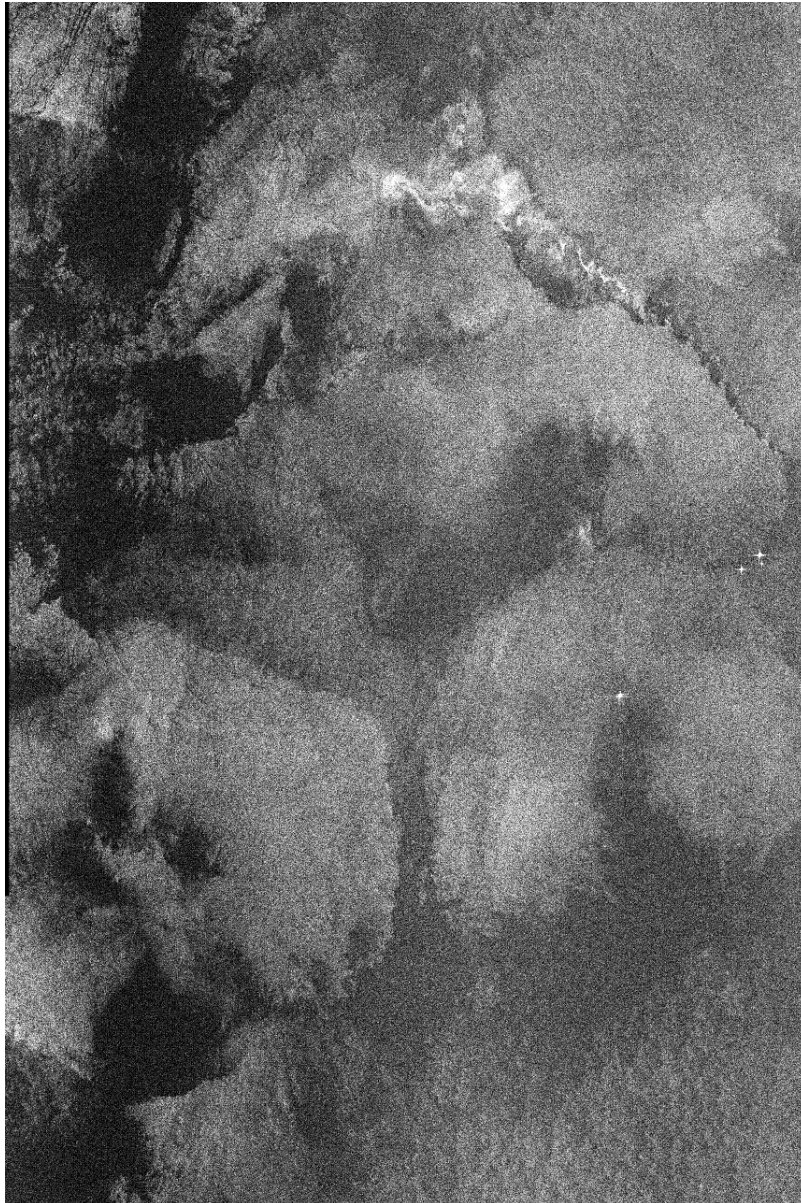


Figure 3.1: Envisat ASAR, HH-polarization image of the Norne field in September 2003. To the right, some ships and oil rigs can be seen. Several meteorological and oceanographic phenomena are also visible (figure from [2]).

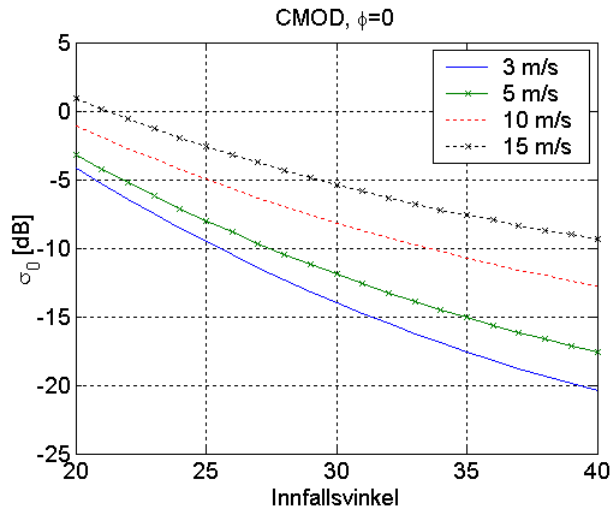


Figure 3.2: Radar backscatter from ocean areas as function of incidence angle, calculated with CMOD (C-band, VV) for various wind strengths. The radar looks straight into the wind (figure from [2]).

The non-homogeneous nature of the sea can also complicate interpretation of SAR images of ocean areas. Regions with different wind conditions, effects from land areas, bathymetry, ship wakes etc. can result in variations in the ocean backscattering that need to be considered. These variations can be seen in figure 3.1. Because of this, segmentation based on local background measures and thresholds is better than using global metrics for the whole image [7].

3.2 SAR imaging of ships

Ship detection is interesting for maritime security reasons, for monitoring of fishery and ship traffic, and in pollution applications. In SAR images, ships will appear as small, bright areas, towards a darker background. Ship parameters extractable from SAR images include position, heading, speed, dimensions and ship type, to a varying degree [22]. The backscattering depends on several properties such as the structure of the ship, its orientation relative to the radar, size and motion.

The ship structure may have varying degrees of complexity, and give both even and odd number of reflections from surfaces, corners, edges, cables and the ship-sea configuration [24] [13], often showing a scattering combination of dihedral and trihedral surface scattering [14]. If the ship is in motion, this can give distortions and displacement in azimuth direction. When a wake is present in the image, this will act as a reference for the real position [22]. Wakes can also be used as a basis for ship detection.

Many studies have been done on ship detection, discussing what parameters are affecting the ship-sea contrast. The Radar Cross Section (RCS), σ , will increase with ship size, freeboard and amount of metal structure [13]. Whether the vessel is laden or unladen may also be relevant. Fully laden ships will sit

lower in the water, reducing the RCS. A ship travelling in azimuth direction will have higher backscatter compared to other travel directions [7].

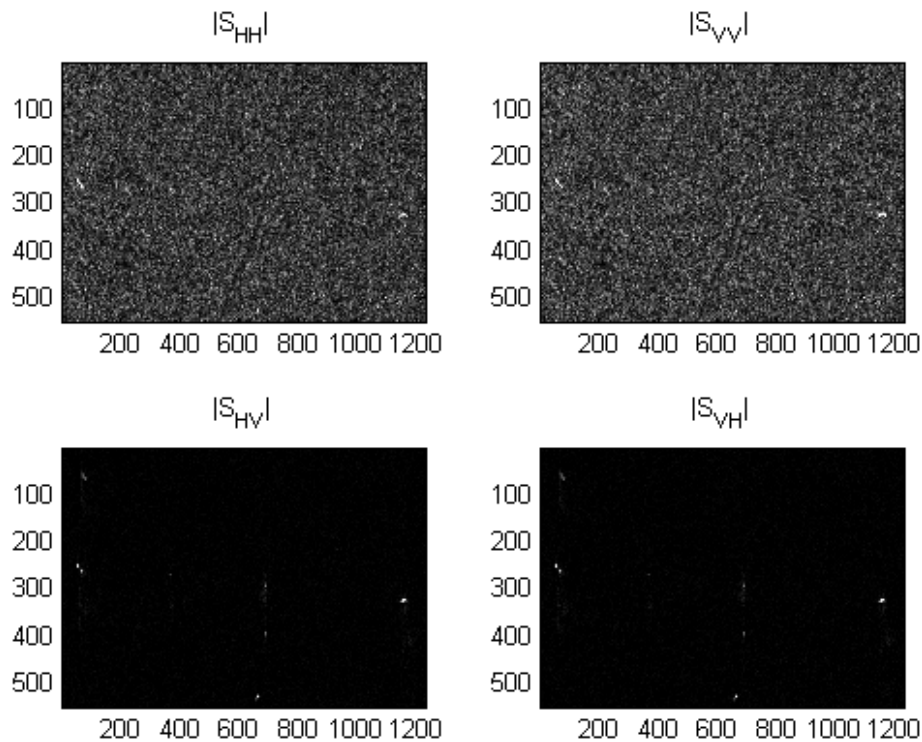


Figure 3.3: RADARSAT-2 image of ships in different polarizations (figure from [50]).

In addition to the target related variables mentioned above, ship-sea contrast depends on environmental parameters, e.g. sea state, and on sensor parameters such as resolution, incidence angle, polarization and frequency.

Sea clutter increases with wind speed, swell and air-sea temperature instability, reducing the contrast between ship and ocean background. Out of these, wind speed seems to be most widely discussed. High wind speeds will increase sea clutter levels, and enhance azimuth blurring due to ship pitch and roll in high sea states [13]. The ocean clutter dependency of wind was described in section 3.1.

Concerning the sensor itself, ship backscatter is enhanced by higher frequency SAR, and the contrast increases with higher resolution [7]. Geometry between target, sensor, wind and waves can also affect the backscattering [13].

The dependency of ship-sea contrast on incidence angle and polarization have been widely discussed in the literature. For co-polarization, sea clutter is higher for steep incidence angles, so shallow angles will be better for ship detection. Sea clutter is higher for VV than for HH, so HH will provide the better contrast. Cross-polarization is preferable to co-polarization, as the sea clutter is even lower here, at least up to some incidence angle, where co-polarization contrast may surpass that of cross-polarization [7] [13]. Some research done on contrast

measures for ship targets, and dependency on incidence angle, polarization and other parameters are discussed in section 3.2.1.

Figure 3.3 is a figure from the pilot study done prior to the current project [50], and illustrates the difference between the polarization channels. It is seen that in the cross-polarized channels, the ships stand out from the background as white dots. In the co-polarized channels, the sea is very noisy and the contrast between ship and sea is low. Only a few of the ships can be seen here.

What radar parameters one prefers when obtaining SAR data depend on the objectives. For example are steep incidence angles and VV polarization not so good for ship detection, but are more sensitive to wake and oil spill imaging. Hence, the polarization channels can complement each other and provide more information when used together. The combination of HH and VV, or HV and VV under smaller incidence angles, is suitable for maritime surveillance as it can be used for both ship detection (in HH or HV) and for wake and oil spill imaging (in VV) [13].

The approach most widely used for ship detection is the Constant False Alarm Rate (CFAR). A Probability Density Function (PDF) for the clutter is estimated, and a threshold is set based on this. Possible targets are detected if they have values above the threshold. The threshold is chosen so that the percentage of background pixels lying above the threshold is constant, giving a constant false alarm rate. However, in practice, this condition is not always met. The simplest PDF is a Gaussian distribution, but a better and often used model for ocean clutter is the K -distribution [13]. The K -distribution has also been demonstrated to be a suitable model for sea ice in one-look intensity images of VV and VH polarization [5]. As the clutter levels varies within the image, the PDF and detection threshold should be determined locally, and a sliding window is therefore often used. The output of the detection process is a list of detected ship positions and corresponding attributes, e.g. estimated length, width, heading and RCS.

Even though SAR images can be used for detection, classification is difficult, and identification is essentially impossible. In some cases, the outline of the ship and the distribution of scatterers can be seen, on which classification can be based. The size can be used to distinguish some types of ships, e.g. fishing vessels from tankers and container ships. However, the outline is often not very well defined due to blurring, sea clutter etc. and a reliable length estimate is difficult to obtain [13].

As data is not continuously available, and has limited swath, resolution, detection and classification probability, ship detection results are more useful in combination with ship traffic data from other sources, such as AIS. Hence ships using AIS can be identified in SAR images, and vessels which are not sending AIS information can be located. The latter is interesting for maritime safety, military purposes and in controlling illegal fishing. Possible pollution sources can also be identified, if e.g. an oil spill is detected in the image.

Several new satellites provide quad-polarimetric images, giving rise to new possibilities. Quad-polarimetry can be helpful in discrimination between ships and false alarms, and polarimetric decompositions can identify different scattering types (see section 4.1.1). Based on quad-polarimetric data, the ship-sea contrast can be enhanced, and new features such as polarization entropy or anisotropy (described in section 4.1.4) can be used for ship detection [58] [52].

3.2.1 Research on ship contrasts

Contrast between ship and background have been evaluated in several studies, and identification of optimal polarization channels and incidence angles for contrast measures have been discussed. Findings from some studies are summarized in this section.

In Touzi (2000), polarimetric Convair-580 SAR data was investigated, and ship-sea contrast calculated for various ships at incidence angles between $45^\circ - 70^\circ$. HV polarization was found to produce better contrast than HH and VV at low incidence angles. At angles higher than 60° , HH gave the best results. Of HV, HH and VV, the latter gave the lowest contrast for all the range of angles considered [52].

In Touzi *et al.* (2001), the research was extended to include lower incidence angles (from 20°) and various wind conditions. Again, it was found that HV gave the best contrast at low incidence angles. At incidence angles above 55 degrees, HH gave best results, while VV still had the lowest contrast for the whole range of incidence angles evaluated. HV effectiveness was not degraded by rough sea conditions, for ships at 35° and 45° (from 7 knots to 20 knots). Phase differences was also evaluated for ship-sea discrimination, and of HH-VV, HH-HV and VV-VH, the first option was best, and also produced better ship-sea contrast than the HH and VV radiometric information. However, the HV component was more effective than the phase information [53].

In Jeremy *et al.* (2001), fully polarimetric C-band SAR imagery of ships from airborne platform were investigated. Target-to-clutter ratios (TCR) for the different channels were studied, and calculated as the ratio between the targets RCS, σ_T , normalized by the number of pixels in the RCS calculation, N , and the ocean clutter's mean RCS, σ_C^0 :

$$TCR_{Jeremy} = \frac{\sigma_T}{N\sigma_C^0}$$

It was found that HH was more optimal for ship detection for incidence angles $> 45^\circ$, while cross polarized data ($(VH + HV)/2$) was optimal for incidence angles $< 45^\circ$. VV was not as good as HH or cross-polarized data. Jeremy *et al.* also evaluated the Van Zyl and Cameron polarimetric decompositions, and the results indicated that polarimetric methods looked promising for ship detection, and also worked well at rejecting false alarms [58].

In Arnesen and Olsen (2004), Envisat ASAR Alternating Polarization (AP) data was investigated with respect to ship detection capabilities. TCR was evaluated as function of polarization, geometry and sea state. Contrasts for small ($\sim 18^\circ$), medium ($\sim 33^\circ$) and high ($\sim 41^\circ$) incidence angles were evaluated, and it was found that TCR increase with incidence angle for co-polarization, and decrease for cross-polarization. The data used was acquired under varying wind strength and sea state conditions, resulting in some scatter in the data [2]. 10 dB is considered the minimum contrast for ship detection in SAR data with more than three looks [1]. In this study, co-polarized data did not satisfy the criteria of 10 dB TCR for the smallest angles, while the cross-polarized TCR was above. The opposite was seen for the largest incidence angle. Also in Arnesen and Olsen (2004), it was seen that HH was preferable compared to VV, due to lower ocean backscatter. For both co-polarization channels, TCR increased with incidence angle, but decreased with wind speed and wave height. It was also

pointed out that the contrast near the edges (near and far range) can be lower due to instrument noise [2].

In Liu *et al.* (2005), ship detection performance using single-, dual- and quad-polarization SAR data from CV-580 was compared, and TCR compared for the different polarizations. Detection performance estimates in terms of false alarms and missed detections was made, clearly showing the advantage of the quad-polarimetric system, which gave the best results. Dual-channel with both amplitude and phase information performed better than dual-polarization with amplitude only, which in turn were better than single polarization results. Quad-polarimetric case with only amplitude was also considered, and performed very good. The dual-polarization system (HH,VV) with both amplitude and phase also performed good. One ship was imaged at two different incidence angles, 37° and 57° , with better detection performance at the highest incidence angle.

Of the single channels, HV and VH were better than the co-polarized channels for the lowest incidence angles (at 29° and 37°), both when looking at detection performance, and at the TCR values. At 42° , all four single-polarization channels had similar performance and TCR. At 57° , HH gave better results than VH and HV. The TCR for VV was lowest in all cases [23].

Vachon and Wolfe (2008) worked with validated ship signatures from Envisat ASAR AP mode data. Subscenes of 64×64 pixels were centered around maximum σ^0 , and the four 16×16 pixel corners were the basis for the clutter estimates. Several contrast metrics were used in this project, e.g. Peak-to-Clutter Ratio and Segmented Region RCS-to-Clutter Ratio, defined as

$$\text{Peak-to-Clutter Ratio} = \sigma_{max}^0 / \text{mean}(\sigma_{clut}^0)$$

$$\text{Segmented Region RCS-to-Clutter Ratio} = [SR_{RCS} / \text{mean}(\sigma_{clut}^0)] / SR_{area}$$

SR_{RCS} is the segmented region RCS, found by integrating σ^0 over the segmented target with the mean clutter removed. The segmented target region was constructed by taking out the pixels with $\sigma^0 > \text{mean}(\sigma_{clut}^0) + 5 \text{ std}(\sigma_{clut}^0)$ [56]. The method we are using in this project is similar to the one used by Vachon and Wolfe, and are described in chapter 4.

Vachon and Wolfe (2008) found that for co-polarization, the ship target contrast increases with increasing incidence angle, reflecting the decrease in ocean clutter. Cross-polarization contrast was more or less independent of incidence angle, as the clutter levels were at the instrument noise floor. It was concluded that co-polarization contrast was best for large incidence angles, while cross-polarization contrast was best for small angles. They found that the break point between co- and cross-polarization was around 33° , depending on ship size.

Vachon and Wolfe (2008) also discussed the contrast metrics versus ship length, and found that there was a general increase in contrast with ship length. The dependency on size was much clearer for the cross-polarization data, which also varied less [56]. Figure 3.4 summarize the findings of Vachon and Wolfe (2008). The dependency of contrast on incidence angle, ship length and polarization, and the fact that cross- and co-polarization is better for small and large incidence angles respectively, with a break-point around 33° , depending on size, is seen in this figure.

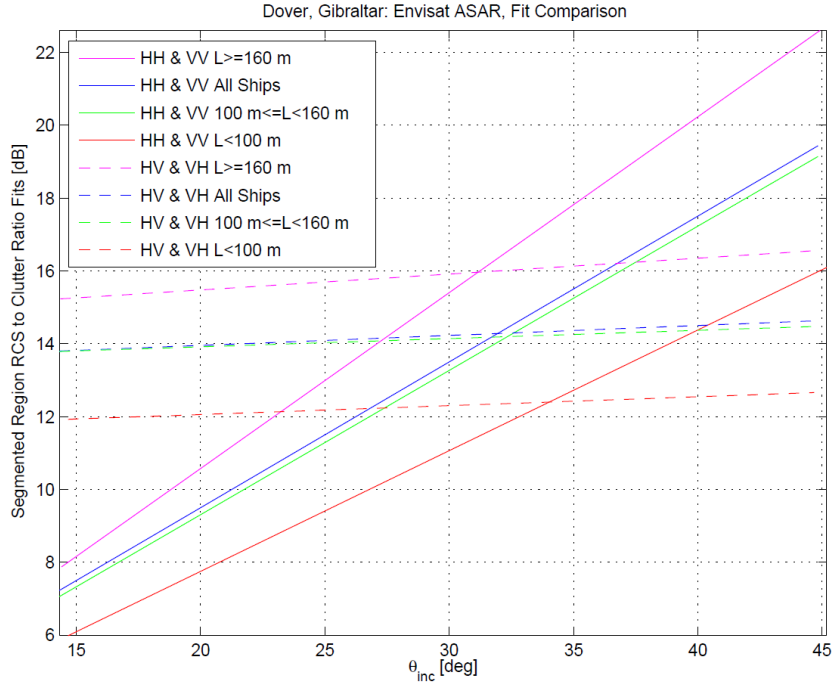


Figure 3.4: Summary of contrast measures as function of incidence angle and ship length for both co- and cross-polarization as found in Vachon and Wolfe (2008) (figure from [56]).

In Brekke and Anfinson (2010), a large fleet of fishing vessels in RADARSAT-2 images was analysed, and peak-to-clutter ratio as function of incidence angle and polarization was investigated. Peak-to-clutter ratio in small incidence angles of Wide-mode was compared to larger incidence angles in a ScanSAR narrow scene. For the smaller incidence angles, higher peak-to-clutter ratio was seen in HV than in HH. For larger angles, the situation was more mixed. For the largest angles, $34^\circ - 37^\circ$, all targets were above the threshold of 10 dB [5].

In Souyris *et al.* (2003), the possible enhancement of point target contrast by joint use of magnitude and phase in SAR images was discussed. The idea was to utilize the higher phase coherence of a vessel than the surrounding sea to enhance the vessel signature and to suppress the sea surface signature. During SAR acquisition, the variation in range between target and radar generate a Doppler effect in azimuth direction. If deriving the SLC image azimuth spectrum and extracting front- and rear-looks, a hard target (such as ships) contribution will remain unchanged in phase from one sublook to the other and have strong local complex correlation between sublooks. Front- and rear sublooks over extended targets on the other hand, are decorrelated. The sea surface decorrelates in a matter of only 3 msec.

Souyris *et al.* (2003) also introduced the internal Hermitian product (IHP), where both radiometric and phase behaviour is captured:

$$\rho_{herm} = \langle sub_1 \cdot sub_2^* \rangle$$

where sub_1 and sub_2 are the complex values associated with the front and rear look for a given pixel, and $\langle . \rangle$ is a spatial averaging in the vicinity of this pixel. The azimuth and range pre-whitened complex spectra were each divided into two; "azi-left", "azi-right", "rge-low" and "rge-high". After a spectra overlapping, four images corresponding to the azimuth-range spectrum combinations (azi-left,rge), (azi-right,rge), (azi,rge-low) and (azi,rge-high) are generated. The IHP between (azi-left,rge) and (azi-right,rge), ρ_{herm}^{azi} , and between (azi,rge-low) and (azi,rge-high), ρ_{herm}^{range} , were found and added incoherently. This adding is called the two-looks internal Hermitian product (2L-IHP). The results of the 2L-IHP on SAR images in Souyris *et al.* (2003) were critically reduced speckle, and clearly distinguishable targets. The 2L-IHP was also extended to quad-polarimetry [51].

3.3 SAR imaging of sea ice

When looking at the Earth's surface, 11 - 15% are covered by sea ice [3]. In the Northern Hemisphere, sea ice extent varies from a minimum in September to a maximum in March. In the Southern Hemisphere, fluctuations are even greater, from a minimum in February to a maximum in September. The mean thickness of Arctic and Antarctic sea ice is 3 m and 1-1,5 m respectively [46].

Sea ice has an impact on many important processes, e.g. the heat exchange between the ocean and atmosphere, the solar albedo of the ocean and the deep ocean circulation, and is hence an area of interest. Information about sea ice distribution and properties are needed for ship navigation, fisheries, oil and gas explorations and in climate research [3]. Sea ice have also been shown to be a problematic issue for ship detection in ice-infested waters [13].

As the large, sea ice covered regions in the Arctic and Antarctic are not easily accessible, data acquisition from space are very important. These areas are often cloud-covered, and during large parts of the year, also lay in darkness. Therefore, SAR has become the most important observational method. An example of a RADARSAT-1 image of sea ice is shown in figure 3.5.

Measurements of sea ice and its snow cover can be challenging due to large spatial and temporal variations. The many forms of sea ice, and the continuous modification of properties by ocean and atmosphere, makes sea ice a complex terrain. The backscatter signal depends on surface characteristics such as roughness and water content, on volume scatterers such as air bubbles and brine inclusions in the ice, and on dielectric properties, which in turn depends on salinity and temperature. Presence of a snow layer, and the properties of this, will also affect the radar backscatter [3].

The ice properties will change with sea ice age. At the first stage of freezing, frazil ice of small crystals are formed, and coagulate to grease ice. Grease ice will dampen the Bragg waves, reducing the roughness, and hence the backscatter, resulting in dark regions in the SAR images. As the ice thickens, it forms gray ice (10-15 cm) and gray-white ice (15-30 cm), giving brighter radar images. When the ice reaches a thickness of 30 cm it is known as firstyear ice (FYI). The sea state and weather conditions during the ice formation will have a large effect on the roughness of the ice [46] [36].

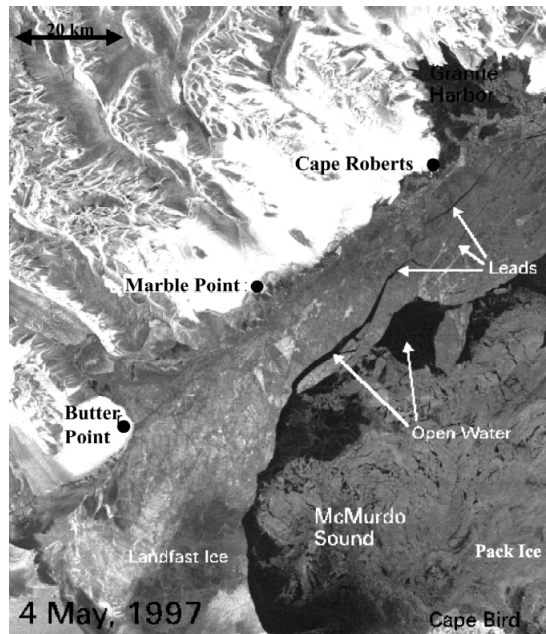


Figure 3.5: RADARSAT-1 (C-band, HH) image of a region near Cape Roberts. The image shows landfast ice, and leads along the coastline due to strong katabatic winds (figure from [35]).

FYI has high salinity and low penetration depths (depending on radar wavelength). This type of ice therefore shows mainly surface scattering [36]. Ice ridges, rubble fields, irregular edges and snow crystals can make the scattering diffuse, giving various amounts of backscatter [8] [46]. When the ice ages, brine will gradually drain from the ice, reducing the salinity. The reduced salinity of multiyear ice (MYI), allows deeper penetration into the ice, giving rise to volume scattering in addition to the surface scattering. Because of this, MYI will often have higher backscatter than FYI, and this can be used to distinguish FY Arctic ice from MYI. However, it is complicated by the diffuse surface scattering of rough FYI surfaces [46]. The difference between FYI and MYI is seen in figure 3.6, where we see bright MY ice floes compared to the darker FYI.

Presence of snow complicates interpretation as it contributes to radar backscatter, but contribution varies with age, structure and state. The dielectric constant of snow depends on density and grain size. Even a small amount of water in the snow cover will give a high dielectric loss, reducing the penetration depth, and the snow will act as an opaque filter, preventing sensing of the ice surface. Frozen snow in the winter is transparent, allowing sensing of the ice surface and volume underneath [36] [25].

Many processes can change the ice properties and hence the SAR imaging. Winds and currents can cause convergence or divergence in the ice, leading to ridges and underwater keels, or openings in the ice called leads and polynyas. This introduces open water and variability in surface roughness, both observable by a radar [46]. Orientation of ridges relative to the radar are important for

how much these changes will affect the backscatter. Presence of ice types such as pancake ice and frost flowers, and flooding of the ice, can also alter the backscatter signal, making interpretation more difficult [46].

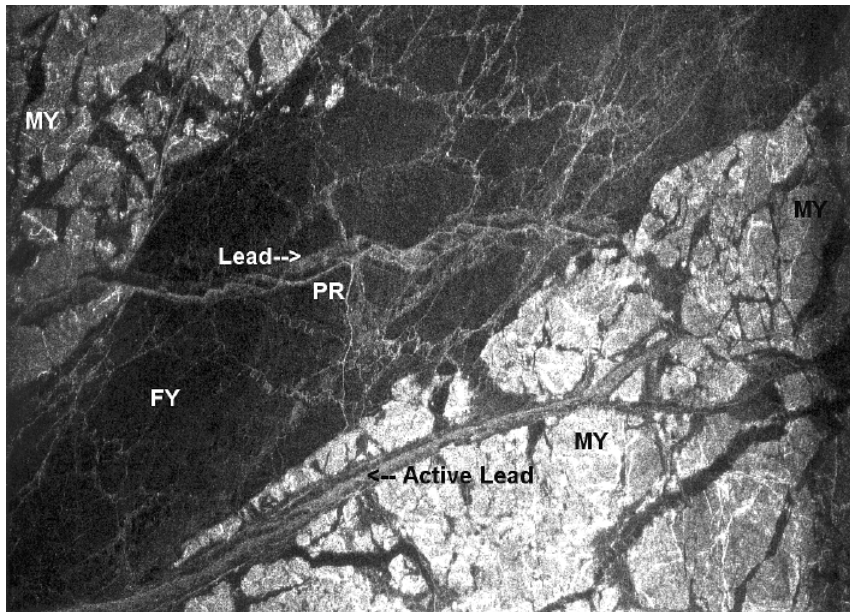


Figure 3.6: Aircraft SAR image (C-band, VV) from Beaufort Sea during the winter, showing pack ice. The imaged area is approximately 10 km wide and incidence angles range from 20° to 70° . FY, MY and PR denotes First Year, Multi Year and Pressure Ridges respectively (figure from [36]).

Seasonal variations will also change the radar backscatter. During melting, MYI backscatter decrease, e.g. due to melt ponds on top of the ice. At freeze-up, an increase in backscatter is seen, due to more volume scattering. Melting of FYI has less impact on radar backscatter [3].

It should be noted that there are differences in SAR imaging of the Arctic and the Antarctic sea ice, and some of the discussion above are only valid for Arctic areas. Melt ponds covers up to 60% of the Arctic summer ice surface, while they are largely absent from Antarctic sea ice. Antarctic sea ice comprises a much higher portion ($\sim 80\%$) of FYI than in the Arctic ($< 50\%$). The brine draining of Arctic ice are much less pronounced in Antarctica, so the contrast between MYI and FYI due to salinity is less there [25].

Radar properties, e.g. frequency, incidence angle and polarization, will also affect the measurements. Backscattering will decrease with increasing incidence angles. A linear relationship with varying slopes for different sea ice types in different seasons have been seen [20]. Regarding frequency, C-band is often used as a reasonable compromise, and provides good contrast between open water, new ice, smooth FYI, rough FYI and MYI. Shorter wavelengths are better for distinguishing different thin ice classes and FYI, while longer wavelengths are more useful when looking at level and deformed ice [3] [35]. Hence, the preferred frequency, wavelength and polarization depend on the objectives. Quad-

polarimetric SAR and the use of multipolarization have been showed to improve sea ice classification [3].

In Sandven and Johannesen (2006), Envisat ASAR data of sea ice was discussed. It was seen that cross-polarization gave better discrimination between ice and open water compared to co-polarization, although co-polarization was also found useful for this purpose. When observing low backscatter ice types, the sensor noise floor in cross-polarization channel was seen to be a possible limiting factor. Cross-polarization was found to be preferable for detecting ridges and for discrimination of FYI versus MYI, and level versus deformed ice [46]. In Askne and Dierking (2008) it is stated that for C-band SAR, HH or HV is best for FYI-MYI discrimination [3].

In Flett *et al.* (2008), SAR data from Envisat and RADARSAT-1 and -2, were evaluated for sea ice monitoring. It was seen that ice-water contrast was significantly improved using cross-polarization compared to co-polarization, particularly under high winds. While co-polarization had similar backscatter for ocean and ice during high sea, cross-polarization reduced the open water scattering virtually independent of sea roughness and incidence angle. Cross-polarization was also best for looking at rougher, deformed ice. On the other hand, ability to discriminate new, thin and FYI was better for HH than in HV. It was stated in Flett *et al.* (2008) that for ice monitoring, co- and cross-polarization should be used complementary [12].

3.4 SAR imaging of icebergs

Icebergs are formed when fresh water ice breaks off ice shelves or glaciers and become free floating. Icebergs from calving may be very large, e.g. sizes of 400 to 11.000 km² have been seen. Smaller icebergs are frequently produced, and may become deadly marine hazards. Detection of iceberg activity is interesting for monitoring of the calving rate, and because of the serious hazard they pose for mariners, causing delays and damage [35]. In remote sensing, icebergs can give similar scattering as ships, and discrimination between these are desirable.

Icebergs are categorized according to shape and size. Size categories using length measures are growler (0-5 m), bergy bit (5-15 m), small berg (15-60 m), medium berg (60-120 m), large berg (120-220 m) and very large bergs (> 220 m). Major shape categories include tabular, non-tabular, blocky, wedge, dry rock and pinnacle [35].

Icebergs have bright signatures compared to the darker surroundings of drifting and fast ice, and are known to have a scattering mechanism combined of surface and volume scattering [14]. At steep incidence angles, surface scattering will be dominating, while shallow angles will give more volume scattering. Polar sea ice is an inhomogeneous medium containing salt, brine pockets and air bubbles, and various types of ice, depending on its age, can have large differences in scattering [8]. Detection of icebergs depends on sea state and size. As several icebergs often calve at the same time and drift together, they can be detected as clusters [35]. An example of a SAR image of kilometer-sized icebergs are shown in figure 3.7.

Surface topography will also affect the backscatter, e.g. by producing dihedral scatterers. Antarctic ice are often covered by thick snow layers, producing strong backscatter as the snow crystals act as discrete scatterers, and the microwaves

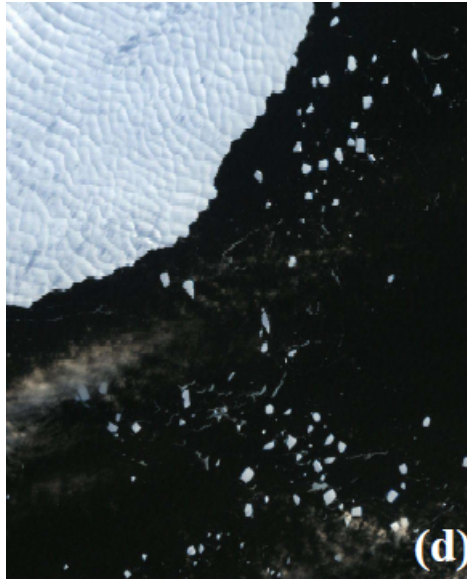


Figure 3.7: SAR response of kilometer-sized icebergs (figure from [35]).

can penetrate tens of meters into the snow pack. Glacial ice however, produces weak backscatter. Tall icebergs can produce radar shadows, which highlight the topography. Shadows increase with incidence angle, making medium incidence angles ($30^\circ - 55^\circ$) optimum for iceberg detection [35].

Several studies on iceberg detection and monitoring have been done. In Power *et al.* (2001), iceberg detection in RADARSAT-1 data was evaluated as function of iceberg size, wind speed and incidence angle. It was found that for incidence angles above 35° , icebergs with size in the order of resolution could generally be detected. Larger icebergs was believed to be detected more consistently, even during rough seas. They found that wind speed significantly affects iceberg detection. High clutter and small icebergs relative to resolution could make icebergs indistinguishable from speckle [38].

In Lane *et al.* (2002), iceberg detection was also studied. RADARSAT-1 detection in C-band, HH polarization, was evaluated for ScanSAR NarrowB and Wide modes. Iceberg pixel statistics were extracted from the images, while ocean clutter were generated using a wind model provided by Canada Centre for Remote Sensing. Based on these statistics, Probability Of Detection (POD) curves for various wind strengths were generated. Detection was found to increase with incidence angle and with decreasing wind. Medium icebergs (in the order of resolution cell and larger) in ScanSAR NarrowB mode with incidence angles $31^\circ - 46^\circ$ could be detected in over 50% of the time in strong winds. Small icebergs (in the order of resolution cell) in Wide2 mode with incidence angles $31^\circ - 39^\circ$ was also detected in approximately 50% of the time in strong winds, and in over 75% of the time for Wide3 with $39^\circ - 45^\circ$ incidence angles. For lighter wind, this was believed to increase dramatically. Lane *et al.* (2002) concluded that despite the significant effect of wind on iceberg detection, a reasonable success could be obtained with the modes described for icebergs with sizes in

the order of resolution [19].

In Lane *et al.* (2004), iceberg detection in sea ice conditions was evaluated based on Envisat ASAR and RADARSAT-1 data. POD curves for icebergs of various sizes in different sea ice types were made. It was found that detection increased with incidence angle (from $31^\circ - 39^\circ$ to $39^\circ - 45^\circ$). The POD curves for icebergs in sea ice was similar to performance on open water at a wind speed of 35 knots. Sea ice was shown to degrade detection, however not significantly if sea ice segmentation was successfully applied [20].

Giant icebergs (longer than approximately 18,5 km) are systematically tracked based on satellite data by the National Ice Center and Brigham Young University Center for Remote Sensing. Information on smaller icebergs have largely relied on ship-borne observation, which are not always accurate, and normally do not provide iceberg tracks. Since the end of the 1990s, the utilization of SAR in providing information on smaller icebergs have been investigated. Silva and Bigg (2004) proposed the first computer-based method allowing both identification and tracking of icebergs as small as 200 m in length based on high-resolution satellite SAR [49].

The identification process consisted of automatic segmentation using an edge detection approach, followed by classification of objects as iceberg or non-iceberg. Classifications were made based on object characteristics including average σ^0 , area, ratio between major and minor axes and ratio between perimeter and the square root of the area. The icebergs were matched between images acquired at different times and locations based on shape and size similarities [49].

The technique was tested in Silva and Bigg (2004) on wintertime data from European Remote Sensing satellite 1 (ERS-1) data from Antarctica. The automatic identification and tracking was compared to a manual analysis. The majority of the objects were correctly segmented, but a large number of false alarms was produced. The detectability increased with iceberg size. The automatic tracking was compared to a validation set obtained manually. Between 60% and 100% of the matches between the three images were correct. Most misses and incorrect classifications were due to at least one iceberg in a pair not being segmented out [49].

3.5 Discrimination between icebergs and ships

For SAR imagery to be useful in marine surveillance, we want as high detection and classification accuracy as possible. Discrimination between icebergs and ships in SAR images is not always reliable, especially in single polarization images. Misclassification can be due to feature similarities between target classes, target sizes in the order of pixel spacing, wind- and atmospheric conditions and insufficient training data [14].

Several studies on how to discriminate between ships and icebergs have been done. A study performed by Howell *et al.* (2004) using Envisat ASAR multi-polarization (HH and HV) data concluded that ships had comparable responses in HH and HV channels, while icebergs had less or no response in HV compared to HH. Detection in HH and HV versus detection in only HH could then be used as a discrimination method, with an accuracy of 87% according to this study. A single feature method for discrimination was the HV/HH area ratio, which gave an accuracy of 97% in the same report.

Figure 3.8 shows an example of a ship and an iceberg, and corresponding ASAR HH response, HV response, and pixel membership map. The latter represent the radar signature for the target in terms of CFAR pixel membership, where the pixel membership was assigned to one of three classes: HH and HV (blue), HH exclusively (red) and HV exclusively (green) [14].

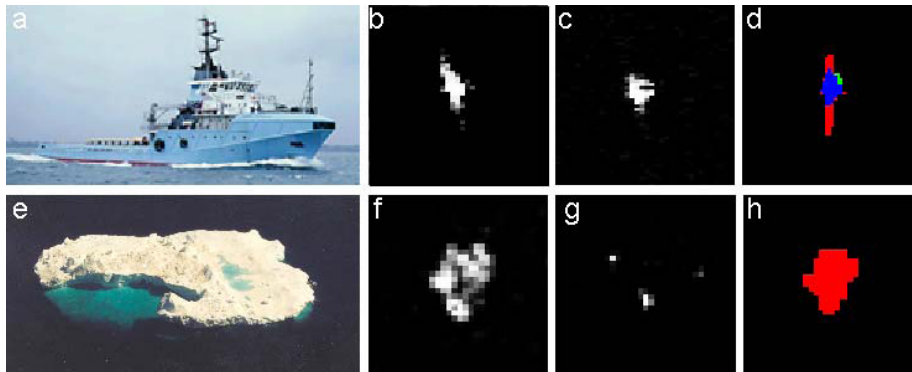


Figure 3.8: a) Maersk Chegnecto, a 70 m supply vessel. (b) HH data of a. (c) HV data of a. (d) Multi-polarization membership map of a. (e) Large Tabular Iceberg, 160 × 140 m length/width. (f) HH data of e. (g) HV data of e. (h) Multi-polarization membership map of e (figure from [14]).

A more recent study by Howell *et al.* (2008) examined the potential of multipolarization data for detection and discrimination of ship and iceberg targets. Convair-580 SAR data (used to simulate RADARSAT-2 (HH,HV), (HH,VV), (VH,VV), HH, HV and VV data) and spaceborn ASAR (HH,HV) and (HH,VV), with validated ship and iceberg targets, were used. For the simulated RADARSAT-2 data, the discrimination accuracy was found to increase with resolution, and quad-polarization performed better than dual, which in turn was better than single polarization. HH discrimination was benchmarked at 92,9%, (HH,HV) at 96,4% and quad-polarization at 98%. It was found that intensity based metrics provided more information than morphological features and decompositions, and HV intensity was found to be the most significant single feature. Also for the ASAR (HH,HV) set, HV was found to be important, as ships was visible, while the icebergs often were buried in the noise floor. HH variance was another significant feature, as icebergs had lower variance than ships due to lower mean and maximum backscatter levels. An accuracy of 95% was achieved for this data set. For ASAR (HH,VV), 99% discrimination accuracy was possible, but direct comparison between the two ASAR accuracies is difficult as they were based on different data sets. Among other things, the (HH,VV) set included only large ships, possibly affecting the accuracy of discrimination.

The general conclusions of Howell *et al.* (2008) were that HH channel was preferred over VV for iceberg detection, and that HV showed the highest potential for discriminating icebergs and ships. The combination (HH,HV) was hence recommended for operational ship/iceberg detection purposes [15].

Chapter 4

Methods

The methods we use in the experimental part of this project include Pauli decomposition of quad-polarimetric data, generation of RGB (Red Green Blue) images, segmentation of targets, calibration and ground range correction of SLC images and calculation of incidence angles, peak-to-background ratios (PBR), target-to-background ratios (TBR) and geometric moments for a number of targets in the different data sets. The data are described in chapter 5. The methods applied, and some related methods that could be used to further characterize the targets, are described in the following sections.

4.1 Polarimetric decompositions

In section 2.5, the scattering matrix S was defined, and different polarimetric decompositions were mentioned. The objective of these decompositions is to describe the measured backscattering in S as a sum of the scattering responses from simpler objects. In the following section, the Pauli decomposition will be derived.

4.1.1 Pauli decomposition

The scattering vector is defined as

$$\vec{k}_4 = V[S] = \frac{1}{2} \text{Trace}([S]\Psi) = [k_1 \ k_2 \ k_3 \ k_4]^T \quad (4.1)$$

where S is the scattering matrix as defined in equation 2.7, $V[S]$ is the Matrix Vectorization Operator and Ψ is a complete set of four 2×2 basis matrices [6]. In the case of Pauli decomposition, we use the Pauli basis matrix set

$$\Psi = \{S_a, S_b, S_c, S_d\} \quad (4.2)$$

where

$$S_a = \sqrt{2} \begin{bmatrix} 1 & 0 \\ 0 & 1 \end{bmatrix}$$
$$S_b = \sqrt{2} \begin{bmatrix} 1 & 0 \\ 0 & -1 \end{bmatrix}$$

$$S_c = \sqrt{2} \begin{bmatrix} 0 & 1 \\ 1 & 0 \end{bmatrix}$$

$$S_d = \sqrt{2} \begin{bmatrix} 0 & -i \\ i & 0 \end{bmatrix}$$

The Pauli scattering vector then becomes

$$\vec{k}_{4p} = \frac{1}{\sqrt{2}} [S_{HH} + S_{VV} \quad S_{HH} - S_{VV} \quad S_{HV} + S_{VH} \quad i(S_{HV} - S_{VH})]^T \quad (4.3)$$

or

$$\vec{k}_{4p} = \frac{1}{\sqrt{2}} \begin{bmatrix} S_{HH} + S_{VV} \\ S_{HH} - S_{VV} \\ S_{HV} + S_{VH} \\ i(S_{HV} - S_{VH}) \end{bmatrix} \quad (4.4)$$

When assuming reciprocity, $S_{HV} = S_{VH}$, the Pauli basis will only contain the first three matrices, $\Psi = \{S_a, S_b, S_c\}$, and the scattering matrix becomes

$$S = \begin{bmatrix} S_{HH} & S_{XX} \\ S_{XX} & S_{VV} \end{bmatrix}$$

where S_{XX} denotes S_{HV} or S_{VH} . The scattering vector is now written as [6]

$$\vec{k}_{3p} = \frac{1}{\sqrt{2}} \begin{bmatrix} S_{HH} + S_{VV} \\ S_{HH} - S_{VV} \\ S_{XX} + S_{XX} \\ 0 \end{bmatrix} = \frac{1}{\sqrt{2}} \begin{bmatrix} S_{HH} + S_{VV} \\ S_{HH} - S_{VV} \\ 2S_{XX} \end{bmatrix} \quad (4.5)$$

The Pauli decomposition is used in the experimental part; for evaluating the scattering mechanisms of marine targets and for calculation of contrast measures.

4.1.2 Interpretation of Pauli decomposition

The Pauli scattering vector has the advantage of being directly related to the physical properties of the scatterer. These properties can be found by looking at the amount of backscattered energy coming from the different types of scatterers. The different basis matrices correspond to different types of scatterers, as summarized in table 4.1. The response we get in e.g. $|S_{HH} + S_{VV}|$ indicates how much of the scattered energy that is of the single/odd-bounce type, which typically comes from surfaces.

4.1.3 The Pauli image

The information in the scattering matrix, S , can be represented as an RGB image. By using one component for each colour channel, a colour composite is made. What is known as the Pauli image can visually enhance the scattering behaviour of the targets and land cover classes of the scene. The Pauli image is created by inserting the Pauli decomposition components from table 4.1 into the RGB channels.

Table 4.1: Pauli matrices and corresponding scattering mechanisms [57][11].

Pauli matrix	Decomposition	Scattering type	Interpretation
$\sqrt{2} \begin{bmatrix} 1 & 0 \\ 0 & 1 \end{bmatrix}$	$ S_{HH} + S_{VV} $	single-bounce, odd-bounce, surface scattering	surface, sphere, corner reflector, plate, trihedral
$\sqrt{2} \begin{bmatrix} 1 & 0 \\ 0 & -1 \end{bmatrix}$	$ S_{HH} - S_{VV} $	double-bounce, even-bounce	dihedral oriented at 0 degrees, man-made targets as ships, buildings etc.
$\sqrt{2} \begin{bmatrix} 0 & 1 \\ 1 & 0 \end{bmatrix}$	$ S_{HV} + S_{VH} $	even-bounce 45 degrees tilted, volume scattering	diplane oriented at 45 degrees, landscape, vegetation etc.

In this project, we use the Polarimetric SAR Data Processing and Educational Tool (PolSARpro) to make RGB images from polarimetric SAR data. The Pauli decomposition components and the corresponding colour channels used by PolSARpro are shown in table 4.2.

Table 4.2: Decomposition components and colour channels used for generating Pauli RGB images from quad-polarimetric data.

Colour channel	Decomposition
Red	$ S_{HH} - S_{VV} $
Green	$ S_{HV} + S_{VH} $
Blue	$ S_{HH} + S_{VV} $

As can be seen from table 4.1 and 4.2, we use the double-bounce component for the red channel, the volume scattering component in the green channel, and the surface scattering component in the blue channel. Areas dominated by the different scattering types will be distinguishable by the different colours. In an image containing land and sea areas, the sea area, mainly composed of surface scattering, will have a blue colour, and land areas, with more volume scattering in e.g. vegetation, will appear green. This colour combination is the most natural to us, as for some land cover types, it will correspond to the colours in the visual part of the spectrum.

4.1.4 Entropy and anisotropy

Another feature based on polarimetric data is the Polarimetric Entropy (PE). PE is a measure for the randomness of the scattering characteristics, and has

been widely used in unsupervised classification. Backscattering from ocean areas is dominated by surface scattering, which has low entropy. Ships have more complex scattering and high entropy values. Hence, the PE could be used to describe a marine target, and to e.g. detect a ship target from ocean clutter [59].

In Touzi (2000) and Touzi *et al.* (2001), PE, and polarization anisotropy, $PE^c = 1 - PE$, were proposed as promising tools for ship detection at incidence angles below 60° . It was found that for low incidence angles, Bragg scattering of the ocean has lower entropy than the ships polarization entropy, while at angles above 60° , the ocean backscatter became as heterogeneous as the ships, and PE and PE^c could no longer be used. As most SAR sensors operate at incidence angles below 60° , this will seldom be a problem. During rough sea, the effectiveness of entropy and anisotropy was found to be degraded, but looked promising at relatively calm wind conditions (7 knots and 14 knots) [52].

Entropy and anisotropy will not be investigated any further in this thesis.

4.2 Semi-automatic target detection

The target segmentation problem consists of separating pixels belonging to the targets of interest from the background clutter. As the main focus of this study is on the contrast and geometric measures, and not on the segmentation itself, this process is done only semi-automatic. All targets are segmented using the same method, however some parameters are set depending on the target size. Segmentation of small and large objects are discussed in section 4.2.1 and 4.2.2 respectively.

4.2.1 Segmentation of small targets

For each target, we define a subimage of size 120×120 pixels with the target at the center, as shown in figure 4.1.

We then compute the amplitude of each subimage, as given by equation 4.6.

$$A = \sqrt{Re^2 + Im^2} \quad (4.6)$$

where A is the amplitude, Re is the real part of the complex image and Im is the imaginary part of the complex image.

The background mean and standard deviation is calculated from the four 30×30 pixels corners, and a threshold is set based on these values, as seen in equation 4.7.

$$T = mean(Backg) + \alpha * std(Backg) \quad (4.7)$$

where T is the threshold, α is a constant that needs to be chosen and $mean(Backg)$ and $std(Backg)$ are the mean value and the standard deviation of the amplitude background pixels respectively.

Each pixel in the 120×120 pixels subimage is then checked to see if the pixel value is above T , in which case the pixel position keep its value in the new segmented image. If the pixel value is below T , the pixel position is given value zero in the segmented image. The result of this first part of the segmentation is an image with the background in black and the target pixels in white. However, some non-target pixels have high enough values to be segmented out. This occurs often when there is smearing of the target. To remove these, the 8 nearest

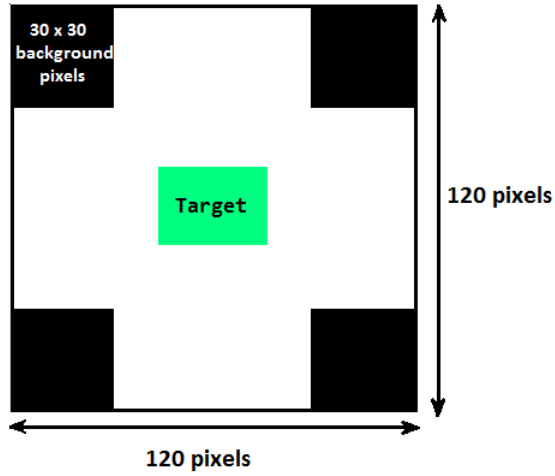


Figure 4.1: Subimage of size 120×120 pixels, with the target in green in the center. The four 30×30 pixels corners in black are used as background measure.

neighbours of each target pixel are checked according to the threshold T , and pixels with less than β neighbours above T are set to zero.

The parameters α and β have to be set before doing the segmentation. The two parameters are defined based on visual evaluation of segmentation results using different pairs of α and β .

We first decided to use the same parameter values for all targets in each data set, and define them by testing different values for two of the targets. As the targets often have quite different properties, e.g. size, intensity, amount of smearing etc., the values chosen based on two training targets from data set 1 gave poor results for some of the other targets in this set. It was therefore decided to define values of α and β for each target individually.

For each target, different pairs of values were tested. As the correct shape of the targets are not known, and as some polarizations have a lot of smearing, it was difficult to find good values for the parameters. Too high values of α or β gave very few or no pixels left after the segmentation. Too small values would segment out the smearing as part of the target. As the contrast often is better in cross-polarization than in co-polarization (see discussion in section 3.2.1), we focused mostly on the cross-polarization channels when choosing the values. One problem is that the cross-polarization channels often have the most smearing, and to remove this, values had to be set so high that nothing was left in the co-polarization channels. Because of these differences, a trade-off between amount of smearing segmented out, and making sure not the whole target disappears in some of the channels had to be done.

It should be noted that for one of the smallest targets, the contrasts in some channels are so poor that nothing is segmented out, even for relatively low values of α and β , as will be seen in the results in chapter 6.

The values of α and β for the different targets are summarized in table A.1

in the appendix.

An example of the segmentation process is shown in figure 4.2. This is target 1 in polarization HV, where $\alpha = 9$ and $\beta = 5$.

One advantage of the segmentation method applied in this project is the fact that it is based on local conditions. Ocean background will vary a lot over a SAR image, e.g. due to local wind conditions, bathymetry and imaging geometry. By using the corners of each subimage as background measure, each target is segmented based on the local conditions, instead of on a global background measure used for the whole image. By using the corners for background measures, we avoid the smearing of the target often seen as a "star" extending out from the target in range and/or azimuth direction. By using all four corners for the background measure, as opposed to one (as used in the pilot study [50]), more reliable background statistics and a more appropriate value for T are obtained. Possible influences from nearby targets or other features, will also have less effect by using all four corners. When the subimage size is constant, the relative amount of background pixels compared to subimage size, is also constant. Another improvement from the pilot study is that we by doing a segmentation make sure the peak value lies within the target.

4.2.2 Segmentation of large targets

Some of the targets chosen from data set 3 are significantly larger than the other targets. These are chosen in order to be able to compare the same iceberg targets in different images and polarizations. The segmentation of these targets is done as described in section 4.2.1, with a few adjustments as listed below:

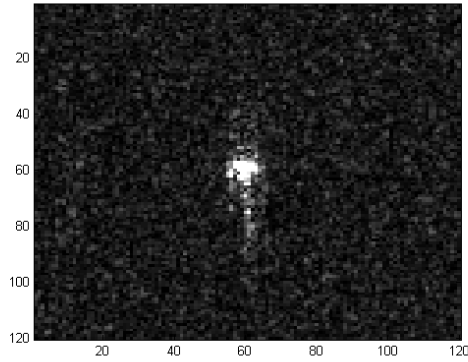
- Subimage size for these targets are 350×350 pixels instead of 120×120 pixels.
- The iceberg targets are surrounded by smaller ice blocks with high backscattering, making it difficult to segment out only the target of interest. When checking the number of neighbours above the threshold T , a window of size 5×5 around the pixel are therefore used, instead of 3×3 , i.e. 24 neighbours instead of 8 are checked.

This adjusted segmentation method is applied to targets 21, 23, 24, 31, 32 and 33. Due to the number of small high-backscatter objects around the icebergs, a trade-off between missed iceberg pixels and segmentation of unwanted small objects has to be made.

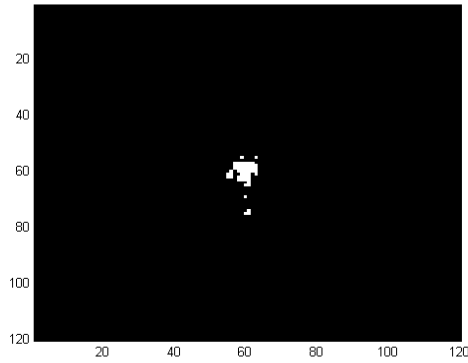
4.3 Calibration

In the context of remote sensing imaging, calibration means to convert raw data into accurate and useful geophysical and biophysical quantities. The objective of calibrating SAR imagery is to provide data in which the pixel values can be directly related to the radar backscatter of the scene. In addition, radiometric correction is necessary for the comparison of SAR images acquired with different SAR sensors, at different times or with different modes.

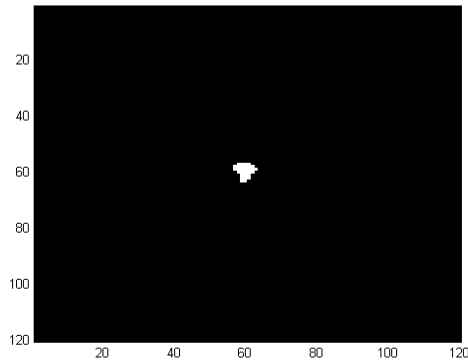
The reflectivity of the features in the scene is expressed in terms of radar cross section (RCS) and denoted by σ . The area dependence is removed from



(a) Original amplitude image, scaled for visualization.



(b) Segmented image without removal of unwanted pixels.



(c) Segmented image after removal of unwanted pixels

Figure 4.2: Segmentation of target 1 in HV polarization; (a) original image, (b) image before and (c) after removal of pixels with less than 5 neighbours above the threshold T . RADARSAT-2 Data and Products ©MacDONALD, DETTWILER AND ASSOCIATES LTD. (2010) - All Rights Reserved

the RCS, resulting in the normalized radar cross section (NRCS), also called the radar backscattering coefficient, σ^0 , often given in dB [7].

For the data sets used in this project, the SLC image is calibrated using range-dependent gain values retrieved from a Look-up-table (LUT) included with the image product. This adjustment is done to improve appearance by optimizing radiometric scaling and compensating for changes in backscatter with changing incidence angle. The calibration is done as shown in equation 4.8.

$$C = \frac{A^2}{Gain^2} \quad (4.8)$$

where C is the calibrated value, A is the amplitude value and $Gain$ is the gain value retrieved from the LUT-file. The relationship in equation 4.8 applies for SLC RADARSAT-2 products [41]. $Gain$ is a range dependent gain, i.e. each range value has the same value of $Gain$ for all azimuth values.

4.4 Calculation of incidence angles

In order to investigate the dependency of contrast ratios on incidence angle, the incidence angle of each ship has to be computed. The parameters needed to compute local incidence angles are given in table B.1 - B.10 in the appendix. The number of samples per line and the near range and far range incidence angles are used for this calculation. To find the location of a target in the image in terms of pixel number, the *cursor location tool* in ENVI is used. The incidence angle of one particular target is given as

$$\theta_{local} = \theta_{near} + \Delta_r * \frac{\theta_{far} - \theta_{near}}{\#samples} \quad (4.9)$$

where θ_{local} is the local incidence angle for the target, θ_{near} and θ_{far} are the near range and far range incidence angles of the image, Δ_r is the position of the target center in range direction and $\#samples$ is the number of samples per line for the image.

In order to find the correct local incidence angles, it is important to find Δ_r as the number of samples counted from near range. If the image has been flipped left to right, the near range will be at the right side of the image, and this needs to be accounted for when finding Δ_r .

4.5 Ground range correction

Uncorrected radar images such as SLC data is displayed in what is called slant-range geometry, which means it is based on the actual distance from the radar to the different features in the scene. The difference between slant range distance and ground range distance are illustrated in figure 2.2 in section 2.1.1.

The use of slant range leads to some distortion of the features present in the image. Areas in near-range will be more compressed compared to areas further out in range. This is illustrated in figure 4.3 where targets A1 and B1 are the same size on the ground, but in slant range, A2 appears to be smaller than B2.

The slant range display, Z , can be converted into the true ground range display, G_{rd} , placing the features in their correct planimetric (x, y) position

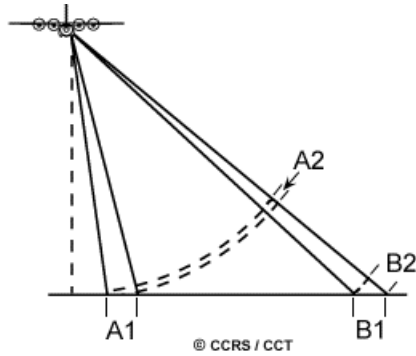


Figure 4.3: Compression of areas in near-range compared to far-range in slant range images (figure from [27]).

relative to one another. The Pythagorean theorem can be applied to transform a slant range image into ground range, as given by equation 4.10.

$$G_{rd} = \sqrt{Z^2 - H^2} \quad (4.10)$$

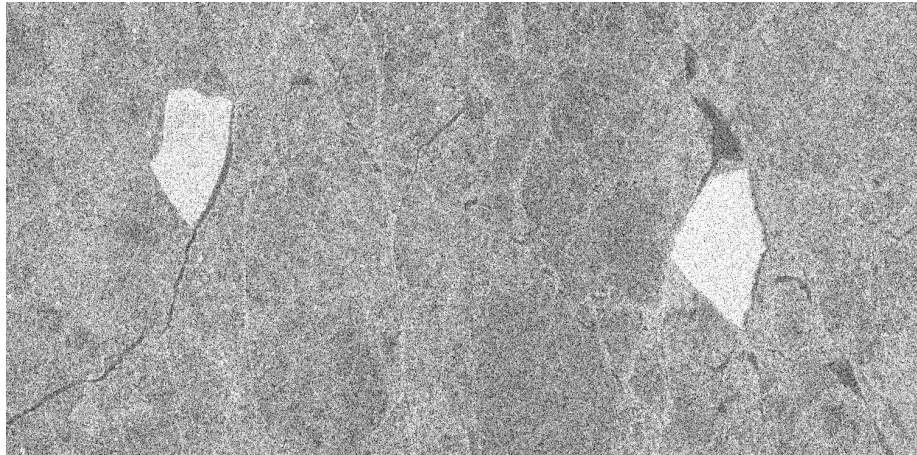
where H is the altitude of the sensor [18]. A resampling of the image is done in order to get the ground range corrected image. Figure 4.4 shows how images of two icebergs look before and after ground range correction.

When calculating the geometric moments described in section 4.7.3, it is important to use the ground range corrected images, in order for the targets to have their correct shape. The ground range correction is therefore applied to the subset of the data used in the calculation of geometric moments. The ground range correction is done using Radar Tool (RAT) [45].

4.6 Contrast measures

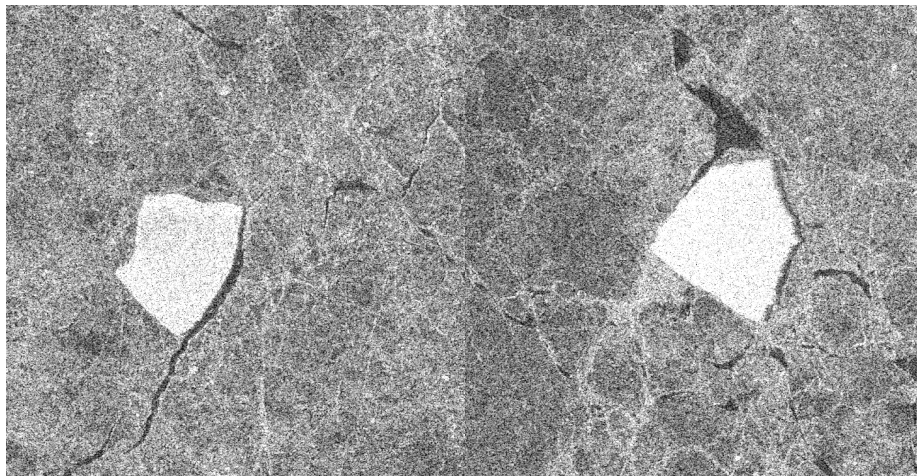
In the pilot study [50], PBR were calculated for 29 marine targets (no ground truth information) based on the amplitude image. The definition of subimages and the measure for the background mean are improved in the current project, and the TBR is calculated in addition to the PBR. A further improvement is to calculate the contrast for the backscattering coefficient σ^0 in dB instead of using the amplitude image.

The ratios in the current study are calculated based on segmented and calibrated images derived by the methods described in section 4.2 and 4.3. For data set 1, calculations are done for all four polarimetric channels $|S_{HH}|$, $|S_{VV}|$, $|S_{HV}|$ and $|S_{VH}|$, and for the Pauli decomposition components $|S_{HH} + S_{VV}|$, $|S_{HH} - S_{VV}|$ and $|S_{HV} + S_{VH}|$. Data set 2 and 3 consist of dual- and single-polarization images respectively, and the contrast measures are found for the available polarizations. The different contrast measures are described in the following sections.



(a) Target 31 in slant range.

(b) Target 32 in slant range.



(c) Target 31 in ground range.

(d) Target 32 in ground range.

Figure 4.4: Examples of slant range and ground range images of icebergs. RADARSAT-2 Data and Products ©MacDONALD, DETTWILER AND ASSOCIATES LTD. (2010) - All Rights Reserved

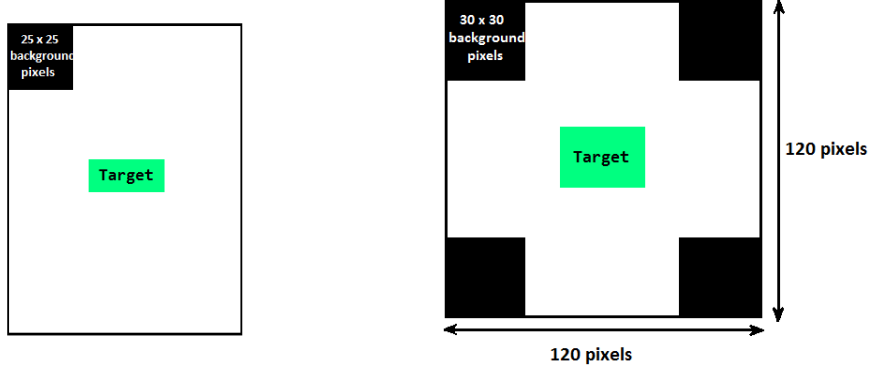
4.6.1 Peak-to-background ratios in the pilot study

The method used for calculating the PBR in the pilot study [50] is given by equation 4.11, and is simply the highest (peak) value in the whole subimage divided by a background mean.

$$PBR_{PS} = \frac{\hat{A}_{peak}}{\hat{A}_{backg}} \quad (4.11)$$

PBR_{PS} denotes the peak-to-background ratio for the pilot study, \hat{A}_{peak} is the maximum amplitude value in the subimage and \hat{A}_{backg} is the mean value of the 25×25 pixels of the upper, left corner.

No segmentation were done here, meaning the peak value did not have to be in the target at all. The size of the subimage was not constant, and the background pixels are chosen from only one corner. Figure 4.5 illustrates the differences between the approach applied in the pilot study versus the approach applied in the current study, with respect to subimage size and definition of background pixels.



(a) Subimage with varying size used in the pilot study.

(b) Subimage with size 120×120 pixels used in the current study.

Figure 4.5: Subimages as defined in the pilot study and in the current project.

The method from the pilot study is applied to data set 1, in order to compare the result of this method to the improved method as is described in section 4.6.2.

4.6.2 Peak-to-background ratios in the current project

To improve the method from the pilot study, we define new subimages for each target with a constant size of 120×120 pixels. Instead of using one corner for calculating the background mean, we use all four 30×30 pixels corners. The PBR is calculated both in amplitude and in σ^0 values.

The PBR based on the amplitude image, PBR_A , is calculated according to equation 4.12.

$$PBR_A = \frac{A_{peak}}{A_{backg}} \quad (4.12)$$

where A_{peak} is the peak value of the pixels classified as target and A_{backg} is the background mean value.

The PBR for the radar backscattering in dB is based on the calibrated image extracted as given by equation 4.8. The ratio between the peak value of the target pixels and background mean is found, and then a log transform is done. This is given in equation 4.13.

$$PBR_{\sigma^0} = 10 * \log_{10}\left(\frac{C_{peak}}{C_{backg}}\right) \quad (4.13)$$

where PBR_{σ^0} is the peak-to-background ratio in dB, C_{peak} is the peak value of the calibrated target values and C_{backg} is the background mean of the four 30×30 pixels corners of the calibrated image.

4.6.3 Target-to-background ratios

The peak values may vary a lot between the targets. When trying to evaluate how targets in general appear in radar images, an average of all target pixels may be more useful than just the peak value. This parameter will probably show less variation, and give us a more reliable measure for how large contrasts we can expect for marine targets, and what polarization channels or decompositions that produce the best results. The TBR is therefore calculated in addition to PBR, for both the amplitude image and for σ_0 in dB. The TBR based on amplitude, TBR_A is given by equation 4.14.

$$TBR_A = \frac{A_{target}}{A_{backg}} \quad (4.14)$$

where A_{target} is the mean value of the target pixels in the segmented amplitude image, and A_{backg} is the mean of the background pixels.

For the TBR in dB, TBR_{σ^0} , the target mean C_{target} is calculated based on the calibrated image, and the same background mean, C_{backg} , as for the PBR_{σ^0} is used. TBR_{σ^0} is computed from equation 4.15.

$$TBR_{\sigma^0} = 10 * \log_{10}\left(\frac{C_{target}}{C_{backg}}\right) \quad (4.15)$$

4.7 Geometric measures

As stated in section 3.2, satellite SAR is not suitable for ship identification, but can be used for classification based on features such as target size and other geometric measures. Also for discrimination between target types, as is discussed in this project, measures of a targets geometry could be useful. In the following sections, examples of such features are described. Only the geometric moments discussed in section 4.7.3 are applied to the data in the experimental part.

4.7.1 Basic region descriptors

A region, such as a marine target in a SAR image, can be described by considering scalar measures based on the geometric properties of the region. The simplest property is given by size or *Area*, given as

$$Area(\xi) = \int_u \int_v \Omega(u, v) dv du \quad (4.16)$$

where $\Omega(u, v) = 1$ if the pixel is within a shape, $(u, v) \in \xi$, and 0 otherwise. The integrals are approximated by summations as shown in equation 4.17:

$$Area(\xi) = \sum_u \sum_v \Omega(u, v) \Delta Area \quad (4.17)$$

where $\Delta Area$ is the area of one pixel. The area will change with scale changes, but is invariant to rotation. If $\Delta Area = 1$, the area is measured in pixels [28].

The *Perimeter* of a region is given by equation 4.18.

$$Perimeter(\xi) = \int_t \sqrt{u^2(t) + v^2(t)} dt \quad (4.18)$$

where $u(t)$ and $v(t)$ denote the parametric co-ordinates of a curve enclosing a region ξ . Equation 4.18 corresponds to the sum of all arcs defining the curve. For the discrete case, $u(t)$ and $v(t)$ are defined by a set of pixels in the image, and equation 4.18 are approximated by

$$Perimeter(\xi) = \sum_a \sqrt{(u_a - u_{a-1})^2 + (v_a - v_{a-1})^2} \quad (4.19)$$

where u_a and v_a represents the co-ordinates of the a th pixel forming the curve [28].

From the area and perimeter, the *Compactness* of the region can be characterized. The compactness expresses a measure of the shape given as the ratio between perimeter and area, as seen in equation 4.20.

$$Compactness(\xi) = \frac{4\pi Area(\xi)}{Perimeter^2(\xi)} \quad (4.20)$$

Compactness measures the ratio between the areas of the shape and the circle that can be traced within the same perimeter, i.e. the efficiency with which the boundary encloses the area. For a circular region, $Compactness(\xi) \simeq 1$, which is maximum compactness. Low values of $Compactness(\xi)$ are associated with involuted regions and highly elongated shapes.

Another measure for region characterization is dispersion or *Irregularity*, measured as the ratio of major chord length to area, defined as

$$Irregularity(\xi) = \frac{\pi \max((u_a - \bar{u})^2 + (v_a - \bar{v})^2)}{Area(\xi)} \quad (4.21)$$

where (\bar{u}, \bar{v}) represent the co-ordinates of the center of mass of the region. The numerator defines the area of the maximum circle enclosing the region.

An alternative measure of dispersion can be defined as the ratio between maximum and minimum radius, that is

$$Irregularity_R(\xi) = \frac{\max(\sqrt{(u_a - \bar{u})^2 + (v_a - \bar{v})^2})}{\min(\sqrt{(u_a - \bar{u})^2 + (v_a - \bar{v})^2})} \quad (4.22)$$

This measure defines the ratio between the radius of the maximum circle enclosing the region, and the maximum circle that can be contained in the region [28].

The area, perimeter, compactness and irregularity measures described here could be interesting features for describing the different marine targets.

4.7.2 Ship length estimation

Another important geometric feature is the length of a target. Length estimates can be difficult to obtain from SAR images, e.g. due to smearing, and research on this have been discussed by e.g. Vachon and Wolfe (2008).

Vachon and Wolfe (2008) evaluated Envisat ASAR AP data using a tool called VUSAR. This tool segmented the ship signature, enhanced the shape by morphological operations and derived the ship length. The ship signature length was correct in 60,1% of the co-polarization ships, and for 71,5% of the cross-polarization ships.

It was found that for co-polarization there was a considerably larger rate of underestimation of ship length than in cross-polarization. This may be due to the higher clutter levels that can mask parts of the ship. For cross-polarization there was a larger rate of overestimation of ship length than in co-polarization. Vachon and Wolfe (2008) suggested a reason for this could be that the high contrast ratios show sidelobes or artifacts more clearly.

The same study found that the incidence angle affects how well the ship length is estimated. For all polarizations, the error rate was seen to be higher for small incidence angles, but the type of error was different, with underestimates and overestimates in co- and cross-polarization respectively. The error rate was found to be higher for ships with smaller TCR [56].

Vachon *et al.* (2007) suggests the overestimates in length are related to azimuthal smearing caused by the ships large velocity component in the azimuth direction. The underestimates are related to ships where the signatures are split up into disconnected parts because of high clutter levels in co-polarization. It was concluded that for Envisat ASAR AP mode, cross-polarization was best for estimating ship length [55].

4.7.3 Moments

Moment invariants were first introduced by Hu in 1962 [16] and have been widely used for image pattern recognition due to its invariant features on image translation, scaling and rotation. The invariant moments are derived from a binary image, and are computed as follows:

The two-dimensional $(p + q)$ th order moment of a function $f(x, y)$ are given as:

$$m_{pq} = \int_{-\infty}^{\infty} \int_{-\infty}^{\infty} x^p y^q f(x, y) dx dy \quad (4.23)$$

where m_{pq} is the $(p + q)$ th order moment and $p, q = 0, 1, 2, \dots$

These moments may not be invariant when $f(x, y)$ is changed by translation, rotation or scaling. To obtain invariant features, the central moments as given in equation 4.24 are used [17].

$$\mu_{pq} = \int_{-\infty}^{\infty} \int_{-\infty}^{\infty} (x - \bar{x})^p (y - \bar{y})^q f(x, y) dx dy \quad (4.24)$$

In the case of a digital image of size $B \times D$, where $f(i, j)$ is a point in this image, the dimensional moments and central moments are given as [39]:

$$m_{pq} = \sum_{i=1}^B \sum_{j=1}^D i^p j^q f(i, j) \quad (4.25)$$

$$\mu_{pq} = \sum_{i=1}^B \sum_{j=1}^D (i - \bar{i})^p (j - \bar{j})^q f(i, j) \quad (4.26)$$

The pixel point (\bar{x}, \bar{y}) or (\bar{i}, \bar{j}) is the centroid of the image and are given as

$$\bar{x} = \bar{i} = \frac{m_{10}}{m_{00}} \quad (4.27)$$

$$\bar{y} = \bar{j} = \frac{m_{01}}{m_{00}} \quad (4.28)$$

The central moments μ_{pq} are equivalent to m_{pq} with the center shifted to the centroid of the image, and are therefore invariant to image translation. Invariance to scale is obtained by normalization, given as follows

$$\eta_{pq} = \frac{\mu_{pq}}{\mu_{00}^\gamma} \quad (4.29)$$

where η_{pq} are the normalized central moments, $\gamma = (p + q + 2)/2$ and $(p + q) = 2, 3, \dots$ [17].

Based on the normalized central moments, Hu defined seven moment invariants. These are defined in equation 4.30 - 4.36 [16].

$$I_1 = \eta_{20} + \eta_{02} \quad (4.30)$$

$$I_2 = (\eta_{20} - \eta_{02})^2 + 4\eta_{11}^2 \quad (4.31)$$

$$I_3 = (\eta_{30} - 3\eta_{12})^2 + (3\eta_{21} - \eta_{03})^2 \quad (4.32)$$

$$I_4 = (\eta_{30} + \eta_{12})^2 + (\eta_{21} + \eta_{03})^2 \quad (4.33)$$

$$I_5 = (\eta_{30} - 3\eta_{12})(\eta_{30} + \eta_{12})[(\eta_{30} + \eta_{12})^2 - 3(\eta_{21} + \eta_{03})^2] \\ + (3\eta_{21} - \eta_{03})(\eta_{21} + \eta_{03})[3(\eta_{30} + \eta_{12})^2 - (\eta_{21} + \eta_{03})^2] \quad (4.34)$$

$$I_6 = (\eta_{20} - \eta_{02})[(\eta_{30} + \eta_{12})^2 - (\eta_{21} + \eta_{03})^2] \\ + 4\eta_{11}(\eta_{30} + \eta_{12})(\eta_{21} + \eta_{03}) \quad (4.35)$$

$$I_7 = (3\eta_{21} - \eta_{03})(\eta_{30} + \eta_{12})[(\eta_{30} + \eta_{12})^2 - 3(\eta_{21} + \eta_{03})^2] \\ - (\eta_{30} - 3\eta_{12})(\eta_{21} + \eta_{03})[3(\eta_{30} + \eta_{12})^2 - (\eta_{21} + \eta_{03})^2] \quad (4.36)$$

The first six moments are absolute orthogonal invariants, while the last one is the skew orthogonal invariant.

Moment invariants have been known as one of the most effective methods to extract descriptive features for object recognition in e.g. classification of aircrafts, ships, ground targets etc. In Premaratne and Safaei (2009), moment invariants were used as a feature for ship classification. The objective was to assess how effective they were as features compared to other physical features such as length estimates. Even though the results of using other features were superior to the use of moment invariants, it was concluded that Hu moments show a great promise in automatic ship classification, with reduced complexity in the overall system, as calculation of many physical parameters can be difficult and time consuming, leading to errors and misclassifications [39]. In oil spill detection, Hu's 1st invariant planar moment has been found to separate well between dark spots with thin, piecewise elongated shapes and spots with other arbitrary shapes [4].

Hu's 1st moment of marine targets can be used to describe the elongatedness of these, and possibly be a feature for discrimination between targets of different shapes, e.g. ships, platforms and icebergs. In this project, we evaluate Hu's 1st invariant moment for a subset of the targets, and compare different target types. In order to find the correct geometric measures, a ground range correction of the SLC images as described in section 4.5 is done before calculating the Hu moments. A segmentation of the ground range corrected subimages was conducted as described in section 4.2, with new values for α and β , given in table A.2 in the appendix.

4.8 Other relevant methods

To conclude this chapter, two more methods that have been used for ship characterization in other studies, but are not applied to our data, will be briefly described.

4.8.1 Total Degree of Rotation

In Panagopoulos *et al.* (2008), a new feature for vessel identification, the Total Degree of Rotation (TDR), was proposed. The feature was evaluated as the average capability of a ship surface to change the polarization of the incident radiation. A new image was derived, where each pixel corresponded to the capability of a specific scatterer to change the incident polarization. Derivation was based on assessing the amount of EM energy that changed polarization as mean value over all pixels.

Envisat ASAR data with VV and VH polarization was used in the experiment. When the EM radiation was scattered on a sea surface, the plane of polarization did not change, giving dark areas in the VH image. Vessels on the other hand, will rotate the polarization, and would therefore be revealed. The TDR was given as

$$TDR = \frac{1}{NVP} \sum_{i=1}^{NVP} \frac{pixel_i(VH)}{pixel_i(VV) + pixel_i(VH)} = \frac{1}{NVP} \sum_{i=1}^{NVP} B_i \quad (4.37)$$

where NVP is the number of vessel pixels, and $pixel_i(VH)$ and $pixel_i(VV)$ are the received energy in the horizontal plane and vertical plane, respectively, for vertical transmission. B_i expresses the ability of one specific vessel pixel to change the EM polarization, and takes values between 0 and 1.

It was demonstrated that TDR could discriminate between different types of ships, but Panagopoulos *et al.* (2008) stated that the TDR should be used in combination with other features for ship identification [37].

4.8.2 Symmetric Scattering Characterization Method

In Touzi and Charbonneau (2003), Symmetric Scattering Characterization Method (SSCM) was investigated, and found to be very promising for ship characterization. The ship elemental targets of significant maximized symmetric scattering component could be identified, and was proposed to be useful for identification of ships in different weather and sea conditions. In an experiment, a ships pitch angle was accurately estimated. However, SSCM was found to be very sensitive to system focus setting and Doppler centroid shift, and Touzi and Charbonneau (2003) states that these errors should be removed before applying the method [54].

Follow-up studies were done in applying SSCM to SAR images containing ships, validating the potential of SSCM to characterize ships, e.g. for estimating the ships orientation (pitch and roll). The method was applied to the ship mast and other structures of symmetric scattering. The SSCM was found to be useful for providing a ships specific distribution of "permanent" scattering targets, and hence could be used for classification and identification [7].

Chapter 5

Data

The data used in this project consists of three different data sets composed of ten SAR images. The first set is quad-polarized images of marine targets (i.e. ships and oilrigs) in ocean background, the second set is dual-polarized images containing marine targets (i.e. ships) in sea ice background, and the third data set is single-polarization data of icebergs with unknown background composition. All the data are obtained by RADARSAT-2. The satellite itself, the Automatic Identification System (AIS) for ground truth information on ships, and the individual data sets with corresponding auxiliary information are described in more detail in the following sections.

5.1 RADARSAT-2

RADARSAT-2 was launched December 14th 2007 from the Baikonur Cosmodrome in Kazakhstan. The satellite is a cooperation between the Canadian Space Agency and MacDonald Dettwiler and Associates Ltd.(MDA). It is a SAR satellite, and provides information useful for e.g. environmental monitoring, ice mapping, resource mapping, disaster management and marine surveillance.

RADARSAT-2 is the successor of RADARSAT-1, with improvements such as quad-polarimetry, finer resolution, flexible selection of polarization, left- and right-looking imaging, faster turn-around schedule for data acquisition, better data storage and more precise positional measurements. RADARSAT-2 was one of the first commercial spaceborne SAR satellites with quad-polarization capabilities, and is the world's most advanced commercial C-band SAR satellite.

RADARSAT-2 travels in a polar, sun-synchronous orbit, with a period of approximately 101 minutes, at an altitude of 798 km. It does 14 orbits per day and has a repeat cycle of 24 days. The satellite is designed for a lifespan of 7 years, but may, as RADARSAT-1, live longer. RADARSAT-2 has a spatial resolution of 3 - 100 m and operates in the C-band at a frequency of 5,405 GHz [44]. The radar can operate in different modes as illustrated in figure 5.1. Some properties of the modes, including nominal swath width, resolution, incidence angle and polarization, are listed in table 5.1.

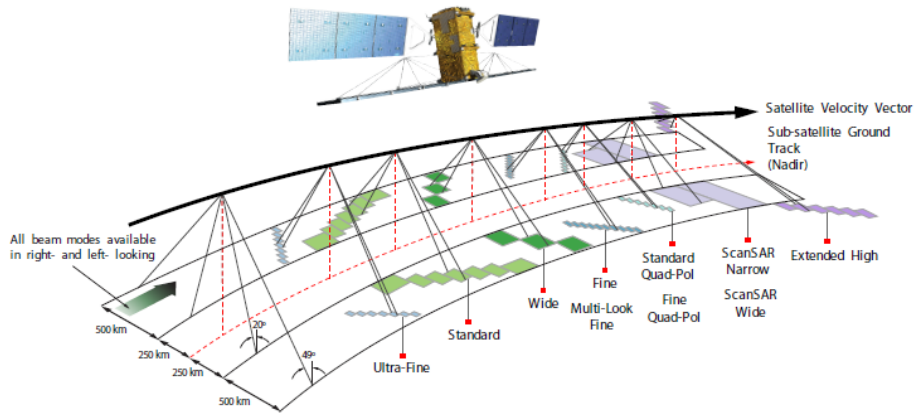


Figure 5.1: RADARSAT-2 modes of operation (figure from [40]).

Table 5.1: Properties of the different modes of RADARSAT-2 [40].

Beam mode	Nom. swath width	Approx. range resolution	Approx. azimuth resolution	Approx. incidence angle	Polarization
Ultra-Fine	20 km	3 m	3 m	$30^\circ - 49^\circ$	Single
Multi-Look Fine	50 km	8 m	8 m	$30^\circ - 50^\circ$	Single
Fine	50 km	8 m	8 m	$30^\circ - 50^\circ$	Single or dual
Standard	100 km	25 m	26 m	$20^\circ - 49^\circ$	Single or dual
Wide	150 km	30 m	26 m	$20^\circ - 45^\circ$	Single or dual
ScanSAR Narrow	300 km	50 m	50 m	$20^\circ - 46^\circ$	Single or dual
ScanSAR Wide	500 km	100 m	100 m	$20^\circ - 49^\circ$	Single or dual
Extended High	75 km	18 m	26 m	$49^\circ - 60^\circ$	Single
Fine Quad-Pol	25 km	12 m	8 m	$20^\circ - 41^\circ$	Quad
Standard Quad-Pol	25 km	25 m	8 m	$20^\circ - 41^\circ$	Quad

5.2 Automatic Identification System

The AIS is used by ships and Vessel Traffic Services (VTS), for identification and location of vessels. Ships can exchange identification, position, course, speed etc., with nearby ships and VTS stations. AIS is required to be installed aboard international voyaging ships of ≥ 300 gross tonnage and on all passenger ships. A directive issued by the European Union (EU) require all European fishing vessels with length above 15 m to use an AIS transponder. The AIS system is used for both collision avoidance, search and rescue operations and other emergency response operations, and also for studying traffic patterns and for general traffic monitoring [24].

Ships that do not operate their AIS will not show up in the AIS system.

Matching of AIS data and satellite images can reveal vessels which are not sending AIS information, and these can be checked for illegal activities, e.g. illegal fishing or environmental crimes.

The Norwegian Coastal Administration (NCA) has a land based network of AIS stations in Norway. At 39 locations along the coast, AIS information are received. The data are available as AIS raw data or as a map with traffic information, but data access are restricted [30].

AIS stations placed along the coasts only have a range of 30-40 nautical miles. To be able to monitor areas further away from the shore, satellite based AIS systems are developing. In July 2010, the Norwegian satellite AISSat-1 was launched, now covering all Norwegian waters [33].

5.3 Data set 1: Man-made targets in ocean background

Data set 1 consists of three quad-polarimetric RADARSAT-2 images, I1, I2 and I3, from the coast of Norway, more specifically from the Norne field. This area is of special interest as the production ship Norne is located here, and images of the ship can be systematically acquired with different radar parameters and sea state.

Details of image I1 - I3 are listed in table B.1 - B.3 in the appendix. Corresponding ground truth information in the form of AIS data and weather data are available for this data set, and are used in the discussion in chapter 6. See section 5.3.1 and 5.3.2 for details.

Image I1 is fine, quad-polarization mode, while I2 and I3 are standard quad-polarization mode. All three images are of product type SLC. Table 5.2 and 5.3 list some properties of these modes.

Table 5.2: RADARSAT-2, Fine Quad-Pol, SLC details [42].

Pixel spacing (Range \times Azimuth [m])	4,7 \times 5,1
Resolution (Range \times Azimuth [m])	5,2 \times 7,6
Scene size (Range \times Azimuth [km \times km])	25 \times 25
Number of looks (Range \times Azimuth)	1 \times 1

Table 5.3: RADARSAT-2, Standard Quad-Pol, SLC details [42].

Pixel spacing (Range \times Azimuth [m])	8,0 or 11,8 \times 5,1
Resolution (Range \times Azimuth [m])	9,0 or 13,5 \times 7,6
Scene size (Range \times Azimuth [km \times km])	25 \times 25
Number of looks (Range \times Azimuth)	1 \times 1

The range coordinates for SLC products are given in radar slant range. Both scene size and resolution are nominal values, and ground range resolution depends on incidence angle.

The images have four polarization channels, and contain both phase and amplitude, making them 8-dimensional. The images are not multi-look, and

therefore contain more speckle and noise. Geographical position of the three images are shown in figure 5.2. All images are processed at Kongsberg Satellite Services (KSAT).

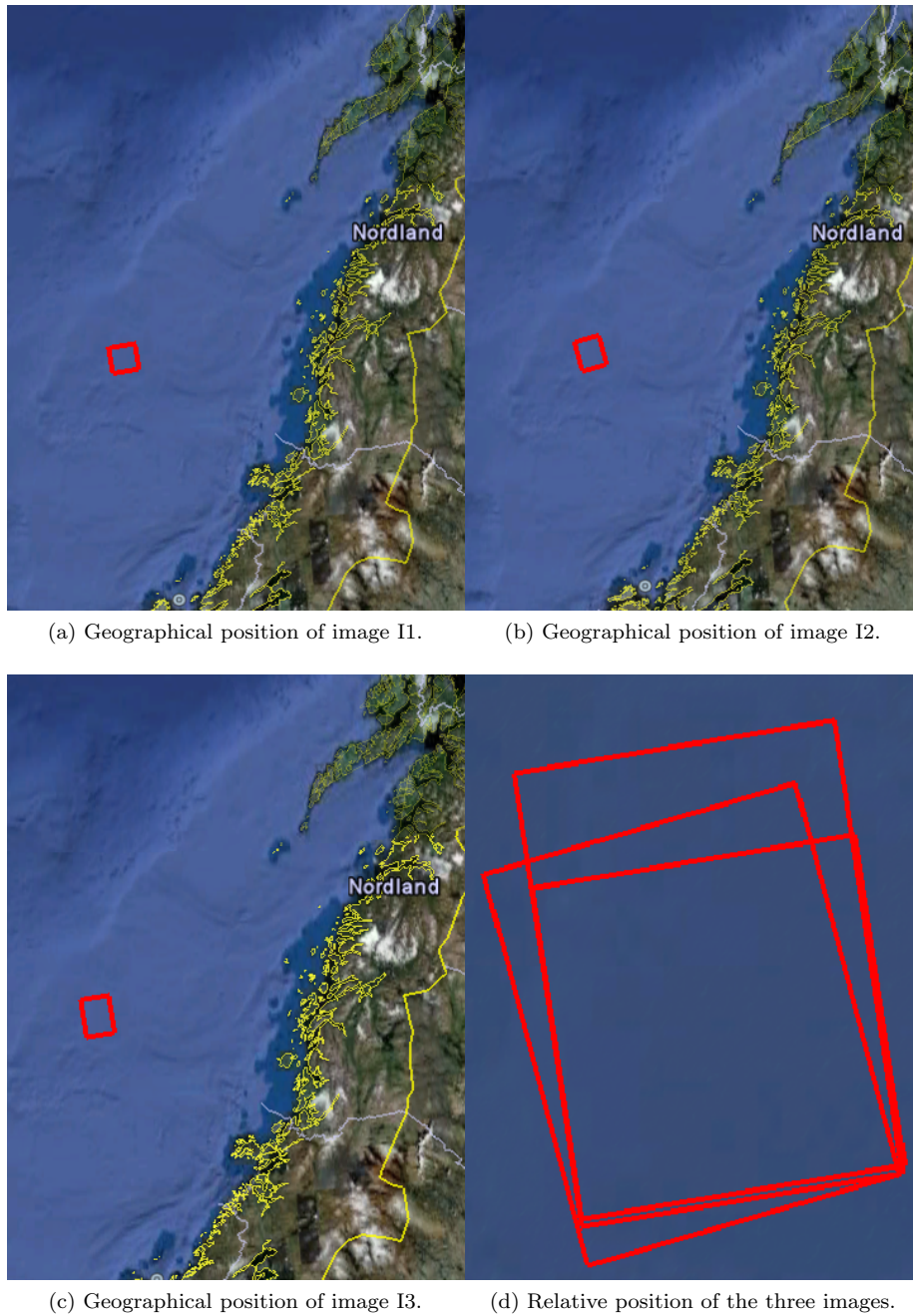


Figure 5.2: Geographical positions of image I1, I2 and I3 (figures from Google Earth).

Data set 1 contains marine targets as ships and oil rigs. After visual inspection of the data, 18 targets were identified, and 16 subimages were extracted. Two of these subimages contain two targets, as the targets were too close to be separated. Table 5.4 shows how the targets are distributed in the images.

Table 5.4: Number of targets and subimages in data set 1.

Image	# targets	# subimages
I1	6	5
I2	6	5
I3	6	6

Figure 5.3 - 5.5 show subimages of the Pauli image (described in section 4.1.3) derived from I1-I3. The target numbers are overlaid. Here we see how strong responses the different targets give, and their spatial distribution within the images. The images are not ground range corrected, and may be distorted.

5.3.1 AIS data

AIS data from the Norwegian Coastal Administration is available for data set 1 [30]. Location of the targets and target sizes are some of the information contained in the AIS file that is useful for this study. The AIS data is matched with the targets located in georeferenced versions of image I1 - I3, and based on this, the targets can be identified.

Target identity and some properties are summarized in table 5.5. Target numbers marked with * means that this target is composed of two targets, but is treated as one as they are too close to separate. Note that there are repeated acquisitions of some of the targets. Some parameters were missing from the AIS file, and are hence extracted from other sources as given by the references.

Figure 5.6 shows photos of some of the targets present in the images.

Table 5.5: Properties of the targets in data set 1.

Name	Target	Target type	Length	Width
Ocean Prince	1, 10, 14	Ship	64,5 m [48]	13,83 m [48]
Norne	2, 6, 11	Ship	260 m	44 m
Deepsea Bergen	3	Rig [34]	93 m	67 m
Aker Spitsbergen	4*, 8, 13	Rig ¹	120 m	77 m
Island Challenger	4*	Ship	93 m	20 m
Far Star	5	Ship	84 m	18 m
Island Wellserver	7, 12	Ship	116 m	26 m
West Alpha	9*, 16	Rig [34]	90 m	26 m
Skandi Mongstad	9*	Ship	97 m	22 m
Urvaag	15	Ship	44,95 m[9]	9 m [9]

¹In the AIS file, this target is listed as a cargo ship, but the image show a rig. Hence, this target will be treated as a rig in this thesis.

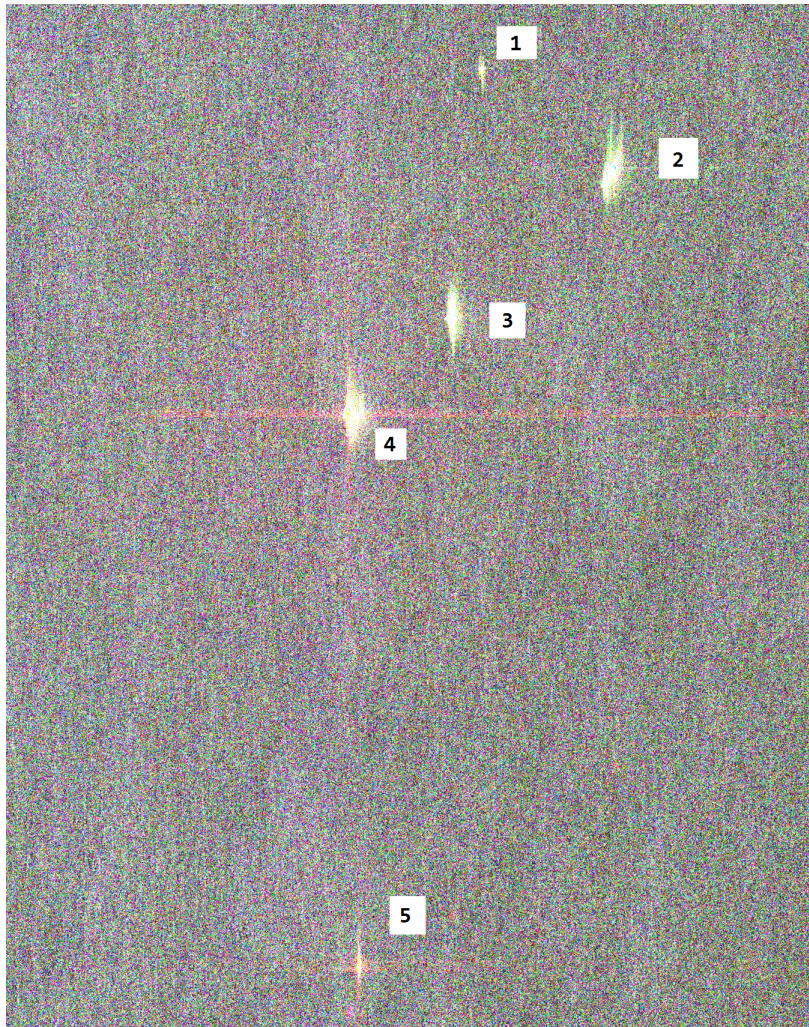


Figure 5.3: Pauli image derived from image I1.

5.3.2 Weather data

Weather data, i.e. wind strength, wind direction and wave height, are obtained from The Norwegian Meteorological Institute, and are summarized in table 5.6. Weather data obtained at Norne is only available for one of the three dates of image acquisition. Data from another platform, Heidrun, and from some nearby ships are used for the other dates. "Ship X" and "PHEC" are both ships with known positions. Visual observations from the ships are not as accurate as the official measurements from the platforms, and this needs to be considered when using the data. The exact time of image acquisitions are found in table B.1 - B.3 in the appendix.

Figure 5.7 shows the locations of the weather data acquisitions together with the images. The locations of the platforms are obtained from the Norwegian

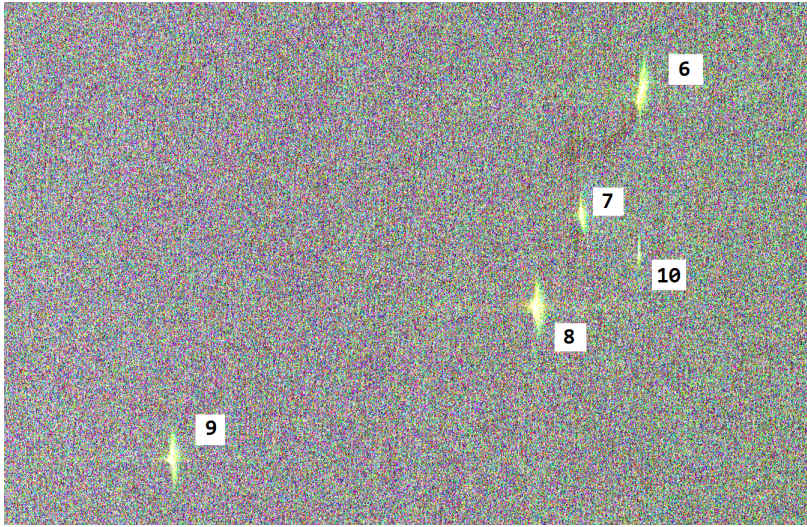


Figure 5.4: Pauli image derived from image I2.

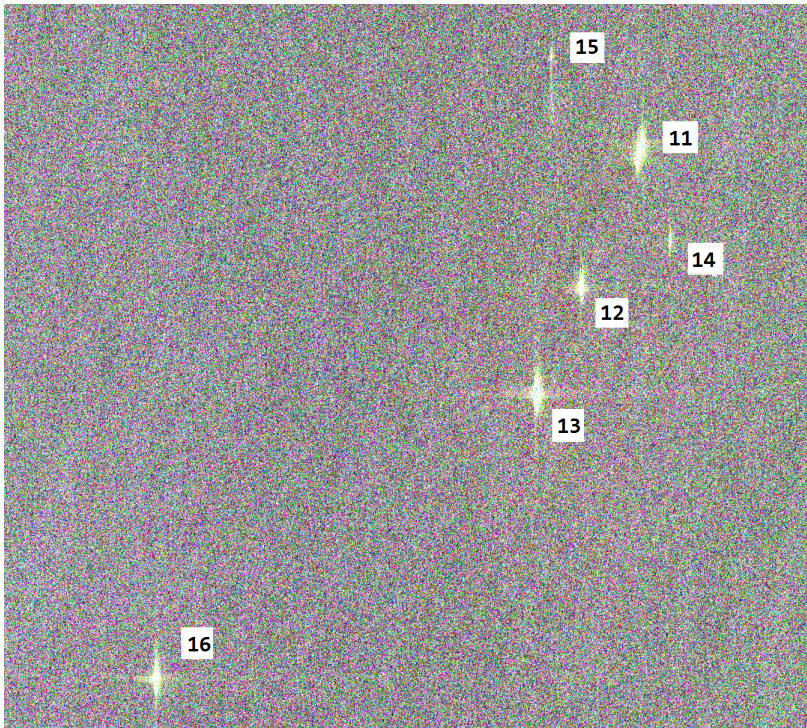


Figure 5.5: Pauli image derived from image I3.

Petroleum Directorate [31] while the ship positions are given by The Norwegian Meteorological Institute. We can see that there are certain distances between



Figure 5.6: Photos of some of the targets present in I1, I2 and I3.

Table 5.6: Weather data for data set 1.

Image	Location	Time	Wind strength	Wind direction	Wave height
I1	Norne	17:00	7 m/s	20° (N-NE)	
	Norne	18:00	7 m/s	20° (N-NE)	
	Ship X	18:00			2,5 m
	Heidrun	18:00			2,0 m
I2	Heidrun	15:00	7 m/s	50° (NE)	1,0 m
	Heidrun	16:00	7 m/s	50° (NE)	
	Heidrun	17:00	7 m/s	50° (NE)	
	PHEC	18:00	7 m/s	70° (E-NE)	1,5 m
I3	Heidrun	15:00	5 m/s	40° (NE)	0,5 m
	Heidrun	16:00	5 m/s	40° (NE)	
	Heidrun	17:00	5 m/s	40° (NE)	

some of the sites of weather data acquisition and the image positions. A colocation would be optimal, however this is the best data accessible, and it gives an indication of the wind conditions in the area at the dates of interest.



Figure 5.7: The observation sites for obtaining weather data, and position of image I1, I2 and I3 (figure from Google Earth).

5.4 Data set 2: Ships in sea ice background

Data set 2 consists of three dual-polarimetric RADARSAT-2 images, I4, I5 and I6, acquired a little east of Svalbard. Details of the images are listed in table B.4 - B.6 in the appendix. All three images are of fine mode and product type SLC. Table 5.7 lists some properties of this mode.

Table 5.7: RADARSAT-2, Fine mode, SLC details [42].

Pixel spacing (Range \times Azimuth [m])	4,7 \times 5,1
Resolution (Range \times Azimuth [m])	5,2 \times 7,7
Scene size (Range \times Azimuth [km \times km])	50 \times 50
Number of looks (Range \times Azimuth)	1 \times 1

The range coordinates for SLC products are given in radar slant range. Both scene size and resolution are nominal values, and ground range resolution depends on incident angle.

The images have two polarization channels, VH and VV, and contain both phase and amplitude, making them 4-dimensional. The images are not multi-look. Geographical positions of the images in data set 2 are shown in figure 5.8. All images are processed at KSAT.

5.4.1 Ground truth data

As these images were obtained during the *Oil in Ice Experiment*, ground truth information, including ship identity and location, was available [26]. In I4, two

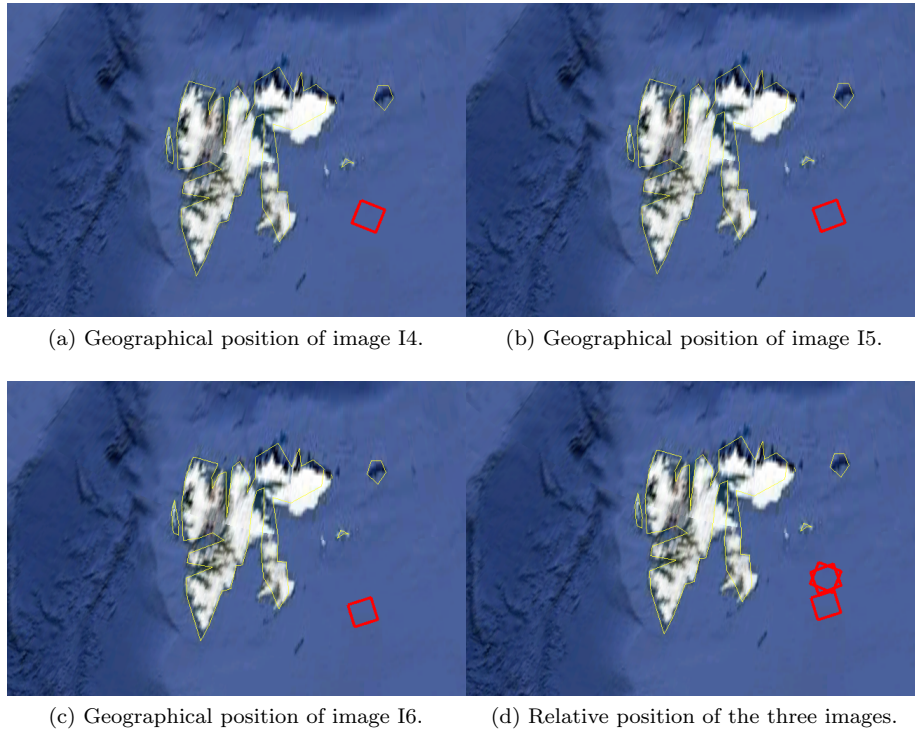


Figure 5.8: Geographical positions of image I4, I5 and I6 (figure from Google Earth).

ships are present, while I5 and I6 only contain one ship each. It is the same two ships that are imaged twice. R/V Lance is present in I4 and I5, while K/V Svalbard is found in I4 and I6. Some properties of the two ships are summarized in table 5.8. Photos of the ships and photos taken from the area at the dates of interest are shown in figure 5.9.

Table 5.8: Properties of the targets in data set 2 [29][32].

Name	Target	Length	Width
K/V Svalbard	17, 20	103,7 m	19,1 m
R/V Lance	18, 19	60,8 m	12,6 m

5.4.2 Weather data

Weather data is obtained from The Norwegian Meteorological Institute, and are summarized in table 5.9. The observations are made from K/V Svalbard, from a buoy (BUOV2), and from a land station at Hopen. The location of the weather observation points are shown in figure 5.10. As K/V Svalbard is in, or close to, the scene sites, these measurements are the most interesting.

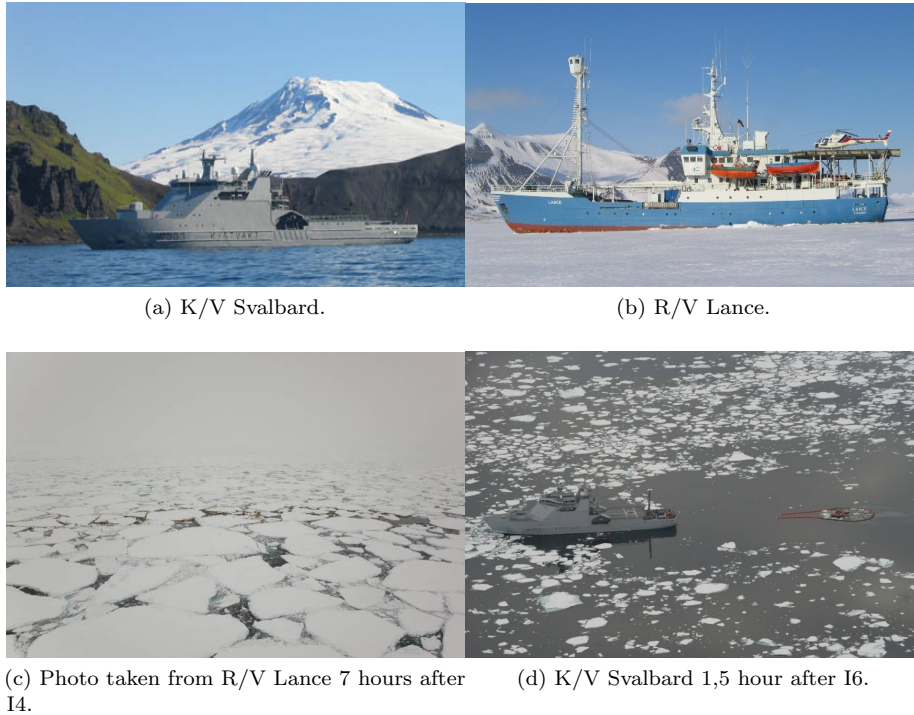


Figure 5.9: K/V Svalbard and R/V Lance and photos taken during the Oil in Ice Experiment (photos from [29], [32] and [26]).

Table 5.9: Weather data of data set 2.

Image	Location	Time	Wind strength	Wind direction	Wave height
I4	K/V Svalbard	05:00	7 m/s	180° (S)	
	BUOV2	05:00	<3 m/s	340° (NW)	1 m
	K/V Svalbard	06:00	4 m/s	180° (S)	
	Hopen	06:00	9 m/s	260° (W-SW)	
I5	K/V Svalbard	14:00	12 m/s	320° (NW)	
	BUOV2	14:00	7 m/s	340° (NW)	2,5 m
	K/V Svalbard	15:00	12 m/s	330° (NW)	
	Hopen	15:00	4 m/s	350° (N-NW)	
	BUOV2	15:00	7 m/s	350° (N-NW)	2,5 m
I6	K/V Svalbard	15:00	3 m/s	250° (W-SW)	
	Hopen	15:00	3 m/s	250° (W-SW)	

5.5 Data set 3: Iceberg targets in mixed background

Data set 3 consists of four single-polarization RADARSAT-2 SLC images, I7 - I10. The images are acquired over Antarctica and contains icebergs. The background composition is unknown, but consists of sea ice and/or ocean areas. Details of the images are listed in table B.7 - B.10 in the appendix.

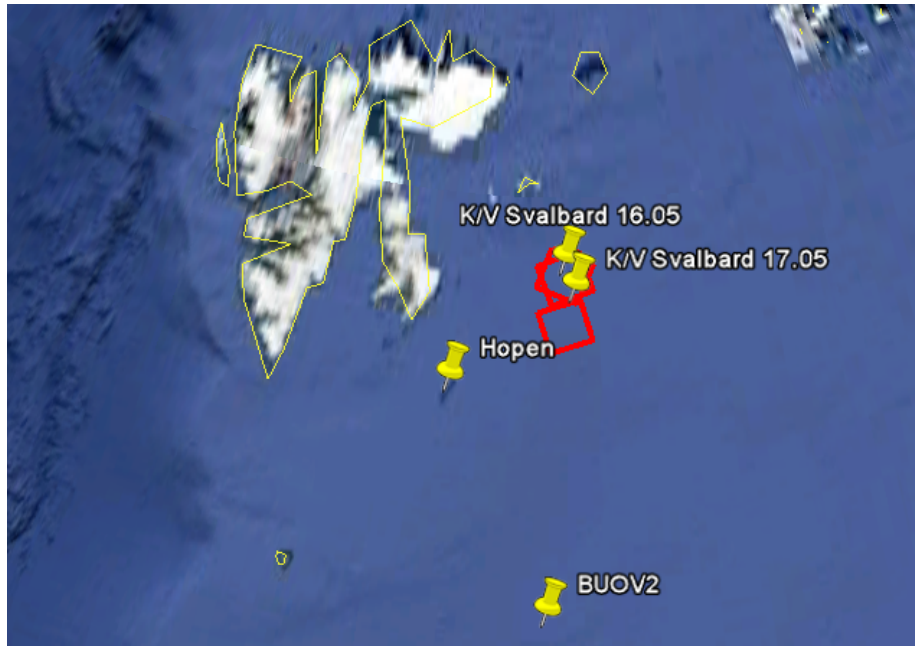


Figure 5.10: The observation sites for obtaining weather data, and position of image I4, I5 and I6 (figure from Google Earth).

Images I7, I8 and I10 are of acquisition type fine, while I9 was of type standard. Properties of these acquisition types are described in table 5.7 and 5.10.

Table 5.10: RADARSAT-2, Standard mode, SLC details [42].

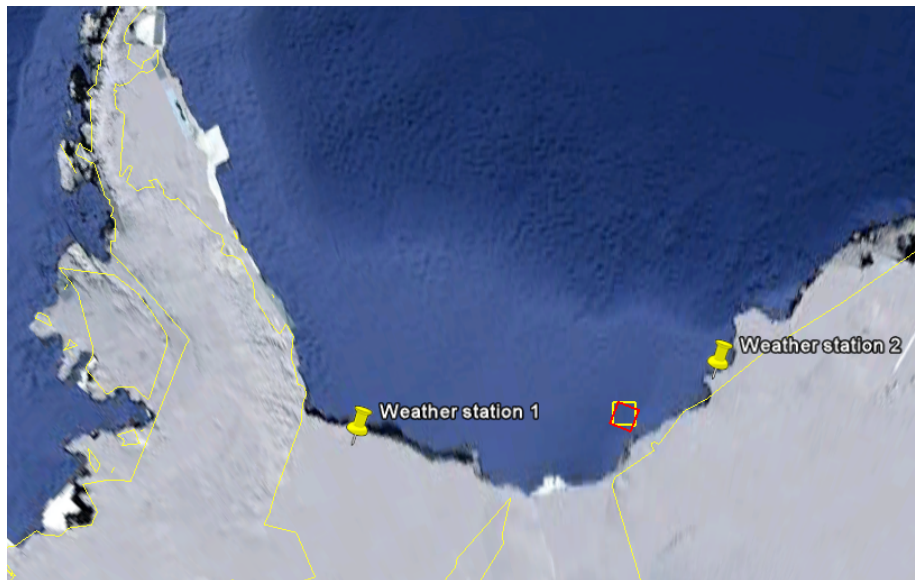
Pixel spacing (Range \times Azimuth [m])	8,0 or 11,8 \times 5,1
Resolution (Range \times Azimuth [m])	9,0 or 13,5 \times 7,7
Scene size (Range \times Azimuth [km \times km])	100 \times 100
Number of looks (Range \times Azimuth)	1 \times 1

The range coordinates for SLC products are given in radar slant range. Both scene size and resolution are nominal values, and ground range resolution depends on incident angle.

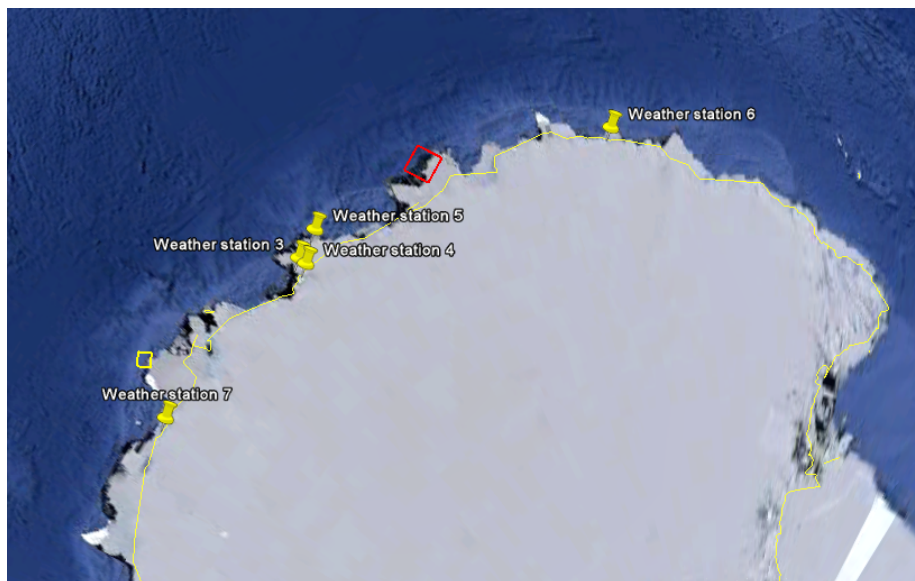
The data set contains two images with $|S_{HV}|$ polarization and two with $|S_{HH}|$ polarization, all containing both phase and amplitude. The images are not multi-look, and are processed at KSAT.

Geographical positions of the images are given in figure 5.11, together with the locations of the weather stations used for obtaining weather information.

Data set 3 was acquired for this project, to be able to compare some of the measures found for man-made targets with iceberg targets. To select scene sites, an online database of large Antarctic icebergs were used. This database is a product of a NASA sponsored project called the NASA Scatterometer Climate



(a) Position of image I7 (yellow box) and I8 (red box), and the locations of the weather stations.



(b) Position of image I9 (red box) and I10 (yellow box), and the locations of the weather stations.

Figure 5.11: Geographical positions of images and weather stations in data set 3 (figures from Google Earth).

Record Pathfinder (SCP) [47]. This database was used as a guide to find areas with high iceberg concentrations. The database is not complete, and the icebergs are likely to have moved between the last database update before scene selection and the acquisition date, but still, icebergs were captured in the images. Table 5.11 shows how 20 targets were selected from the images in data set 3.

Table 5.11: Overview of the selected targets in data set 3.

Image	Polarization	Target	Iceberg	Size
I8	$ S_{HV} $	21	A	large
		22	B	small
		23	C	large
		24	D	large
I10	$ S_{HV} $	25-30		small
I7	$ S_{HH} $	31	D	large
		32	C	large
		33	A	large
		34	B	small
I9	$ S_{HH} $	36 - 40		small

In two of the images, I7 and I8, the same four icebergs were imaged, and they are labelled A-D as can be seen in table 5.11. We do not have any ground truth information for this data set, but based on the relative position and shapes of the four icebergs in these two images, and the fact that they are acquired over the same area, it is assumed they are identical. Three of these four were relatively large icebergs compared to the rest, hence the categorization into "small" and "large" icebergs. Many of the icebergs in the images are quite large compared to a regular ship, so from image I9 and I10, the smallest icebergs are selected in order to get a best possible comparison to the man-made targets. Still, these may be larger than the ships from data set 1 and 2, and we must keep this in mind when comparing the results based on the different data.

5.5.1 Weather data

Weather is collected from the Norwegian Meteorological Institute, and is summarized in table 5.12. "WS" denotes Weather station. No wave height measurements are available for this data set. The locations of the observation points are seen in figure 5.11. The height of the observation sites may influence the measurements, but are not known.

Table 5.12: Weather data for data set 3.

Image	Location	Time	Wind strength	Wind direction
I7	WS 1	02:00	<3 m/s	20° (N-NE)
	WS 2	02:00	3 m/s	80° (E)
I8	WS 1	01:00	3 m/s	80° (E)
	WS 2	01:00	5 m/s	210° (SW)
I9	WS 3	12:00	22 m/s	90° (E)
	WS 4	12:00	40 m/s	90° (E)
	WS 6	12:00	12 m/s	90° (E)
I10	WS 7	12:00	5 m/s	90° (E)
	WS 4	13:00	40 m/s	90° (E)
	WS 5	13:00	20 m/s	110° (E-SE)
	WS 5	14:00	20 m/s	130° (SE)

Chapter 6

Results and discussions

The aim of this project is to investigate how marine targets such as ships, oil rigs and icebergs appear in SAR images. Three data sets (described in section 5.3 - 5.5) containing different targets in marine environments are investigated with respect to contrast measures and geometric measures. Contrast measures, PBR and TBR, are calculated for the different polarimetric channels available, and also for the Pauli decomposition components for data set 1. Possible relations between contrast and target type, size, incidence angle and weather conditions are investigated. Geometric measures, in form of Hu's 1st moment, are also evaluated, and compared for different target types.

The results of the experiment based on the methods and data described in chapter 4 and 5 are presented in this chapter. Section 6.1 gives a summary of the experiment and results from the pilot study, while the rest of the chapter describes the results of the current study. Section 6.2 and 6.3 show the results of the contrast measures and the geometric measures respectively.

6.1 Results from the pilot study

The aim of the pilot study was to investigate the appearance of marine targets in SAR images. 29 marine targets without ground truth information was evaluated with respect to visual appearance and contrast measures (PBR_{PS}) in the different polarization channels and Pauli decomposition components.

Visual inspection of the four polarimetric channels ($|S_{HH}|$, $|S_{VV}|$, $|S_{HV}|$ and $|S_{VH}|$) showed that cross-polarization channels were better for target discrimination than co-polarized channels. Of the Pauli components, $|S_{HV} + S_{VH}|$ gave best visual contrast between sea and target. $|S_{HH} - S_{VV}|$ and colour composites of the Pauli components also gave quite good results. $|S_{HH} + S_{VV}|$ appeared to have high noise level, and was the worst channel for visual discrimination between target and surface. However, some other features, such as ship wakes, were easiest to detect in this component.

The PBR_{PS} in the pilot study were calculated based on the amplitude image only, and are given in table C.1 in the appendix. The best contrast ratio for all targets except one, was found in either $|S_{HH} - S_{VV}|$ or $|S_{HV} + S_{VH}|$. Of all the polarization channels and decomposition components, $|S_{HV} + S_{VH}|$ produced the highest mean PBR. These two, together with $|S_{HV}|$ and $|S_{VH}|$ gave the best

results, with mean PBR_{PS} between 54, 94 and 64, 21.

We would expect $|S_{HH} - S_{VV}|$ to give good results as this component comes from double-bounce scattering from corner reflectors, of which man-made objects such as ships has many. One of the reasons why $|S_{HV} + S_{VH}|$ also gave very good contrast can be that reflections from the ocean surface are lower for cross-polarization channels than for the co-polarized, enhancing the contrast [50].

The component $|S_{HV} - S_{VH}|$ was included in the study to evaluate if the reciprocity assumption $S_{HV} = S_{VH}$ is valid for marine targets such as ships. For some of the targets evaluated, this component gave some response, indicating it is not always correct to assume $S_{HV} = S_{VH}$ when it comes to ships. The PBR_{PS} for this component was very low, and it is not suitable for ship detection. The $|S_{HV} - S_{VH}|$ is not investigated further in this thesis.

The pilot study formed a basis for the current project. The methods implemented in the pilot study are improved, e.g. with respect to improved background clutter measures and the use of calibrated data. The data used in this project is ground truthed, and so, the contrast measures can not only be compared with respect to different polarizations, but also with respect to target type, size and weather conditions. Another feature, Hu's geometric moment, are also included. The results of the current project is presented in the next sections.

6.2 Contrast characteristics

To be able to detect a target in a SAR image, it must stand out from the background in some way. Marine targets such as ships, oil rigs and icebergs stand out as bright dots or larger bright regions against a darker background. How good the contrast between target and background is, depends on many factors. In this project, the different polarization channels and Pauli decomposition components available for each data set have been compared to evaluate what polarizations are optimal for detecting the targets. As we have ground truth information for most of the data, contrast measures are evaluated with regards to target type, size, incidence angles and weather conditions, to see what factors will influence the contrast measures. Section 6.2.1, 6.2.2 and 6.2.3 discuss the results of the contrast measures for data set 1, 2 and 3 respectively, while section 6.2.4 compares the results from different target types and background classes.

6.2.1 Data set 1: Man-made targets in ocean background

Data set 1 is composed of three images containing marine targets in ocean background, as described in section 5.3. PBR and TBR based on amplitude and on calibrated values in dB, scattering mechanisms and relations between contrasts and polarization, incidence angle, size and wind conditions, are discussed in this section.

Contrast measures based on amplitude image

Peak-to-background ratios for data set 1, calculated with the same method as used in the pilot study (see section 4.6.1), PBR_{PS} , are found in table C.2 in the appendix. PBR based on the amplitude image using the method described in

section 4.6.2, PBR_A , are given in table 6.1. For all tables in this section, yellow colour indicates the largest contrast found among the different polarimetric channels and scattering components for each target. Magenta shows the second-largest contrast. It should be noted that target 10 in some polarimetric channels had too low contrast to be segmented out, and is hence listed with '-' in the tables.

Table 6.1: PBR_A for target 1 - 16.

Image	Target	$ S_{HH} $	$ S_{VV} $	$ S_{HV} $	$ S_{VH} $	$ S_{HH}+S_{VV} $	$ S_{HH}-S_{VV} $	$ S_{HV}+S_{VH} $
I1	1	21,25	16,98	32,26	31,87	19,40	41,28	39,37
I1	2	26,32	18,20	58,05	58,31	22,98	50,15	71,36
I1	3	24,22	17,26	57,40	57,38	21,88	47,75	70,38
I1	4	21,73	15,83	54,88	56,88	19,86	44,00	67,62
I1	5	24,01	17,18	39,03	39,40	12,74	51,93	46,81
I2	6	10,51	9,47	131,18	132,32	9,14	61,41	147,45
I2	7	10,44	9,58	119,08	117,79	10,00	50,85	131,15
I2	8	10,33	9,35	108,67	106,58	9,16	64,10	118,77
I2	9	9,59	8,81	124,78	121,55	7,93	60,16	136,04
I2	10	-	-	48,71	48,42	-	33,54	53,29
I3	11	32,54	20,62	89,39	89,99	26,60	54,32	109,03
I3	12	31,83	20,55	82,08	83,47	26,14	54,83	102,30
I3	13	31,71	20,97	89,35	91,30	26,60	67,43	110,94
I3	14	27,10	17,22	38,55	40,69	18,94	32,11	48,62
I3	15	32,66	11,04	40,58	40,91	9,00	52,71	50,26
I3	16	32,49	20,62	95,98	99,63	26,32	69,77	120,66
Mean		23,12	15,58	75,62	76,03	17,78	52,27	89,00

The TBRs based on amplitude, using the method described in section 4.6.3, TBR_A , are given in table 6.2.

For both table 6.1 and 6.2, we can see that the highest mean values are found in $|S_{HV} + S_{VH}|$, i.e. the majority of the targets show the highest contrast in this component. The second highest values are in most cases found in $|S_{HV}|$ or $|S_{VH}|$. None of the highest ratios are found in the co-polarization channels, $|S_{HH}|$ and $|S_{VV}|$, or in $|S_{HH} + S_{VV}|$.

If we compare the PBR_{PS} of the polarization components based on the approach applied in the pilot study, with PBR_A based on the new approach described in section 4.6.2, we can see that the mean values are very similar (see table C.2 and 6.1). The maximum difference found between the mean values of one component is actually only 0,51. This indicates that for this data set, the two methods of selecting the background pixels and defining the subimage, can both be used without large differences in the results. However, for automatic evaluation of contrast measures, a fixed (as suggested in section 4.6) or automatically adjusted subimage size is required.

When comparing the PBR_A and the TBR_A in table 6.1 and 6.2, we can see that the TBR_A mean values are much lower than the mean PBR_A , as is expected since the target peak value is higher than the target mean. The difference between the mean values between the polarizations are much smaller for

Table 6.2: TBR_A for target 1 - 16.

Image	Target	$ S_{HH} $	$ S_{VV} $	$ S_{HV} $	$ S_{VH} $	$ S_{HH}+S_{VV} $	$ S_{HH}-S_{VV} $	$ S_{HV}+S_{VH} $
I1	1	13,95	12,56	14,43	14,18	12,43	15,16	15,82
I1	2	18,44	13,73	26,55	26,64	15,73	21,54	28,57
I1	3	18,77	14,57	24,37	23,28	16,95	21,20	25,19
I1	4	16,83	13,82	18,87	19,47	13,93	22,48	20,76
I1	5	20,56	15,17	20,31	21,24	11,37	34,45	23,49
I2	6	8,27	7,59	22,64	22,78	8,65	21,17	24,22
I2	7	8,13	7,61	22,41	21,97	7,25	19,48	22,71
I2	8	8,59	8,02	24,48	24,57	7,59	22,18	25,60
I2	9	7,63	7,45	23,13	22,69	7,22	19,93	24,01
I2	10	-	-	20,69	20,62	-	16,96	20,87
I3	11	21,90	16,63	32,86	33,48	18,19	26,99	36,67
I3	12	21,41	15,32	28,54	28,49	16,80	23,45	30,08
I3	13	24,63	18,52	36,89	35,13	19,31	27,21	40,12
I3	14	12,40	8,64	13,18	14,01	10,94	14,00	15,85
I3	15	12,45	7,58	17,43	16,36	7,02	20,68	18,97
I3	16	24,07	15,93	36,11	37,45	18,30	30,74	40,70
Mean		15,87	12,21	23,93	23,90	12,78	22,35	25,85

TBR_A than for PBR_A . TBR_A also shows less variation within one polarization channel or decomposition component. From this, we can conclude that

PBR_A and TBR_A based on the amplitude image have highest mean values in $|S_{HV} + S_{VH}|$, $|S_{HV}|$, $|S_{VH}|$ and $|S_{HH} - S_{VV}|$, with the 'volume scattering' component $|S_{HV} + S_{VH}|$ on top.

As described in section 4.3, a calibration provides data with pixel values directly related to the radar backscatter, and the radiometric correction is necessary for comparison between images. Throughout the rest of this thesis, only the ratios calculated from the calibrated image, PBR_{σ^0} and TBR_{σ^0} , will be described. For convenience, these will be referred to as just PBR and TBR . The contrasts based on the amplitude images for data set 2 and 3 are included in appendix D.

Contrast measures based on calibrated image

The result of the calibration described in section 4.3 are images expressing the radar backscattering coefficient σ^0 . The PBRs and TBRs based on the calibrated images are presented in table 6.3 and 6.4 respectively.

From the PBR and TBR given in table 6.3 and 6.4, we see that

$|S_{HV} + S_{VH}|$, $|S_{VH}|$, $|S_{HV}|$ and $|S_{HH} - S_{VV}|$ produce the highest contrasts in the given order for both PBR and TBR.

As for the amplitude based contrasts, the TBR mean values span a shorter range of values than the PBR. The difference between minimum and maximum

Table 6.3: PBR in dB for target 1 - 16.

Image	Target	$ S_{HH} $	$ S_{VV} $	$ S_{HV} $	$ S_{VH} $	$ S_{HH}+S_{VV} $	$ S_{HH}-S_{VV} $	$ S_{HV}+S_{VH} $
I1	1	25,42	23,52	29,12	29,01	24,65	31,27	30,84
I1	2	27,32	24,14	34,24	34,27	26,17	32,90	36,06
I1	3	26,53	23,69	34,13	34,16	25,71	32,52	35,93
I1	4	25,63	22,93	33,73	34,03	24,87	31,85	35,51
I1	5	26,52	23,60	30,83	30,87	21,00	33,25	32,40
I2	6	19,33	18,45	41,30	41,36	18,13	34,73	42,30
I2	7	19,27	18,53	40,46	40,36	18,90	33,03	41,30
I2	8	19,20	18,33	39,70	39,49	18,15	35,12	40,45
I2	9	18,49	17,76	40,83	40,63	16,84	34,54	41,59
I2	10	-	-	32,69	32,65	-	29,50	33,50
I3	11	29,22	25,29	38,00	38,03	27,48	33,67	39,71
I3	12	29,02	25,23	37,24	37,37	27,32	33,71	39,14
I3	13	28,94	25,39	37,93	38,21	27,44	35,53	39,88
I3	14	27,61	23,64	30,70	31,20	24,48	29,07	32,70
I3	15	29,19	19,84	31,08	31,21	18,04	33,33	32,92
I3	16	29,18	25,20	38,60	38,93	27,33	35,79	40,58
Mean		25,39	22,37	35,66	35,74	23,10	33,11	37,18

Table 6.4: TBR in dB for target 1 - 16.

Image	Target	$ S_{HH} $	$ S_{VV} $	$ S_{HV} $	$ S_{VH} $	$ S_{HH}+S_{VV} $	$ S_{HH}-S_{VV} $	$ S_{HV}+S_{VH} $
I1	1	22,17	21,07	23,01	22,83	21,17	23,54	24,00
I1	2	24,66	21,92	28,48	28,51	23,18	26,43	29,46
I1	3	24,55	22,34	27,61	27,29	23,68	26,22	28,18
I1	4	23,65	21,86	25,50	25,74	21,98	26,86	26,46
I1	5	25,32	22,62	25,72	26,08	20,07	30,38	27,08
I2	6	17,37	16,62	28,85	28,89	17,67	26,80	29,56
I2	7	17,21	16,60	28,34	28,16	16,26	26,09	28,68
I2	8	17,69	17,07	29,20	29,14	16,57	27,47	29,70
I2	9	16,59	16,37	28,59	28,44	16,06	26,18	29,07
I2	10	-	-	26,27	26,23	-	24,15	26,49
I3	11	26,18	23,60	30,70	30,81	24,44	28,48	31,87
I3	12	26,04	22,96	29,78	29,78	23,81	27,33	30,61
I3	13	27,03	24,42	31,48	31,28	24,95	28,65	32,59
I3	14	21,63	18,18	22,59	23,18	20,25	22,56	24,32
I3	15	21,97	16,89	24,93	24,61	16,00	26,59	26,00
I3	16	26,86	23,05	31,65	31,94	24,40	29,47	32,87
Mean		22,59	20,37	27,67	27,68	20,70	26,70	28,56

mean value is almost 15 dB for PBR, and just above 8 dB for TBR.

We notice that all contrasts, both in TBR and PBR, are above 10 dB, except for target 10, where some polarizations give zero target pixels after segmentation. This means that all contrasts, except for target 10, are above the minimum contrast level for detecting a ship in sea clutter (described in section 3.2.1).

The PBR for all polarizations are plotted as function of target number in figure 6.1. As mentioned earlier, target 10 had low contrasts in $|S_{HH}|$, $|S_{VV}|$ and $|S_{HH} + S_{VV}|$ and no target pixels were segmented out, causing missing data points in the plot.

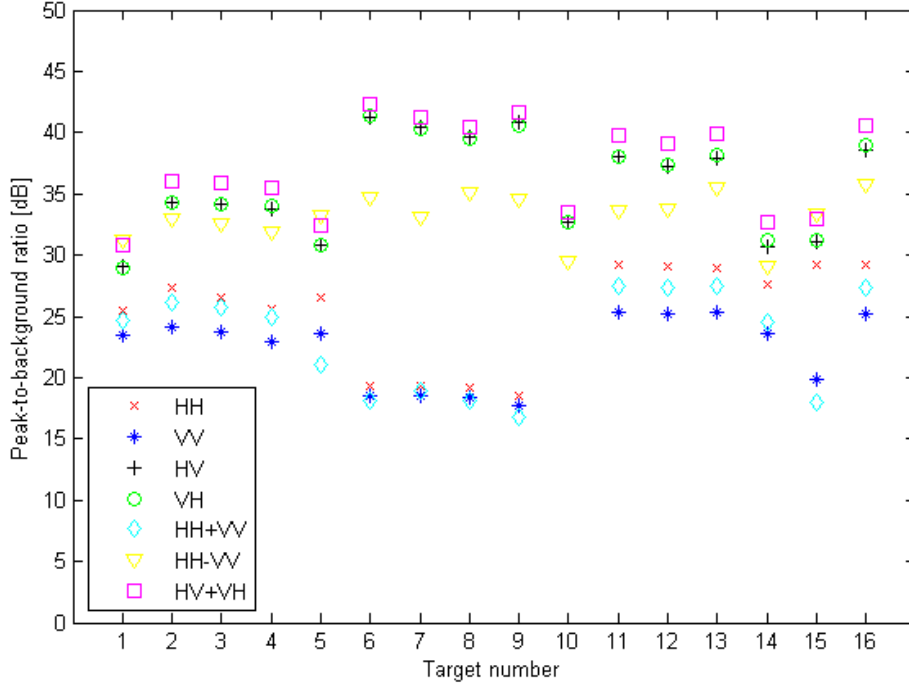


Figure 6.1: PBR as function of target number.

Figure 6.1 shows how the contrasts vary between the polarimetric channels and scattering components, and from target to target. For all targets, $|S_{HV}|$, $|S_{VH}|$ and $|S_{HV} + S_{VH}|$ give the highest contrasts, with $|S_{HV} + S_{VH}|$ on top in most cases. $|S_{HH}|$, $|S_{VV}|$ and $|S_{HH} + S_{VV}|$ have the lowest values, with $|S_{VV}|$ most often at the bottom. $|S_{HH} - S_{VV}|$ normally lies a little lower than the highest ratios, but for a few targets it actually gives the best contrast.

From figure 6.1, we should also notice that targets 6 - 9 have higher maximum values, and lower minimum values than the rest of the targets. As these targets are found in image I2, this implies there is a difference between this image and the other two. From table B.1 - B.3 in the appendix, we see that I2 has lower incidence angles than I1 and I3, possibly causing the differences we see. This will be discussed further in the next part of this section. We also note that in general, I3 (last 6 targets) seems to have slightly larger contrast values than corresponding polarizations in I1 (first five targets).

Another phenomena in figure 6.1 worth noticing, is that targets 1, 5, 10, 14 and 15 seem to have lower contrasts than the other targets in the corresponding images, i.e. target 1 and 5 have lower values than target 2, 3 and 4, target 10 has lower values than target 6 - 9 etc. As these are targets from all three images, this should not be related to image type. It can be seen in figure 5.3 - 5.5 that these are the smallest targets, indicating that target size may influence the contrast measures. This subject will be further discussed later in this section.

The TBRs for all polarizations and targets are plotted in figure 6.2.

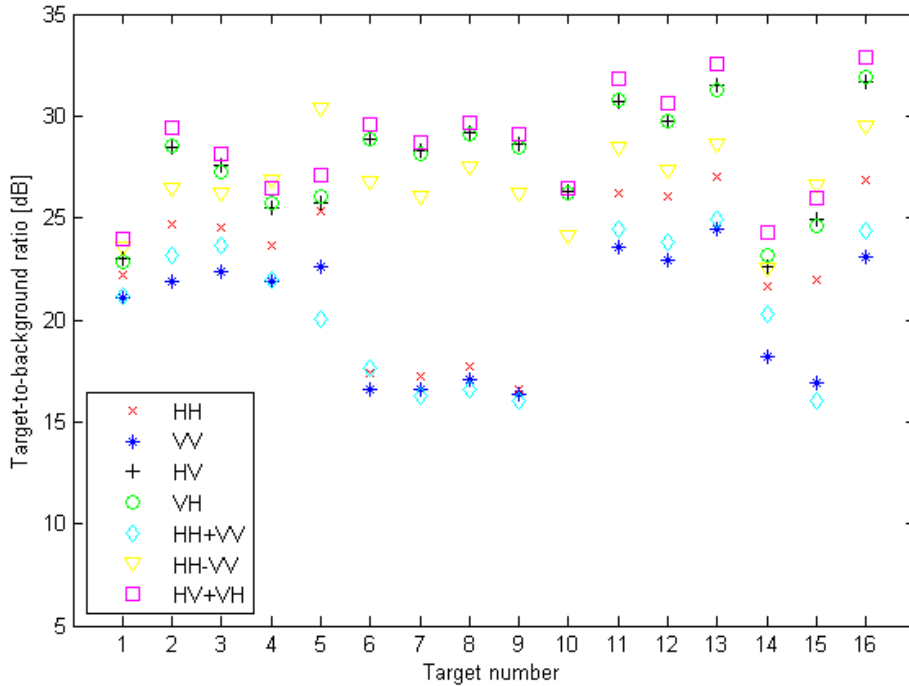


Figure 6.2: TBR as function of target number.

Figure 6.1 and 6.2 show similar result with respect to the order and significance of the polarimetric channels and scattering components. As for PBR, the gap between the high and low TBR values are larger for target 6 - 10, i.e. image I2, than for the other targets. The differences between TBR for small and large targets are not as prominent as for PBR, but can be seen for some of the targets.

From table 6.3 and 6.4, and image 6.1 and 6.2, it is obvious that

for man-made targets in ocean background, cross-polarization gives better contrasts than co-polarization, and the two cross-polarizations $|S_{HV}|$ and $|S_{VH}|$ give very similar results for all targets, as expected by the reciprocity theorem. Also, the $|S_{HH}|$ contrasts are a few dB higher than the $|S_{VV}|$ values, both for PBR and TBR.

These findings agree with previous studies reported in the literature, as described in section 3.2.1. However, the Pauli decomposition component $|S_{HV} + S_{VH}|$ often gives a better contrast than the cross-polarization chan-

nels. For PBR and TBR respectively, 13 and 12 targets out of 16 have the highest contrast in this component. When it is not the highest, it is always the second-highest. This indicates that

by using quad-polarimetric data and decompositions, better contrast between marine targets and the ocean background can be obtained.

Examples of how the ships appear in different polarization channels are seen in figure 6.3 and 6.4. The images have been scaled so that the values lie in the range $[0 \ 255]$.

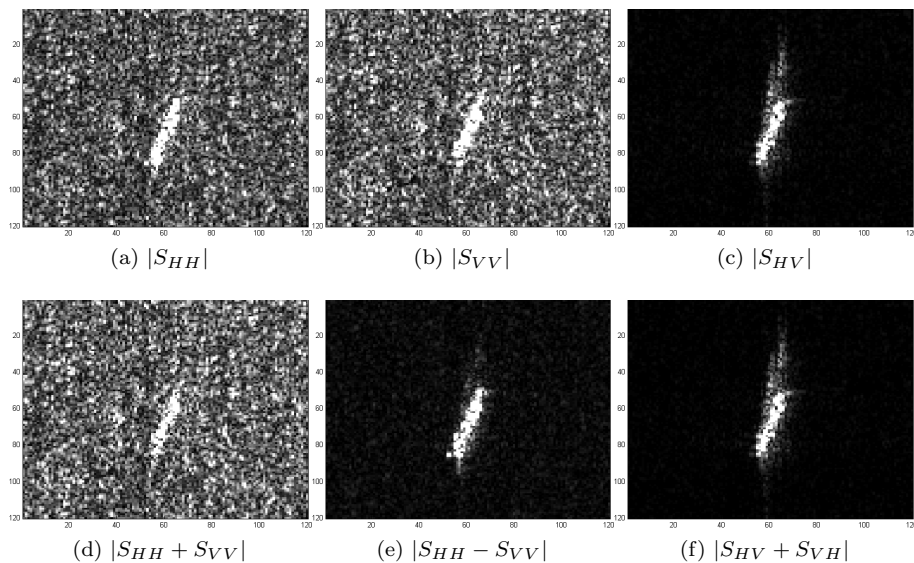


Figure 6.3: Target 6, Norne, in different polarization channels and Pauli decomposition components. RADARSAT-2 Data and Products ©MacDONALD, DETTWILER AND ASSOCIATES LTD. (2010) - All Rights Reserved

In both figure 6.3 and 6.4, we see a big difference between $|S_{HV}|$, $|S_{HH} - S_{VV}|$ and $|S_{HV} + S_{VH}|$ and the other polarizations. The cross-polarization channel and the two Pauli components mentioned have a darker, less noisy background, and provide a much better contrast between ship and sea. In figure 6.4, the ship is barely visible in the co-polarization channels and $|S_{HH} + S_{VV}|$. In both figure 6.3 and 6.4, especially in $|S_{HV}|$ and $|S_{HV} + S_{VH}|$, we see the azimuthal smearing that makes it difficult to do the segmentation.

Contrast measures and relation to incidence angle

The incidence angle for a SAR system is illustrated in figure 2.2, and the calculation method is described in section 4.4. The incidence angles for the targets in data set 1 are summarized in table 6.5.

Figure 6.5 shows the PBR for the different targets as function of incidence angle. Each mark on the x-axis represents one target, so the axis does not show the correct spacing between the incidence angles.

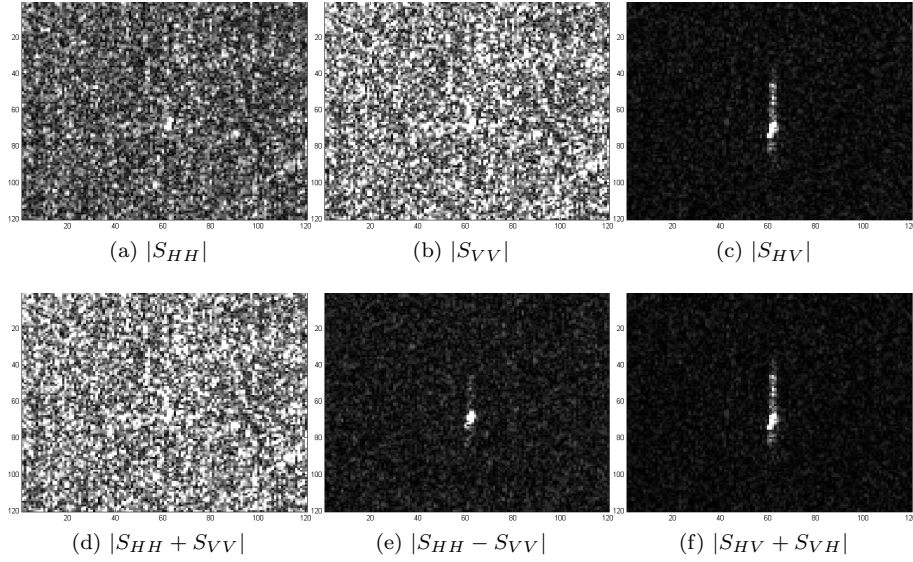


Figure 6.4: Target 10, Ocean prince, in different polarization channels and Pauli decomposition components. RADARSAT-2 Data and Products ©MacDONALD, DETTWILER AND ASSOCIATES LTD. (2010) - All Rights Reserved

Table 6.5: Incidence angles for target 1 - 16.

Image	Target	θ [deg]
I1	1	45,289
I1	2	45,356
I1	3	45,274
I1	4	45,221
I1	5	45,226
I2	6	27,119
I2	7	27,003
I2	8	26,914
I2	9	26,193
I2	10	27,113
I3	11	45,364
I3	12	45,288
I3	13	45,231
I3	14	45,403
I3	15	45,249
I3	16	44,742

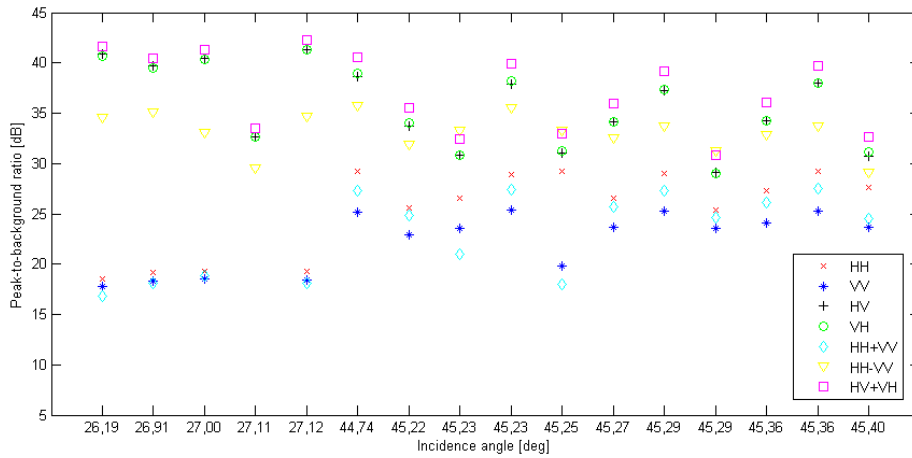


Figure 6.5: PBR as function of incidence angle.

In figure 6.5, and by comparison with table 6.5, we see that the first five points are the targets from I2, with incidence angles in the range $26, 19^\circ - 27, 12^\circ$. Except for target 10 at $27, 11^\circ$, the contrast values for these targets are very similar. $|S_{HV}|$, $|S_{VH}|$ and $|S_{HV} + S_{VH}|$ give high values ~ 40 dB, while $|S_{HH}|$, $|S_{VV}|$ and $|S_{HH} + S_{VV}|$ give low values ~ 18 dB. $|S_{HH} - S_{VV}|$ lies in between these two groups. As described in section 3.1, the ocean backscatter is highest at low incidence angles and for co-polarization, and this can explain the low contrasts produced by the co-polarization channels at the lowest incidence angles.

For the larger incidence angles between $44, 74^\circ$ and $45, 40^\circ$, the ratios vary a lot more from target to target. If we compare the contrasts of the targets at $\sim 27^\circ$ to the ones at $\sim 45^\circ$, we see that

the best channels with respect to contrast, i.e. $|S_{HV}|$, $|S_{VH}|$ and $|S_{HV} + S_{VH}|$, produce a higher PBR contrast at low incidence angles than for larger angles. The opposite is seen for the low contrast polarizations $|S_{HH}|$, $|S_{VV}|$ and $|S_{HH} + S_{VV}|$, where the PBR contrasts increase from low to high incidence angles, possibly due to lower sea clutter at larger angles. No clear trend as to how $|S_{HH} - S_{VV}|$ varies with incidence angle is seen.

We also note that as the incidence angle increase, the separation between $|S_{HH}|$ and $|S_{VV}|$ increase.

The TBRs as function of incidence angle are seen in figure 6.6. We can see that, like PBR, the TBR has little variation between the targets with low incidence angles, while it varies more at the larger angles. We also see that

for TBR in co-polarization channels and $|S_{HH} + S_{VV}|$, the contrast is enhanced from low incidence angles to higher incidence angles. The cross-polarization channels, including $|S_{HV} + S_{VH}|$ however, does not show one clear trend.

Several papers have proposed *break point angles* where co-polarization contrast exceeds cross-polarization contrast (see section 3.2.1). From the results of this

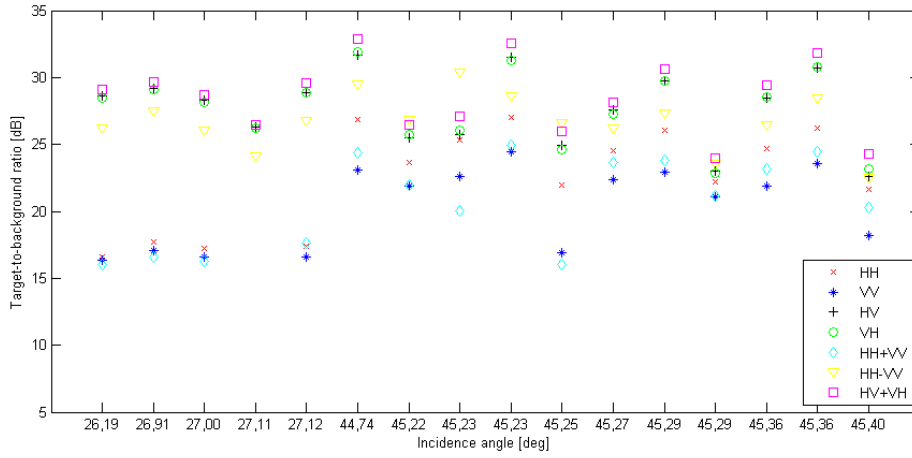


Figure 6.6: TBR as function of incidence angle.

project presented so far, no such break point can be seen.

For a true comparison as to how PBR and TBR are affected by incidence angle, the same ship with the same orientation should be studied at different incidence angles.

Comparison of cross-polarization and co-polarization

To better show how co-polarization and cross-polarization respond to differences in incidence angles, $|S_{VV}|$ is plotted together with $|S_{VH}|$ in figure 6.7, and $|S_{HH}|$ with $|S_{HV}|$ in figure 6.8. The plots are divided into "small" and "large" angles, meaning the smallest ($\sim 27^\circ$) and largest ($\sim 45^\circ$) angles of this data set.

In both figure 6.7 and 6.8, we see a clear difference between co-polarization and cross-polarization for small incidence angles, for both TBR and PBR. The cross-polarization contrasts are much larger than what we see in the corresponding co-polarization channels, and the difference in PBR are more than 20 dB at the highest.

In figure 6.7(b), we see that for PBR at large angles, the separations between the polarizations are not so large anymore, but all $|S_{VH}|$ values are still higher than all $|S_{VV}|$ values. For TBR, in figure 6.7(d), the co- and cross-polarization values have started to overlap, and are more mixed.

In figure 6.8, we see the same as in 6.7, only the co- and cross-polarizations are also starting to overlap for PBR, and the TBRs are even more mixed. However, for each individual target, cross-polarization contrast are in all cases larger than co-polarization contrast. Even though no break point angles as pointed out by others were found in this study, there is no doubt that

cross-polarization contrasts are superior to co-polarization contrasts at low incidence angles $\sim 27^\circ$, but less so at higher incidence angles $\sim 45^\circ$. Our results suggests that the contrast measures based on co-polarization and cross-polarization are more mixed for the TBR than for the PBR.

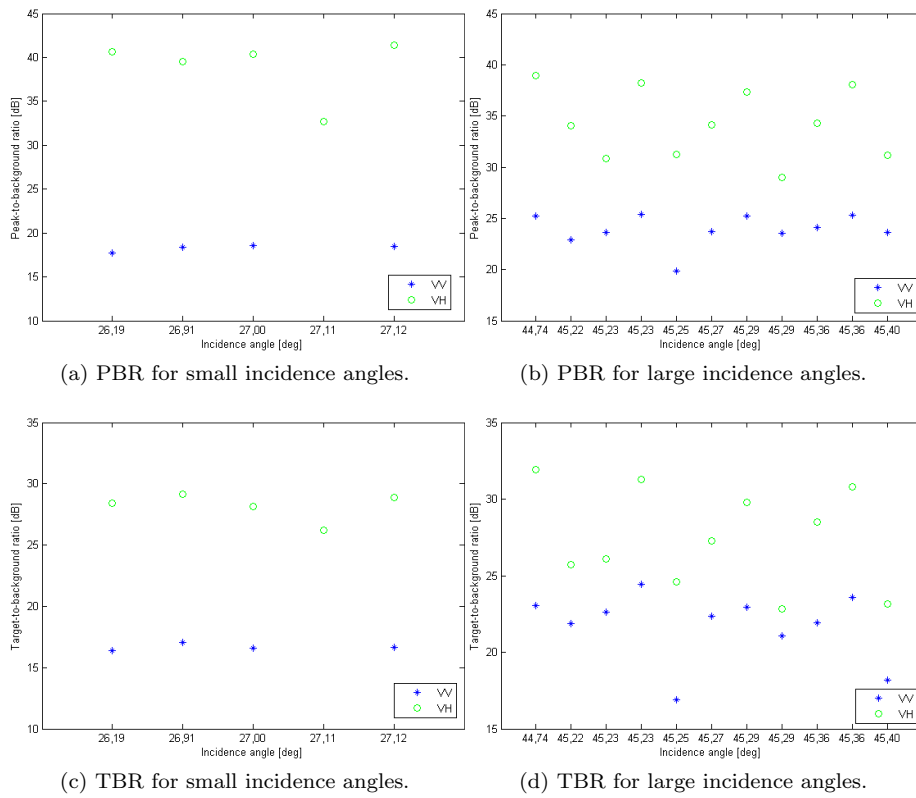


Figure 6.7: PBR and TBR for VV and VH polarization at different incidence angles.

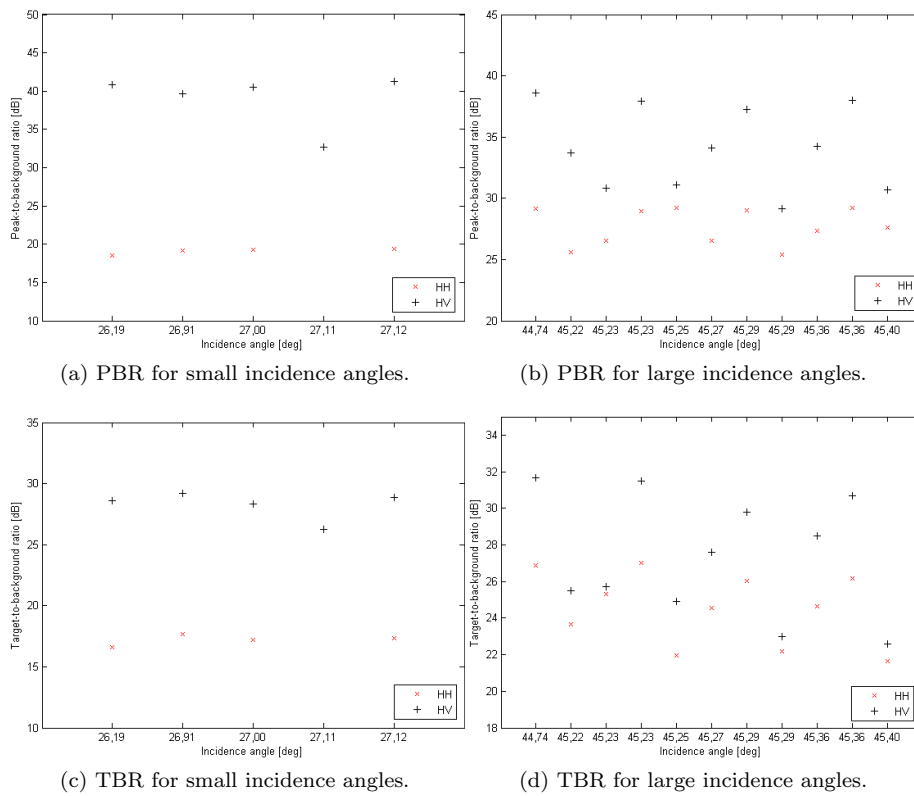


Figure 6.8: PBR and TBR for HH and HV polarization at different incidence angles.

Comparison of repeated target acquisitions

Some of the targets are present in more than one image, as can be seen in table 5.5. To investigate how the appearance of one target change from image to image, i.e. with respect to imaging geometry and sea state, the PBR and TBR for the repeating targets are gathered in table 6.6 - 6.9. Three and three rows (two in the case of Aker Spitsbergen and Island Wellserver), one for each image, are compared, and the image with the highest contrast for each polarization component is marked with yellow for each polarization.

Table 6.6: Contrast measures in dB for Ocean Prince in different images.

	$ S_{HH} $	$ S_{VV} $	$ S_{HV} $	$ S_{VH} $	$ S_{HH}+S_{VV} $	$ S_{HH}-S_{VV} $	$ S_{HV}+S_{VH} $
I1, PBR	25,42	23,52	29,12	29,01	24,65	31,27	30,84
I2, PBR	-	-	32,69	32,65	-	29,50	33,50
I3, PBR	27,61	23,64	30,70	31,20	24,48	29,07	32,70
I1, TBR	22,17	21,07	23,01	22,83	21,17	23,54	24,00
I2, TBR	-	-	26,27	26,23	-	24,15	26,49
I3, TBR	21,63	18,18	22,59	23,18	20,25	22,56	24,32

From table 6.6, we can see some kind of pattern between the images and polarizations. The contrasts in $|S_{HV}|$, $|S_{VH}|$ and $|S_{HV} + S_{VH}|$ are higher in I2 (i.e. the lowest incidence angle) compared to the corresponding measures in I1 and I3. For $|S_{HH} + S_{VV}|$, $|S_{HH}|$ and $|S_{VV}|$, no pixels were segmented out in I2, hence the contrast is best in either I1 or I3. $|S_{HH} - S_{VV}|$ is best in I1 and I2 for PBR and TBR respectively.

Figure 6.9 shows the contrast ratios for Ocean Prince as function of incidence angle. At the lowest incidence angle, no pixels are segmented out for $|S_{HH}|$, $|S_{VV}|$ and $|S_{HH} + S_{VV}|$, so these are not shown in the figure.

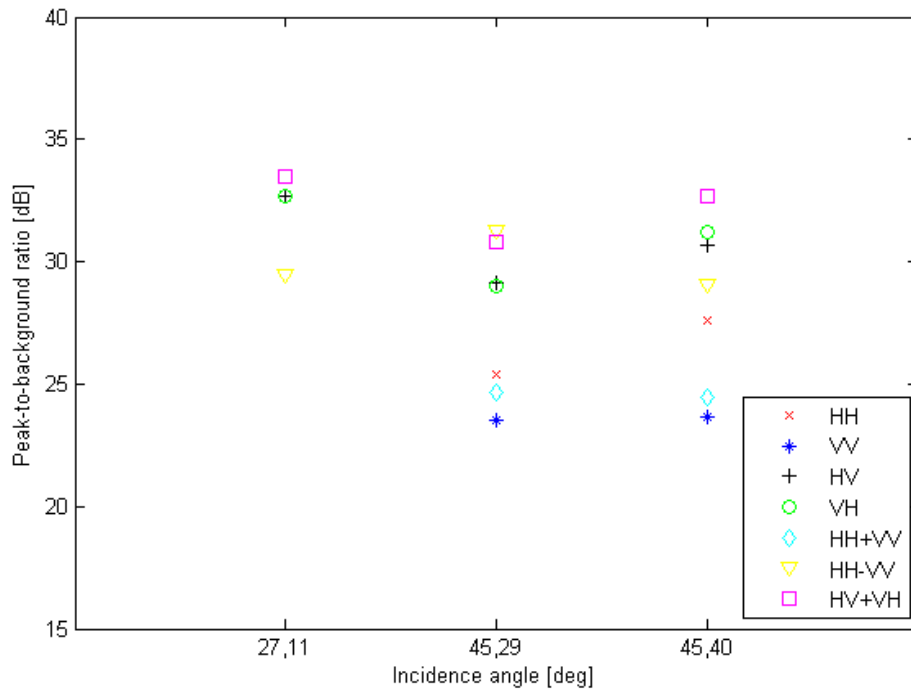
From figure 6.9, we see that the lowest angle gives the best contrasts for both PBR and TBR. $|S_{HH}|$, $|S_{VV}|$ and $|S_{HH} + S_{VV}|$ contrasts increase from the smallest incidence angle to the larger ones (at least we can look at it as an increase since no pixels were segmented out at the lowest angle), while cross-polarization channels and $|S_{HV} + S_{VH}|$ decrease.

From image I1 (at 45, 29°) to I3 (at 45, 40°), all polarizations, except $|S_{HH} - S_{VV}|$ and $|S_{HH} + S_{VV}|$ increase for PBR, and all polarizations except $|S_{HV} + S_{VH}|$ and $|S_{VH}|$ decrease for TBR. In general, the differences between incidence angles in I1 and I3 are probably too small to be able to detect any incidence angle dependency. The differences between these two acquisitions are probably due to some other factor, e.g. sea condition or ship orientation.

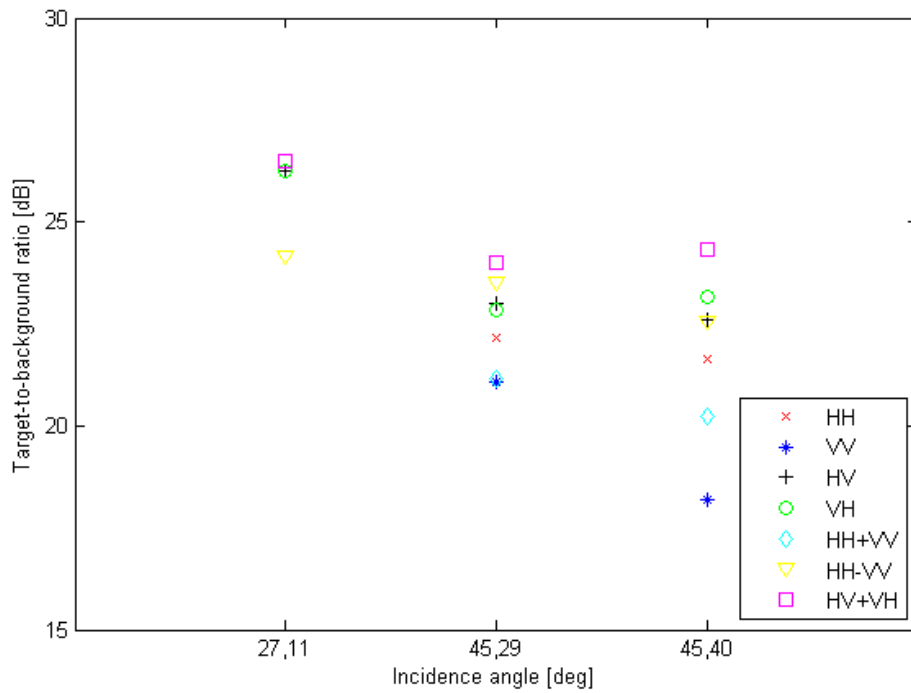
Table 6.7 and figure 6.10 show how PBR and TBR vary for the ship Norne in different images and at different incidence angles.

In table 6.7, we can see mainly the same trend as for Ocean Prince regarding the strongest PBR for each polarization. The difference is that for Norne, image I1 never gives the best result, and $|S_{HH} + S_{VV}|$, $|S_{HH}|$ and $|S_{VV}|$ has the largest contrast in I3. For the Norne TBR however, image I3 gives the highest ratio for all components.

Figure 6.10 shows how PBR and TBR for Norne vary between the three



(a) PBRs for Ocean Prince in the different images, from left: I2, I1, I3.



(b) TBRs for Ocean Prince in the different images, from left: I2, I1, I3.

Figure 6.9: Contrast measures for Ocean Prince in different images and at different incidence angles.

Table 6.7: Contrast measures in dB for Norne in different images.

	$ S_{HH} $	$ S_{VV} $	$ S_{HV} $	$ S_{VH} $	$ S_{HH}+S_{VV} $	$ S_{HH}-S_{VV} $	$ S_{HV}+S_{VH} $
I1, PBR	27,32	24,14	34,24	34,27	26,17	32,90	36,06
I2, PBR	19,33	18,45	41,30	41,36	18,13	34,73	42,30
I3, PBR	29,22	25,29	38,00	38,03	27,48	33,67	39,71
I1, TBR	24,66	21,92	28,48	28,51	23,18	26,43	29,46
I2, TBR	17,37	16,62	28,85	28,89	17,67	26,80	29,56
I3, TBR	26,18	23,60	30,70	30,81	24,44	28,48	31,87

images. In figure 6.10, we see again that the lowest incidence angle yields the highest PBR contrast (with $|S_{HV}|$, $|S_{VH}|$ and $|S_{HV}+S_{VH}|$), and also the lowest contrast (with $|S_{HH}|$, $|S_{VV}|$ and $|S_{HH}+S_{VV}|$). The latter channels increase through all three incidence angles, while $|S_{HV}|$, $|S_{VH}|$ and $|S_{HV}+S_{VH}|$ decrease from 27, 11° to the angles $\sim 45^\circ$, but increase between the last two.

TBR shows the best contrasts at the highest incidence angle, in all polarization channels and decomposition components. $|S_{HV}|$, $|S_{VH}|$, $|S_{HH}-S_{VV}|$ and $|S_{HV}+S_{VH}|$ show a small decrease from I2 to I1, but other than that we see a general increase with angle.

In the case of Norne, I1 and I3 have the same incidence angle of 45, 36°, so in this case, the incidence angles should definitely not affect the result here. Still, we see an increase in contrast between these two, for all polarizations and in both TBR and PBR. This indicates there is some other external influence, e.g. sea state, that causes an increase in contrast. This subject will be touched upon later.

A comparison of two of the acquisitions of Norne is seen in figure 6.11. Target 6 is from I2 ($\theta \sim 27^\circ$), and target 11 is from I3 ($\theta \sim 45^\circ$). The image have been scaled before plotting, so that the values lie in the range [0 255].

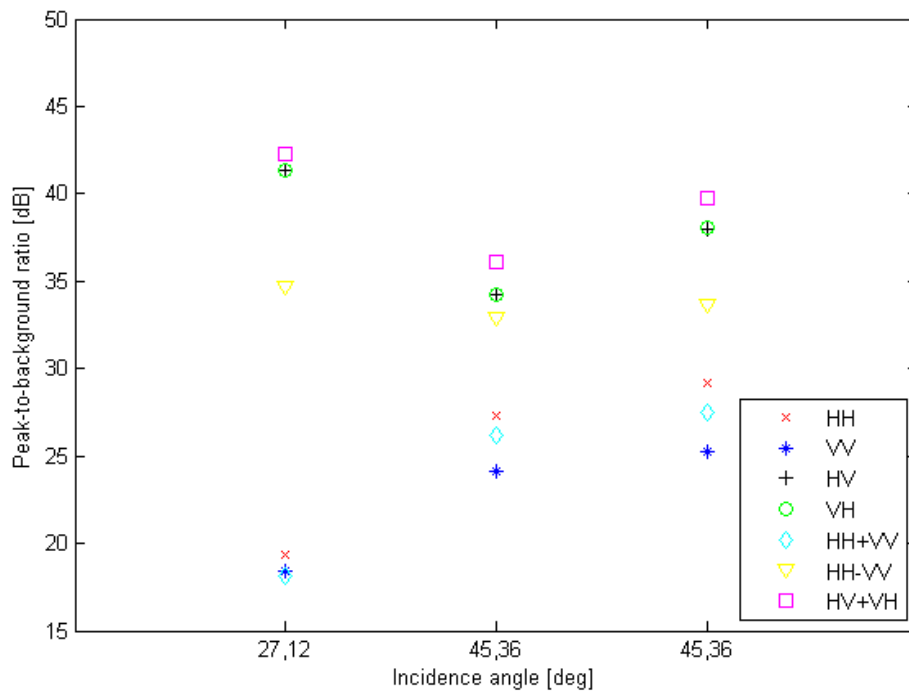
In figure 6.11, we see how the contrast in co-polarization is enhanced at the largest incidence angle, compared to the lowest angle, due to the decrease in ocean clutter. Less difference between the two images are seen in $|S_{HV}|$ and $|S_{HV}+S_{VH}|$, but target 11 seem to be less smeared than target 6.

Contrast measures for Aker Spitsbergen and Island Wellserver are shown in table 6.8 and 6.9 respectively.

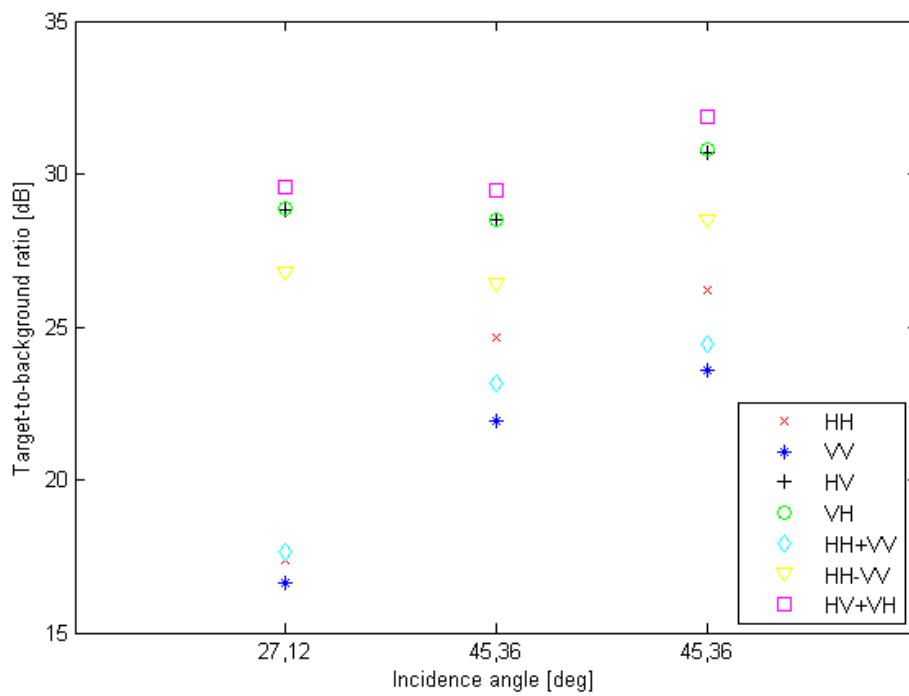
Table 6.8: Contrast measures in dB for Aker Spitsbergen in different images.

	$ S_{HH} $	$ S_{VV} $	$ S_{HV} $	$ S_{VH} $	$ S_{HH}+S_{VV} $	$ S_{HH}-S_{VV} $	$ S_{HV}+S_{VH} $
I2, PBR	19,20	18,33	39,70	39,49	18,15	35,12	40,45
I3, PBR	28,94	25,39	37,93	38,21	27,44	35,53	39,88
I2, TBR	17,69	17,07	29,20	29,14	16,57	27,47	29,70
I3, TBR	27,03	24,42	31,48	31,28	24,95	28,65	32,59

Aker Spitsbergen and Island Wellserver are only present in image I2 and I3, and as we can see from table 6.8 and 6.9, they show the same patterns as



(a) PBRs for Norne in the different images, from left: I2, I1, I3.



(b) TBRs for Norne in the different images, from left: I2, I1, I3.

Figure 6.10: Contrast measures for Norne in different images and at different incidence angles.

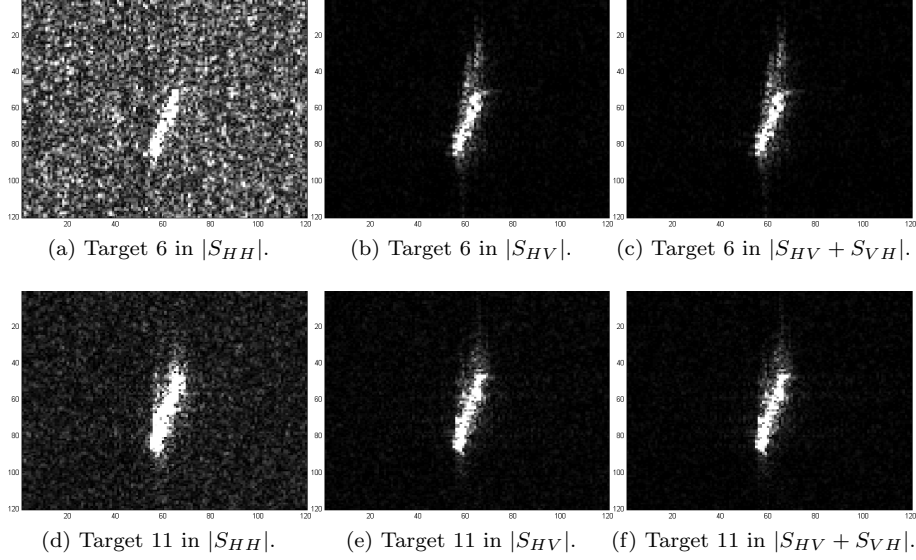


Figure 6.11: Comparison of two acquisitions of Norne. RADARSAT-2 Data and Products ©MacDONALD, DETTWILER AND ASSOCIATES LTD. (2010) - All Rights Reserved

Table 6.9: Contrast measures in dB for Island Wellserver in different images.

	$ S_{HH} $	$ S_{VV} $	$ S_{HV} $	$ S_{VH} $	$ S_{HH} + S_{VV} $	$ S_{HH} - S_{VV} $	$ S_{HV} + S_{VH} $
I2, PBR	19,27	18,53	40,46	40,36	18,90	33,03	41,30
I3, PBR	29,02	25,23	37,24	37,37	27,32	33,71	39,14
I2, TBR	17,21	16,60	28,34	28,16	16,26	26,09	28,68
I3, TBR	26,04	22,96	29,78	29,78	23,81	27,33	30,61

to where the best contrast for each polarization is found. For PBR, I3 have highest values for co-polarization and $|S_{HH} + S_{VV}|$ and $|S_{HH} - S_{VV}|$, while cross-polarization and $|S_{HV} + S_{VH}|$ have the best contrast in I2. For TBR, all polarization channels and decomposition components produce the best contrasts in I3.

Contrast as function of incidence angle for Aker Spitsbergen and Island Wellserver are shown in figure 6.12 and figure 6.13.

Figure 6.12 and 6.13 look very similar. For PBR, $|S_{HV}|$, $|S_{VH}|$ and $|S_{HV} + S_{VH}|$ decrease from small to large incidence angle, while $|S_{HH}|$, $|S_{VV}|$ and $|S_{HH} + S_{VV}|$ increase. For TBR, all polarizations produce best contrast at the highest incidence angle. Aker Spitsbergen is a rig, while Island Wellserver is a ship, and table 6.8 and 6.9 and figure 6.12 and 6.13 indicates that the two target types show similar behaviour with changing incidence angles.

A few generalizations can be made based on the four targets discussed here.

All four targets investigated show increasing contrast in both PBR and TBR from small incidence angles $\sim 27^\circ$ to large incidence angles $\sim 45^\circ$ in $|S_{HH}|$, $|S_{VV}|$ and $|S_{HH} + S_{VV}|$. For all four, we also see a varying degree of decrease in PBR for $|S_{HV}|$, $|S_{VH}|$ and $|S_{HV} + S_{VH}|$ from small angles to large angles, while TBR for these polarizations increase with incidence angles for three of the ships.

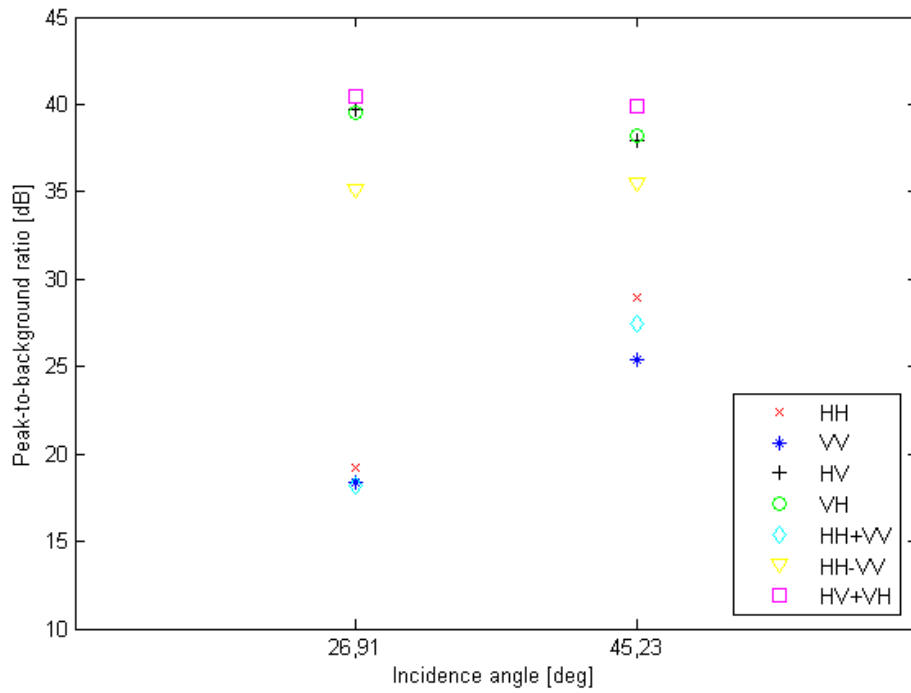
Contrast measures and relation to target size

As was indicated earlier in the discussion, target size may influence how strong contrast a target produces. As we have ground truth information for this data set, the size of each target is known, and are given in table 5.5. Figure 6.14 shows the contrast as function of size for the targets in each image. The length is used as the size measure, and "double" targets are not included.

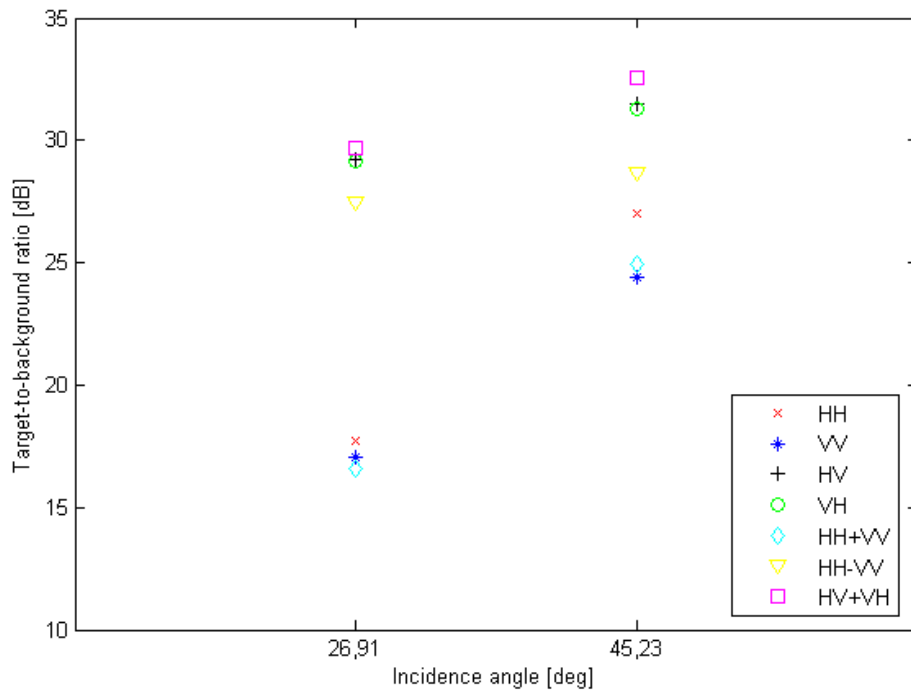
When looking at figure 6.14(a), 6.14(c) and 6.14(e), it looks like PBR for $|S_{HV}|$, $|S_{VH}|$ and $|S_{HV} + S_{VH}|$ increase with length. At least we can see some distinction between the smallest targets and the larger ones. In figure 6.14(a), the first two targets have lower values than the last two. Likewise, the first target in figure 6.14(c) and the first two targets in figure 6.14(e) differ from the other targets in each image. When looking at figure 5.3 - 5.5, we can see that I1 contains two small targets (target 1 and 5), I2 one (target 10) and I3 two (target 14 and 15), so this is consistent with figure 6.14. In this context 'small' just means considerably smaller than the other targets. For convenience, we will label targets 1, 5, 10, 14 and 15 as small, and the targets in data set 1 with length ≥ 90 m will hence be described as large. Figure 6.3 and 6.4 show how a large ship, Norne (260 m), and a small ship, Ocean Prince (64,5 m), appear in image I2.

The co-polarization channels, $|S_{HH} - S_{VV}|$ and $|S_{HH} + S_{VV}|$ does not show a similar, clearly increasing trend as the one seen for the other polarizations. They act differently from image to image, but mostly show some increase towards larger targets, or little variation at all.

When looking at the TBRs in figure 6.14(d) and 6.14(f), we see an increase in contrast from small to large targets in all polarizations. An increase in $|S_{HV}|$, $|S_{VH}|$ and $|S_{HV} + S_{VH}|$ is also seen in figure 6.14(b), while the other

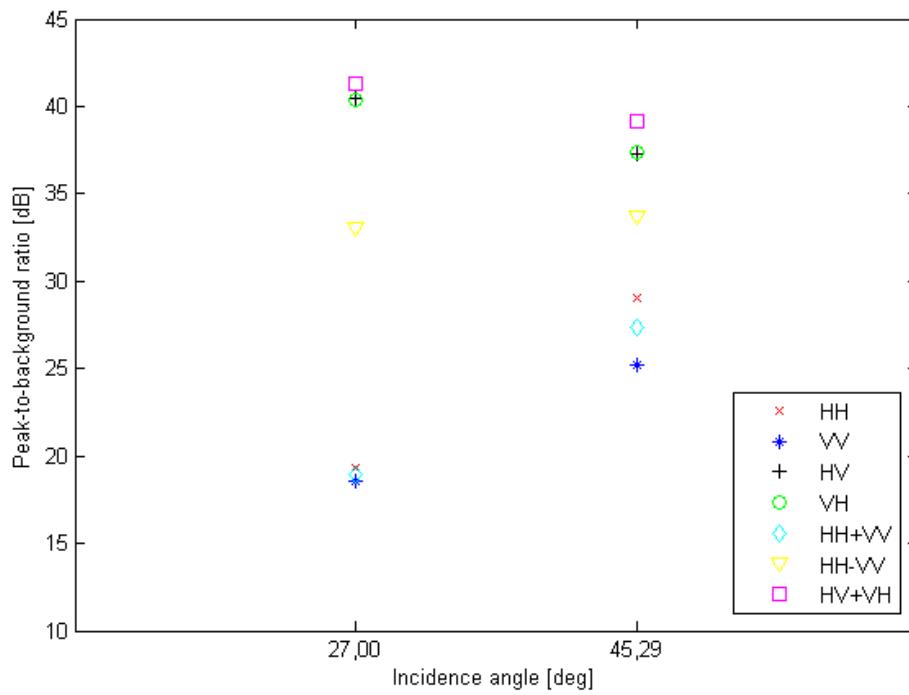


(a) PBRs for Aker Spitsbergen in the different images, from left: I2, I3.

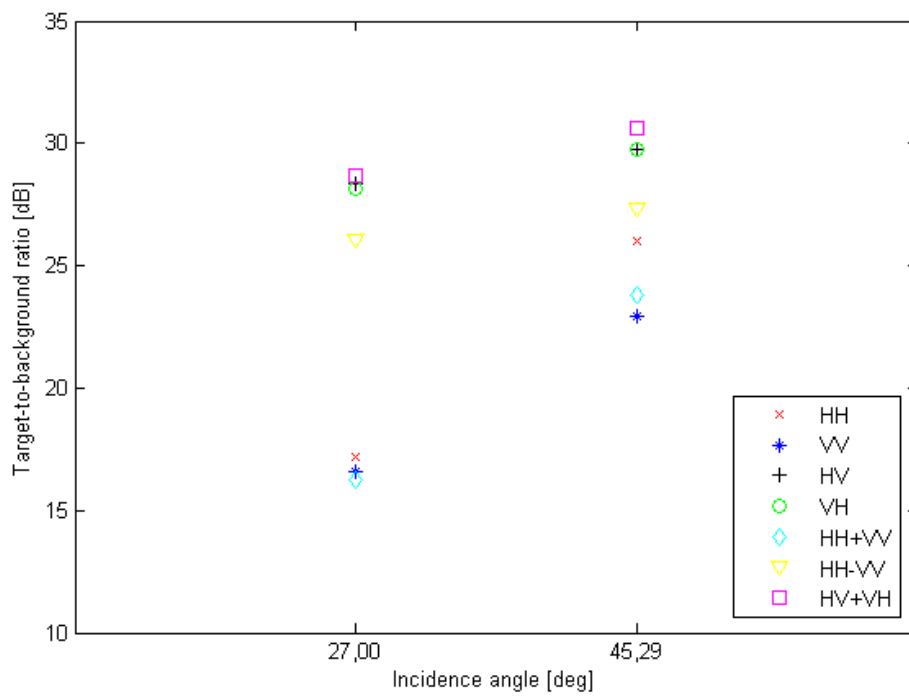


(b) TBRs for Aker Spitsbergen in the different images, from left: I2, I3.

Figure 6.12: Contrast measures for Aker Spitsbergen in different images and at different incidence angles.

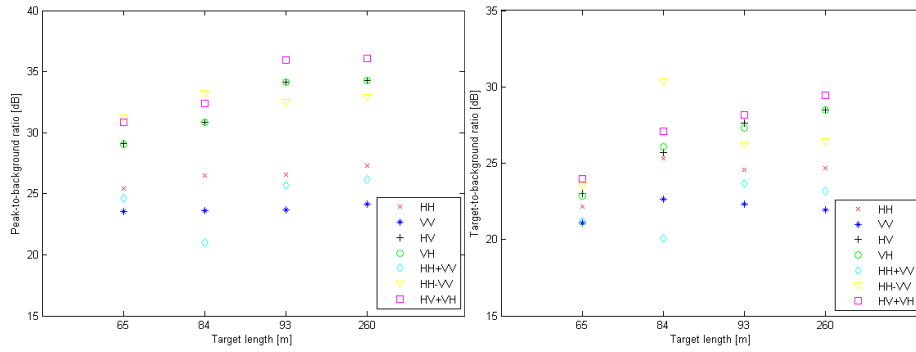


(a) PBRs for Island Wellserver in the different images, from left: I2, I3.

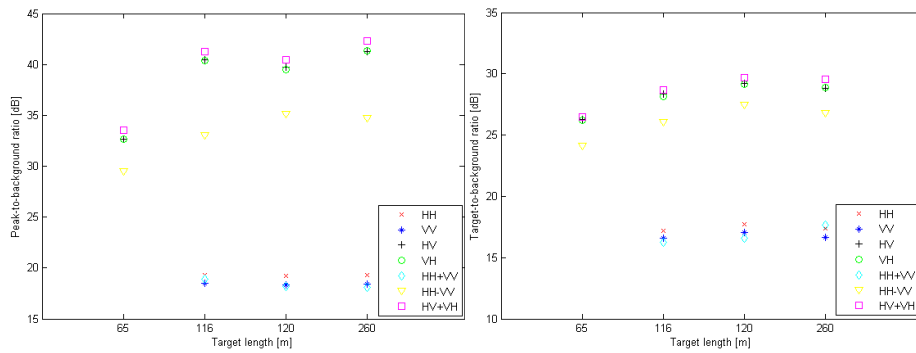


(b) TBRs for Island Wellserver in the different images, from left: I2, I3.

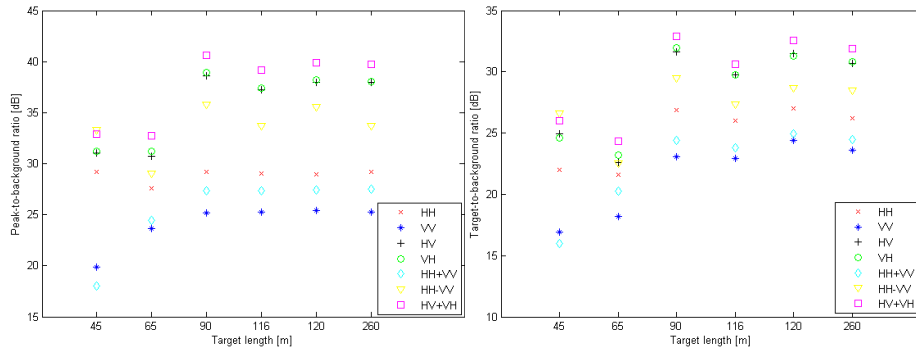
Figure 6.13: Contrast measures for Island Wellserver in different images and at different incidence angles.



(a) PBRs for I1 as function of target length. (b) TBRs for I1 as function of target length.



(c) PBRs for I2 as function of target length. (d) TBRs for I2 as function of target length.



(e) PBRs for I3 as function of target length. (f) TBRs for I3 as function of target length.

Figure 6.14: Contrast measures as function of target length.

polarizations in I1 do not have a clear trend for TBR.

Within the group of large targets, the size varies a lot, but the PBR for these targets seems to be almost constant for all polarizations and images. Also the TBR shows little difference between the largest ships. When looking at figure 5.3 - 5.5, we can see that even though it is easy to discriminate the smallest targets from the largest, the differences between the largest targets are small. Norne is 260 m and Aker Spitsbergen is 120 m, but still it is difficult to see that one is larger than the other in any of the images. Factors such as orientation of the ship, construction material and degree of smearing can affect how large a target appears, and how much energy is backscattered, making it difficult to see size differences from the images.

Based on this discussion, we can conclude that

larger targets often have stronger PBR than smaller ones in $|S_{HV}|$, $|S_{VH}|$ and $|S_{HV} + S_{VH}|$, but not necessarily so in the other polarization channels and decomposition components. The size between targets may also vary quite a lot with no significant differences in PBR. Also the TBR shows an increase with target size, but to a smaller degree, so it seems like PBR is more influenced by ship size than TBR.

These findings agree with other research indicating that the contrast increases with size, especially for cross-polarization (see section 3.2.1). The higher dependency on size of PBR compared to TBR can be utilized in e.g. target classification, where size may be an important feature, and PBR can indicate differences in size.

Contrast measures and relation to weather conditions

As seen from table 5.6, the wind conditions on the three dates of data acquisition vary slightly. I1 and I2 are obtained in 7 m/s wind, with wave heights of 2 m and 1 m respectively. I3 was obtained in 5 m/s wind and observed wave height was only 0,5 m. These are the wave heights observed at Heidrun, which is the closest observation point we have (see figure 5.7), and also the most accurate one.

If we look at figure 6.1 and 6.2, we see that the contrast ratios for the targets from I3 often are a little higher than for the targets of image I1, a few dB for all polarizations. At least for the large targets; target 2, 3 and 4 from I1 versus target 11, 12, 13 and 16 from I3. In figure 6.9 and 6.10, we compared the same ship at different incidence angles. Both of these figures show an increase from I1 to I3 for all PBR and TBR values for Norne, and for most PBRs and some TBRs for Ocean Prince. The calmer sea state in I3 is a possible explanation for the increase we see in contrast compared to I1.

The wind strength is believed to affect PBR and TBR, as strong winds will cause rougher sea surface and increased ocean clutter, resulting in weaker contrast between marine targets and ocean background. We see indications of this in our experiment.

Image I1 and I3 have approximately the same incidence angles, but are taken with different modes, which could also affect the contrast measures. I1 is Fine Quad, which gives a little better resolution than the Standard Quad mode of I3.

In section 3.2, it was stated that ship contrast should increase with resolution. As it is I3, with the lowest resolution, that produce the higher contrast, this indicates that the image mode is not the reason for the higher contrast of I3, strengthening the theory that the sea state is the force behind.

6.2.2 Data set 2: Ships in sea ice background

Data set 2 consists of three images containing ground truthed ships in sea ice background, as described in section 5.4. The PBR and TBR values for the four targets, calculated as described in section 4.6.2 and 4.6.3, are given in table 6.10.

Table 6.10: PBR and TBR in dB for target 17 - 20.

Image	Target	Contrast	$ S_{VV} $	$ S_{VH} $
I4	17	PBR	47,07	63,67
I4	18	PBR	46,41	54,31
I5	19	PBR	45,31	64,67
I6	20	PBR	50,22	65,07
Mean		PBR	47,25	61,93
I4	17	TBR	17,98	20,51
I4	18	TBR	17,54	17,79
I5	19	TBR	17,80	21,12
I6	20	TBR	18,01	19,66
Mean		TBR	17,83	19,77

Table 6.10 clearly shows that the

contrast between ship and sea ice is better in the cross-polarization channel than in co-polarization, as all targets show the best contrast in $|S_{VH}|$ for both PBR and TBR.

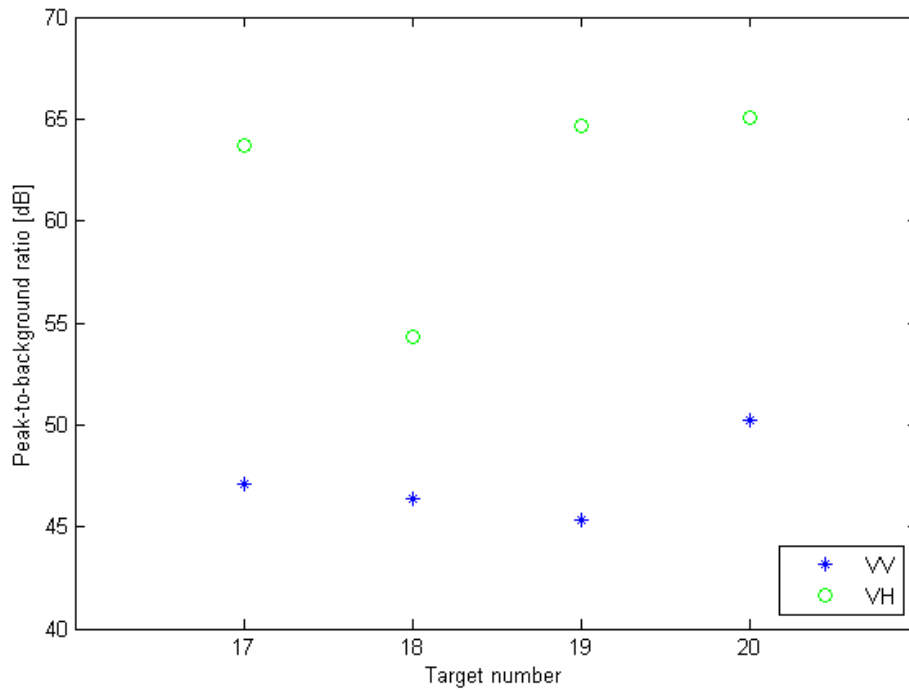
However, the differences between the mean value of $|S_{VV}|$ and $|S_{VH}|$ are smaller than the difference between these two polarizations in the first data set, where the background was composed of ocean areas. PBR and TBR as function of target number is seen in figure 6.15.

In figure 6.15, we clearly see the enhancement of contrast in $|S_{VH}|$ compared to $|S_{VV}|$. Target 18 has lower values for $|S_{VH}|$ than the rest of the targets, but other than that, the contrast values vary little. As was seen for data set 1, the difference between co- and cross-polarization is less for TBR than for PBR.

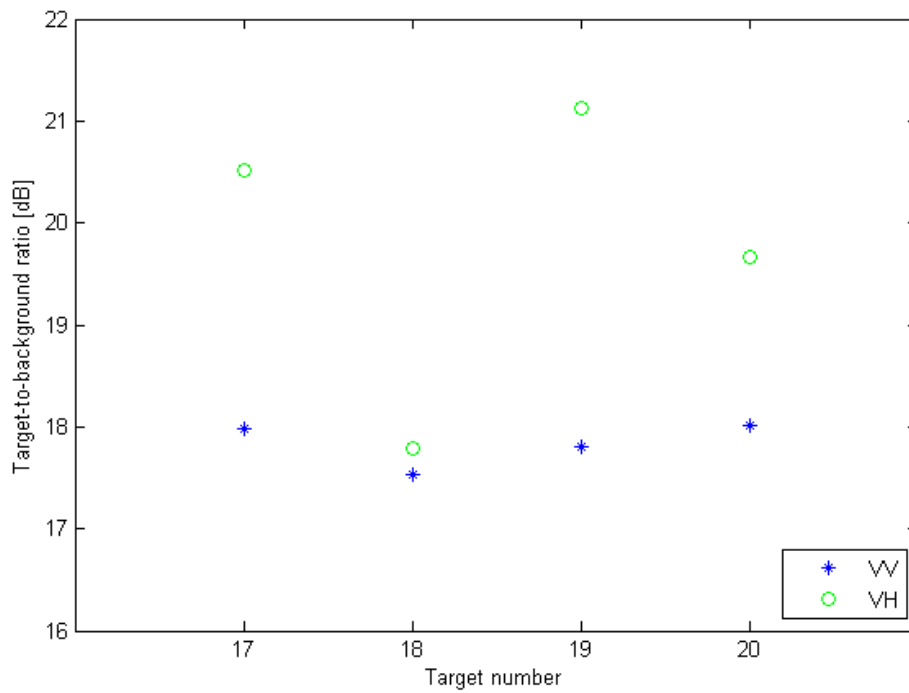
Contrast measures and relation to incidence angle

Incidence angle for each ship was calculated as described in section 4.4, and are given in table 6.11. PBR and TBR as function of incidence angle is seen in figure 6.16.

When looking at figure 6.16(a), it looks like the cross-polarization PBR increases with incidence angle. Except for target 19 at $36,25^\circ$, so does co-polarization.

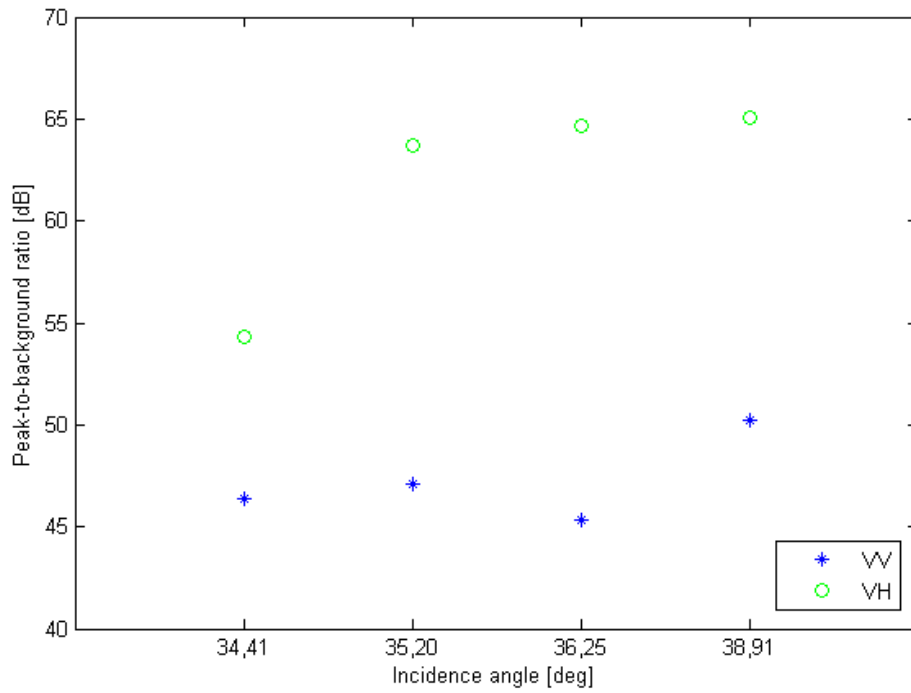


(a) PBR as function of target number.

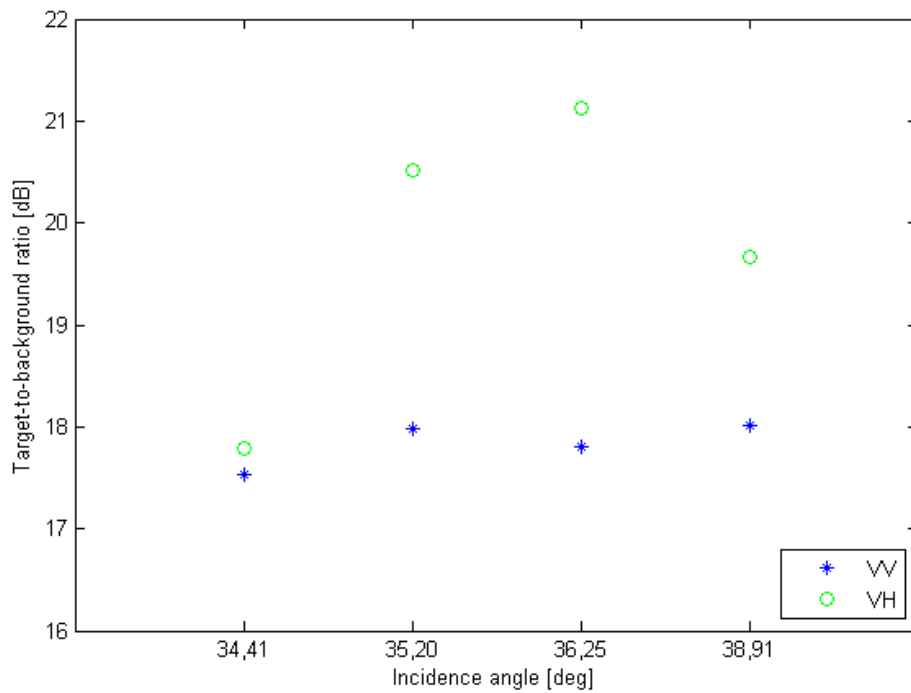


(b) TBR as function of target number.

Figure 6.15: Contrast measures as function of target number.



(a) PBR as function of incidence angle.



(b) TBR as function of incidence angle.

Figure 6.16: Contrast measures as function of incidence angle.

Table 6.11: Incidence angles for target 17 - 20.

Image	Target	θ [deg]
I4	17	35,20
I4	18	34,41
I5	19	36,25
I6	20	38,91

In figure 6.16(b), we can see that TBR in cross-polarization increases for the first three targets, and then drop down. Co-polarization only shows small variations in TBR with incidence angle.

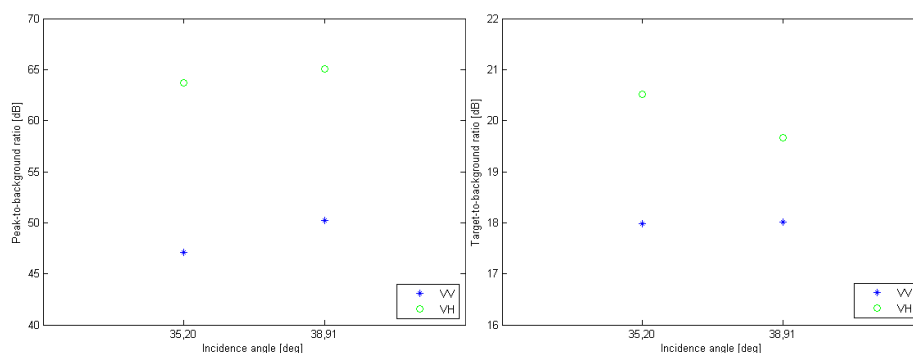
In section 3.3, it was stated that backscattering from sea ice will decrease with increasing incidence angles, but to different degrees depending on the ice type. This would give better contrast at larger incidence angles, and corresponds partially to what we see in figure 6.16.

We should note that target 17 (at 35, 20°) and target 18 (at 34, 41°) are in the same image, and many factors such as weather conditions and radar properties will be approximately the same for these two. Both PBR and TBR show an increase from target 18 to target 17 in both polarizations, possibly due to the slightly larger incidence angle. Based on this we can conclude that the

PBR and TBR for ships in sea ice increase with incidence angle to some extent, at least in cross-polarization. However, we have too little data to be able to draw a reasonable conclusion.

Comparison of repeated target acquisitions

Data set 2 contains two ships, K/V Svalbard and R/V Lance, each imaged twice. The repeated target acquisitions are compared in figure 6.17 and 6.18.



(a) PBR for K/V Svalbard; target 17 and 20. (b) TBR for K/V Svalbard; target 17 and 20.

Figure 6.17: Contrast measures for K/V Svalbard in different images and at different incidence angles.

In figure 6.17, we see that for PBR, both co- and cross-polarization increase

from $35,20^\circ$ to $38,91^\circ$ for K/V Svalbard. TBR however, decrease in cross-polarization and is almost constant in co-polarization.

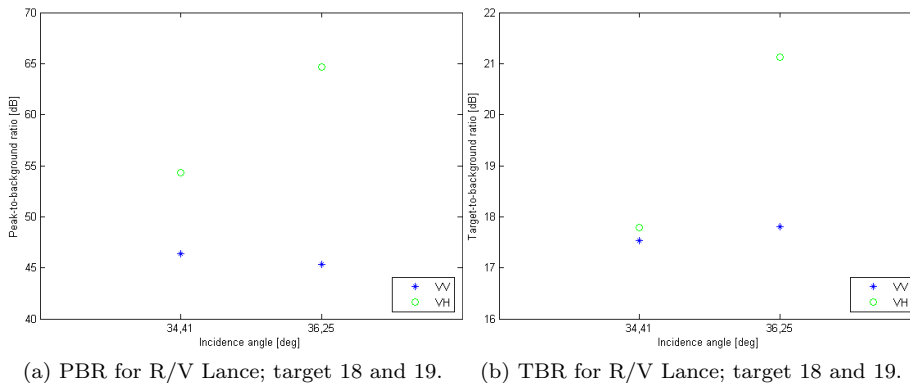


Figure 6.18: Contrast measures for R/V Lance in different images and at different incidence angles.

In figure 6.18, we see that for R/V Lance, cross-polarization contrast increase from the acquisition in I4 (at $34,41^\circ$) to I5 (at $36,25^\circ$) for both PBR and TBR. The increase could be due to larger incidence angles for target 19. Co-polarization shows a small decrease with incidence angle for PBR, and a small increase in TBR.

Based on the plot in figure 6.17 and 6.18, the only common trend was that

for the same ships imaged at different incidence angles, PBR increases with incidence angle in cross-polarization, while co-polarization shows little variation with angle.

Repeated acquisitions of K/V Svalbard (target 17 and 20) are seen in figure 6.19.

In figure 6.19, we see that the contrasts in the cross-polarization channels are better than in co-polarization channels. We also see that the background in the two co-polarization images looks different. Target 20 appears to have a more mixed background, with some darker regions, possibly due to open ocean areas. These background differences can produce some difference in the contrast measures. We would expect target 20 to get a lower background mean, and hence a larger contrast than target 17. In figure 6.17, a small increase from target 17 to 20 is seen for PBR, previously suggested caused by incidence angle. TBR however, does not show any increase for target 20 compared to target 17. The small increase in PBR may be due to incidence angle or background composition, but can also be due to random differences in the imaging.

Contrast measures and relation to target size

PBR and TBR as function of target length is seen in figure 6.20. As we only have two different ships, we only have two different ship lengths to compare. An average of the two measurements of each ship is included in the plot.

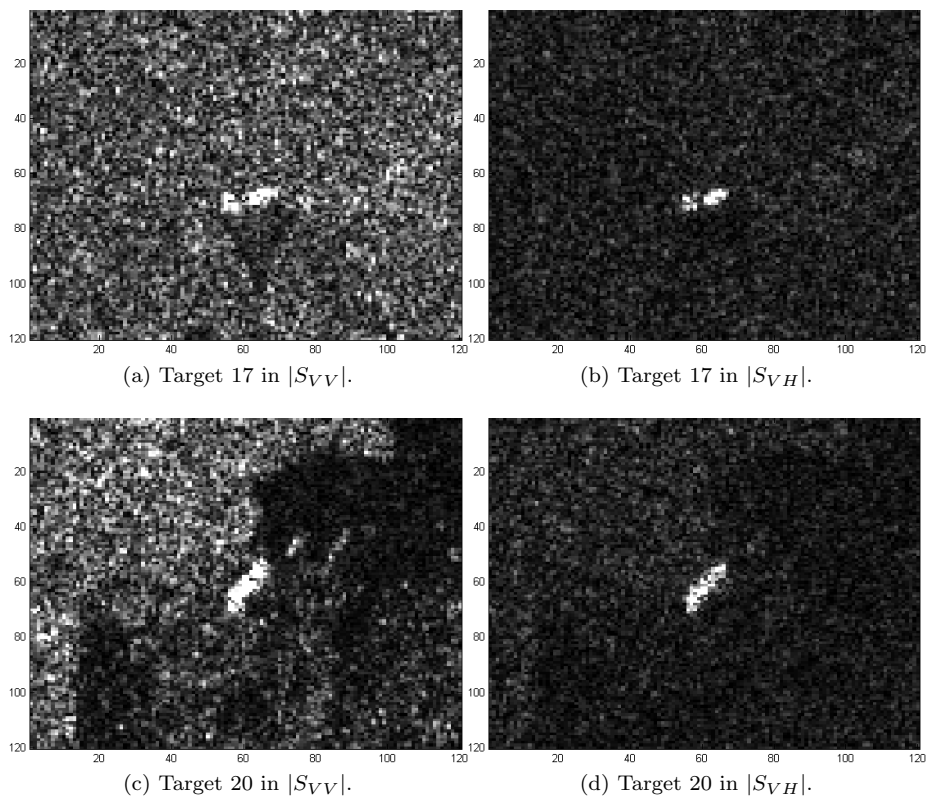
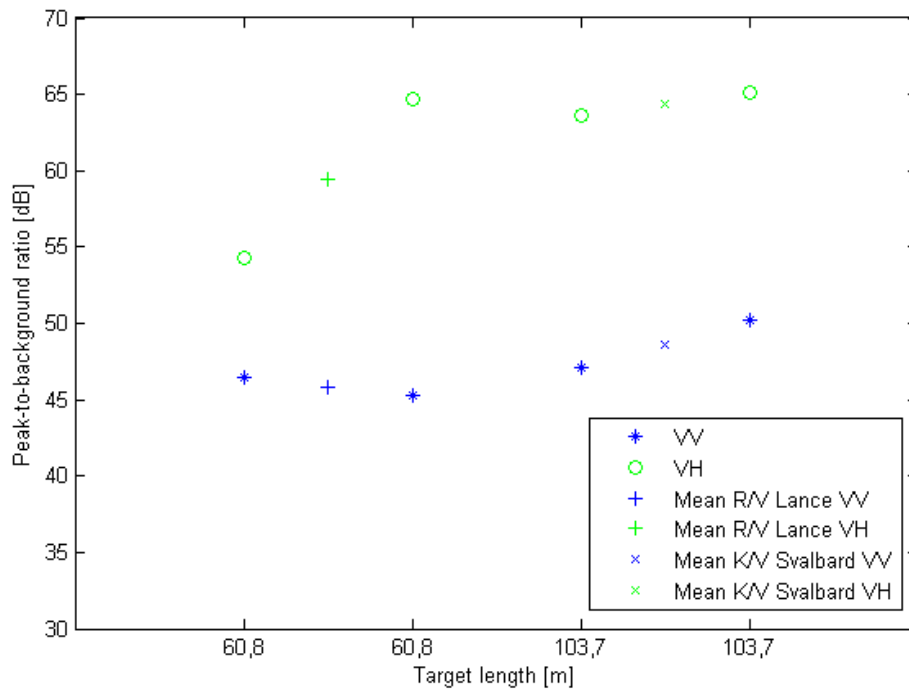
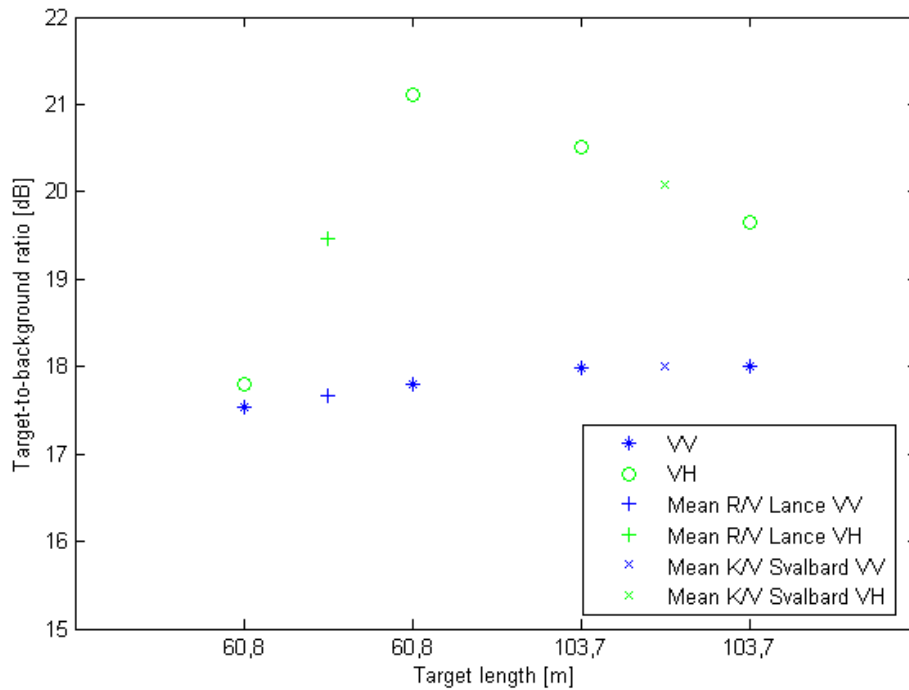


Figure 6.19: Comparison of two acquisitions of K/V Svalbard. RADARSAT-2 Data and Products ©MacDONALD, DETTWILER AND ASSOCIATES LTD. (2009) - All Rights Reserved



(a) PBR as function of ship length (from left to right: target 18, 19, 17 and 20).



(b) TBR as function of ship length (from left to right: target 18, 19, 17 and 20).

Figure 6.20: Contrast measures as function of ship length, including mean value of repeated acquisitions.

When looking at the plots in figure 6.20, it is difficult to make a conclusion based only on comparing the individual contrast measures. However, we see that the mean values in both polarizations increase from the smallest ship to the largest ship in both PBR and TBR.

In order to rule out some of the other factors that may influence the contrast, we can compare the two targets that were in the same image, target 17 and 18. We see that there is an increase from target 18 (60,8 m) to target 17 (103,7 m) in both polarizations for both PBR and TBR, which may be due to the size difference. This indicates

there might be a size dependency in the contrast between ships and sea ice background, producing a higher contrast as the target size increases. The difference is less for $|S_{VV}|$ than for $|S_{VH}|$.

It was noted earlier in this section, that this increase could be due to the increase in incidence angle. It is difficult to know what factor is most important, but it is likely that both size and incidence angle has an effect.

Contrast measures and relation to weather conditions

The weather conditions on the dates of image acquisitions could offer an alternative explanation as to how the contrast vary between the repeated target acquisitions.

As we know from section 5.4, the weather conditions on the two dates of acquisitions of target 17 and 20 were a little different. Measurements done on K/V Svalbard showed 7 m/s wind when I4 was obtained (using the measurement closest in time to image acquisition), and only 3 m/s at the time of imaging I6. When the background is composed of ocean areas, stronger winds can degrade the contrast as discussed in section 3.2.1. The effect of the wind on sea ice background may be different, but the decrease in wind is a possible reason for the slightly increase in PBR for target 20 (from I6) compared to target 17 (in I4).

If we look at the photos in figure 5.9(c) and 5.9(d), it looks like the ice is less dense at the time of imaging I6, corresponding to what we see in figure 6.19. This could also give rise to better contrast on this date, as a background composed of more ocean and less ice may give less background clutter levels, especially at calm winds. However, the photos are separated from the satellite images both in time and space, and can only be used as an indicator on the ice conditions. Due to the lower wind strength and the possibility of more open water at the time of imaging target 20, we could expect a rise in contrast, as we see in PBR. However, these explanations would be more likely if we had seen a similar increase in TBR, which we do not.

From section 5.9, we know that the wind strength measured at K/V Svalbard at the time of imaging of target 18 and 19 were 7 m/s and 12 m/s respectively, and the wave heights measured at BUOV2 were 1 m and 2,5 m. Measurements from R/V Lance itself were not available. As the contrast is best at the day of strongest wind, this indicates that the wind did not degrading the signal contrasts.

From figure 5.9(c), we know there were a lot of ice around the boat on the day of the I4 acquisition, at least 7 hours before the satellite image was acquired.

If there were less ice on the day of the I5 acquisition, this could explain the enhanced contrast that day.

From this it can be stated that

it looks like stronger winds might not result in a decrease in contrast when the background is composed of ice. The density of the sea ice surrounding the ship is likely to have an effect on the contrast.

6.2.3 Data set 3: Iceberg targets in mixed background

Data set 3 contains four single-polarization images from Antarctica containing icebergs, as described in section 5.5. The background is unknown, but seem to be composed by ice and possibly also some open ocean areas. The iceberg targets have a high variety in size and shape, and some examples are seen in figure 6.21. The images have been scaled so that the values lie in the range [0 255].

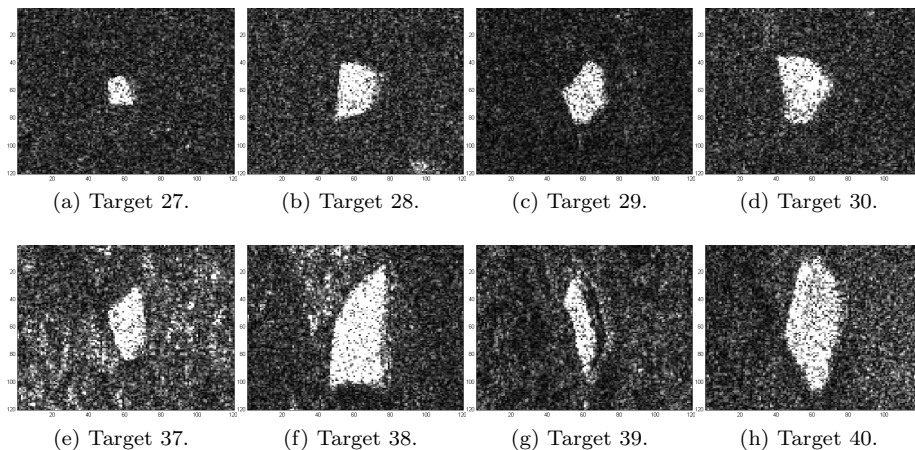


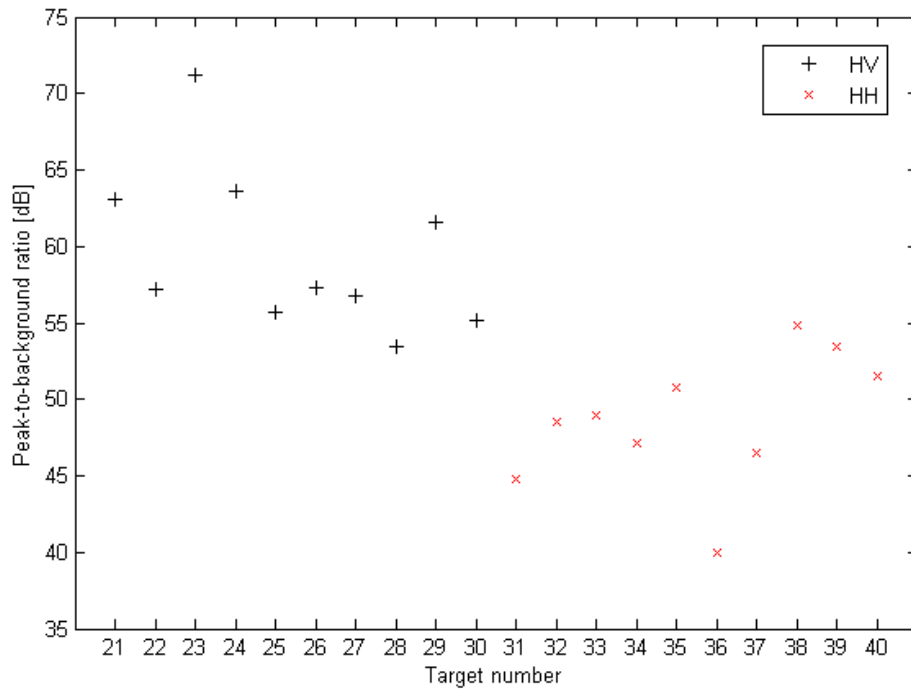
Figure 6.21: Examples of iceberg targets. (a)-(d) are in $|S_{HV}|$, (e)-(h) in $|S_{HH}|$. RADARSAT-2 Data and Products ©MacDONALD, DETTWILER AND ASSOCIATES LTD. (2010) - All Rights Reserved

The iceberg targets have been divided into two categories, small and large, as seen in table 5.11. Some icebergs were imaged twice, and have been labelled A-D. As described in section 4.2.2, the largest icebergs are segmented out a little differently than the others. This applies for both acquisitions of iceberg A, C and D. Table 6.12 summarizes the contrast measures of the targets selected from data set 3.

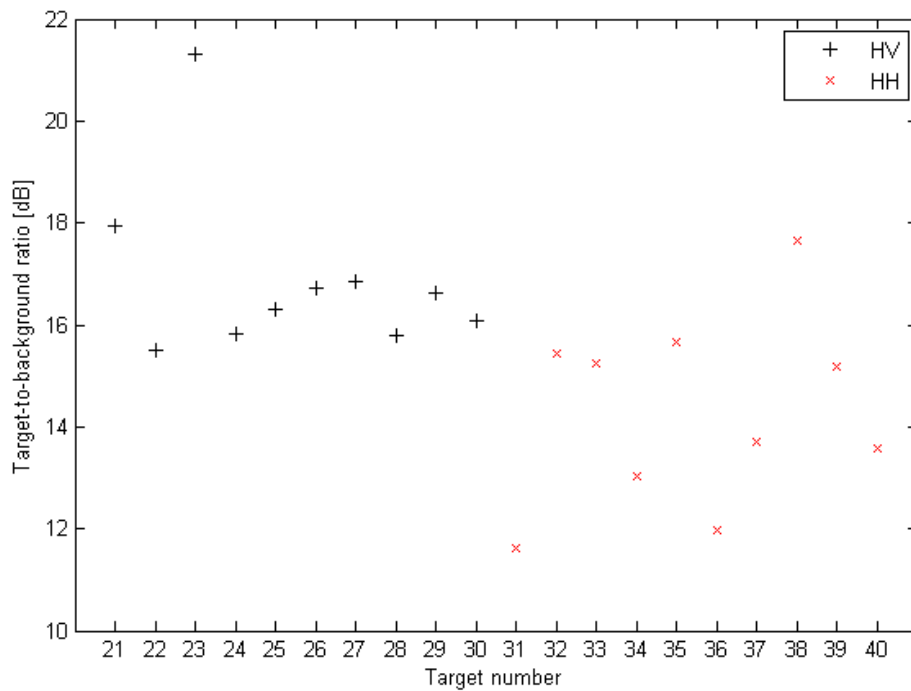
When looking at the results from data set 3, it is important to keep in mind that the measures of $|S_{HH}|$ and $|S_{HV}|$ are from different images, not from the same image as was the case for the first data sets. Direct comparison between polarizations are therefore not possible. However, we see that the cross-polarization targets have higher mean PBR and TBR than the ones in co-polarization. Also for this data set, TBR has considerably lower values than PBR, and vary less between the targets.

Table 6.12: PBR and TBR in dB for target 21 - 40.

Image	Target	Iceberg	Polarization	PBR	TBR
I8	21	A	$ S_{HV} $	63,03	17,94
I8	22	B	$ S_{HV} $	57,19	15,49
I8	23	C	$ S_{HV} $	71,25	21,31
I8	24	D	$ S_{HV} $	63,57	15,82
I10	25		$ S_{HV} $	55,71	16,29
I10	26		$ S_{HV} $	57,32	16,73
I10	27		$ S_{HV} $	56,71	16,84
I10	28		$ S_{HV} $	53,48	15,78
I10	29		$ S_{HV} $	61,58	16,61
I10	30		$ S_{HV} $	55,19	16,08
Mean			$ S_{HV} $	59,50	16,89
I7	31	D	$ S_{HH} $	44,80	11,62
I7	32	C	$ S_{HH} $	48,58	15,43
I7	33	A	$ S_{HH} $	48,96	15,26
I7	34	B	$ S_{HH} $	49,75	14,21
I9	35		$ S_{HH} $	50,79	15,65
I9	36		$ S_{HH} $	40,00	11,97
I9	37		$ S_{HH} $	46,48	13,69
I9	38		$ S_{HH} $	54,80	17,65
I9	39		$ S_{HH} $	53,40	15,19
I9	40		$ S_{HH} $	51,54	13,57
Mean			$ S_{HH} $	48,91	14,42



(a) PBR as function of target number.



(b) TBR as function of target number.

Figure 6.22: Contrast measures as function of target number.

Figure 6.22 shows the PBR and TBR of the iceberg targets as function of target number. In figure 6.22(a), we can see that nearly all icebergs selected from the cross-polarized images have larger PBR than the icebergs selected from the co-polarization images. Figure 6.22(b) shows that for TBR, most cross-polarized icebergs have better contrast than the co-polarized ones, but the separation between co- and cross-polarization is not as clear as for PBR.

From this we can conclude that

icebergs seem to have higher PBR in cross-polarization than in co-polarization. This is also true for TBR, but the separation is less here. More accurate results could be obtained with dual-or quad-polarization data, where co- and cross-polarization of the same target could be directly compared.

In section 3.5, discrimination between ships and icebergs were discussed. Howell *et al.* (2004) found that while ships have comparable responses in HV and HH, icebergs had less or no response in HV compared to HH [14]. The results of Howell *et al.* (2004) does not correspond to what have been seen in this experiment, where $|S_{HV}|$ gives better contrasts than $|S_{HH}|$. One possible reason for this is that the size of the icebergs used in our project may be larger than the ones used by Howell *et al.* (2004).

Contrast measures and relation to incidence angle

The incidence angles for the targets in data set 3 are given in table 6.13. PBR

Table 6.13: Incidence angles for target 21 - 40.

Image	Target	Polarization	θ [deg]
I8	21	$ S_{HV} $	31,03
I8	22	$ S_{HV} $	31,20
I8	23	$ S_{HV} $	31,24
I8	24	$ S_{HV} $	31,28
I10	25	$ S_{HV} $	36,74
I10	26	$ S_{HV} $	37,12
I10	27	$ S_{HV} $	36,46
I10	28	$ S_{HV} $	36,56
I10	29	$ S_{HV} $	37,77
I10	30	$ S_{HV} $	38,99
I7	31	$ S_{HH} $	38,49
I7	32	$ S_{HH} $	38,51
I7	33	$ S_{HH} $	38,43
I7	34	$ S_{HH} $	38,57
I9	35	$ S_{HH} $	41,90
I9	36	$ S_{HH} $	41,81
I9	37	$ S_{HH} $	39,99
I9	38	$ S_{HH} $	38,19
I9	39	$ S_{HH} $	37,57
I9	40	$ S_{HH} $	37,66

and TBR as function of incidence angle for targets in the images with $|S_{HH}|$ and $|S_{HV}|$ polarization are plotted in figure 6.23 and 6.24 respectively.

From figure 6.23 we see that PBR actually seem to decrease with incidence angle for the selected targets in $|S_{HH}|$ polarization. This is the opposite of what we saw for co-polarization for the man-made targets in data set 1 and 2, i.e. both in ocean and sea ice background, which seemed to increase with incidence angle. In figure 6.23(b), we don't see any trend in the data with respect to incidence angle for TBR.

Figure 6.24 shows plots of PBR and TBR versus incidence angle for the targets in $|S_{HV}|$ polarization. The plots show no clear trend as to how PBR and TBR change with incidence angle for these targets.

From figure 6.23 and 6.24, we can state that

there seem to be no relationship between incidence angle and iceberg TBR and PBR for $|S_{HV}|$, and for TBR in $|S_{HH}|$. However, a slightly decreasing trend was seen in PBR for $|S_{HH}|$. More accurate comparisons could possibly be made with dual- or quad-polarimetric data, in which the same icebergs could be directly compared at different polarizations. A larger iceberg database might show some incidence angle dependency that our data set is too small to reveal.

Comparison of repeated target acquisitions

Two of the images in data set 3 were acquired over the same region, each containing four clearly distinguishable icebergs, three large and one smaller. Even though we have no ground truth information, we can recognize the four icebergs in each image to be the same based on their shape and their relative position in the image. These icebergs have been labelled A-D, and the contrast measures from the two image acquisitions are compared in figure 6.25. It should be noted that several factors such as iceberg orientation relative to the radar, weather conditions etc. may be different in the two images, so they can not be compared directly, as we can in multi-polarization data. When we look at table 6.13, we see that the incidence angles of image I8 with $|S_{HV}|$ polarization are $\sim 31^\circ$, while the incidence angles of image I7 with $|S_{HH}|$ polarization are $\sim 38^\circ$, so this is one factor we should keep in mind. In addition, the images are acquired three days apart, so the icebergs or the background may have changed.

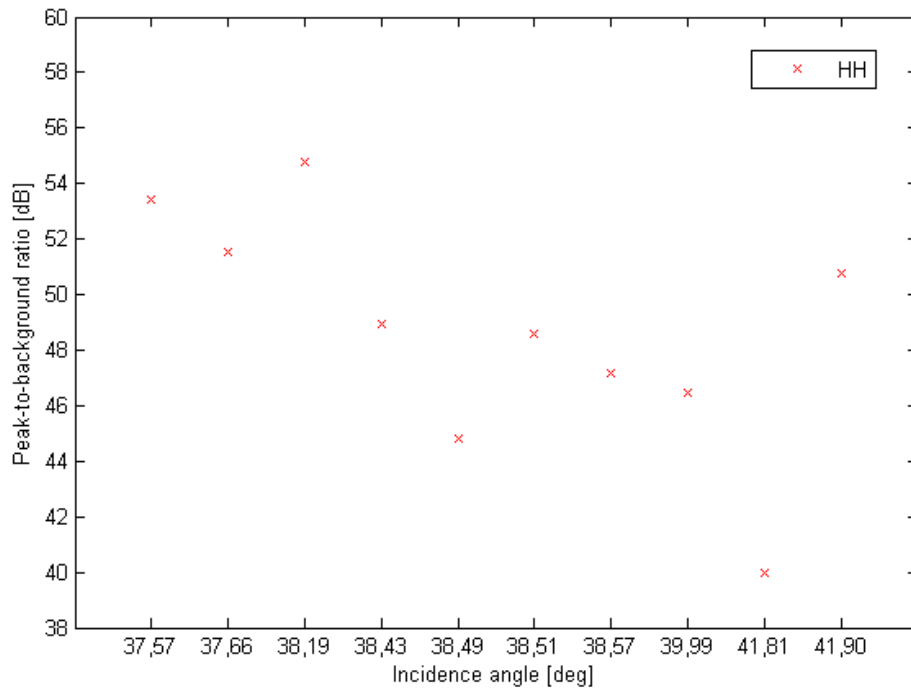
From figure 6.25 it is easily seen that for all four icebergs, both PBR and TBR are higher for $|S_{HV}|$ than for $|S_{HH}|$, with a larger difference in PBR, so

the repeated acquisitions of the four targets show that $|S_{HV}|$ at $\sim 31^\circ$ produces stronger iceberg contrasts than $|S_{HH}|$ at $\sim 38^\circ$, especially for PBR.

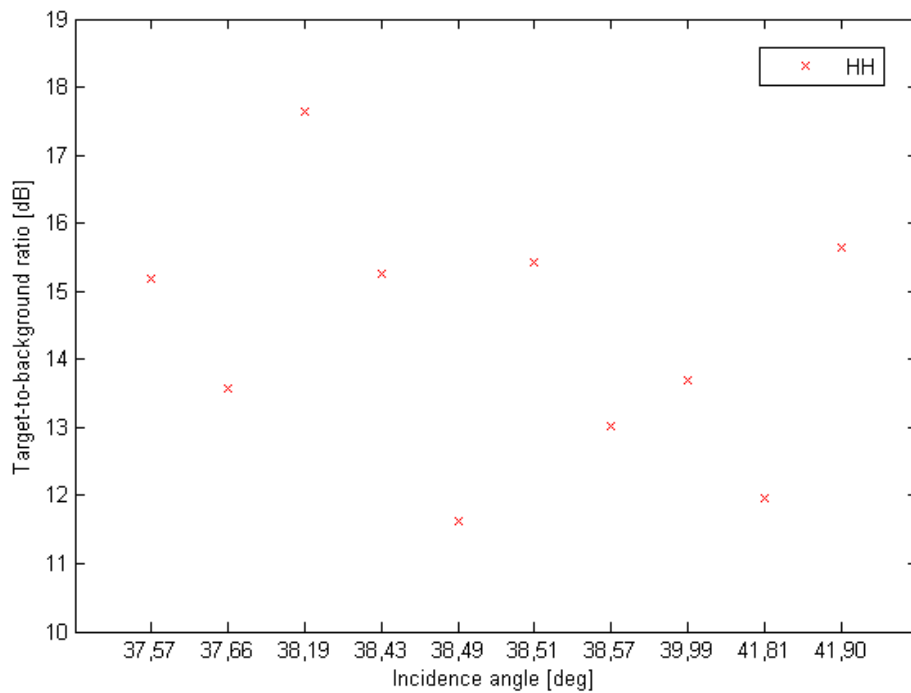
It should be noted that the segmentation parameters for each target, α and β , were not the same for the two polarizations, as they were for the first two data sets (see table A.1 in appendix). The parameters were chosen to give a best possible segmentation of each target, and this may influence the relative contrast.

The two acquisitions of iceberg A-D are compared in figure 6.26. The images are scaled to be in the range [0 255], and are not ground range corrected.

From figure 6.26 we see that the orientation of the icebergs are different for the two acquisitions. We also see that the icebergs have a slightly different shape

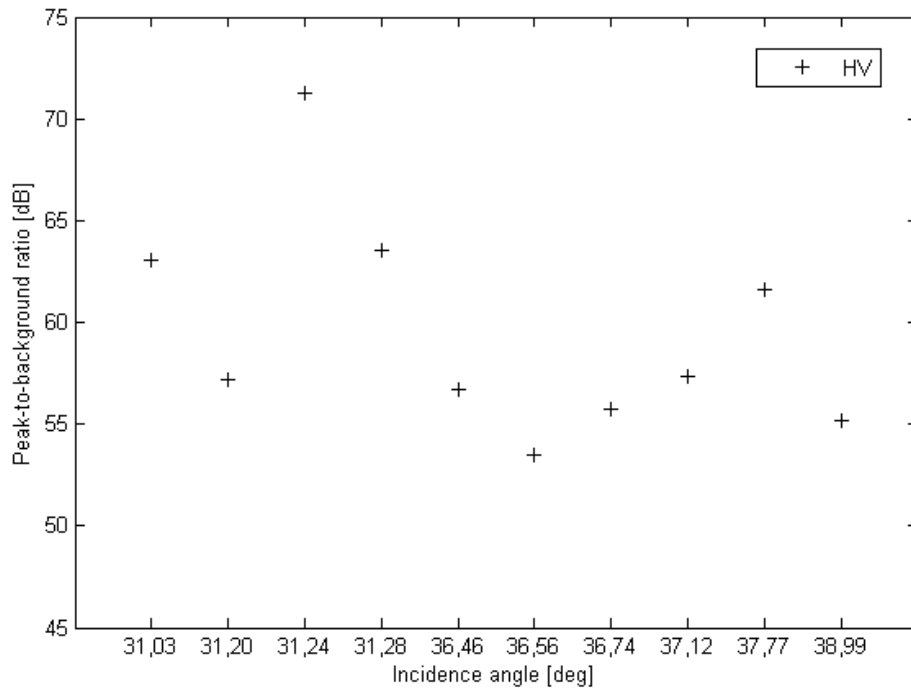


(a) PBR of icebergs in $|S_{HH}|$ polarization.

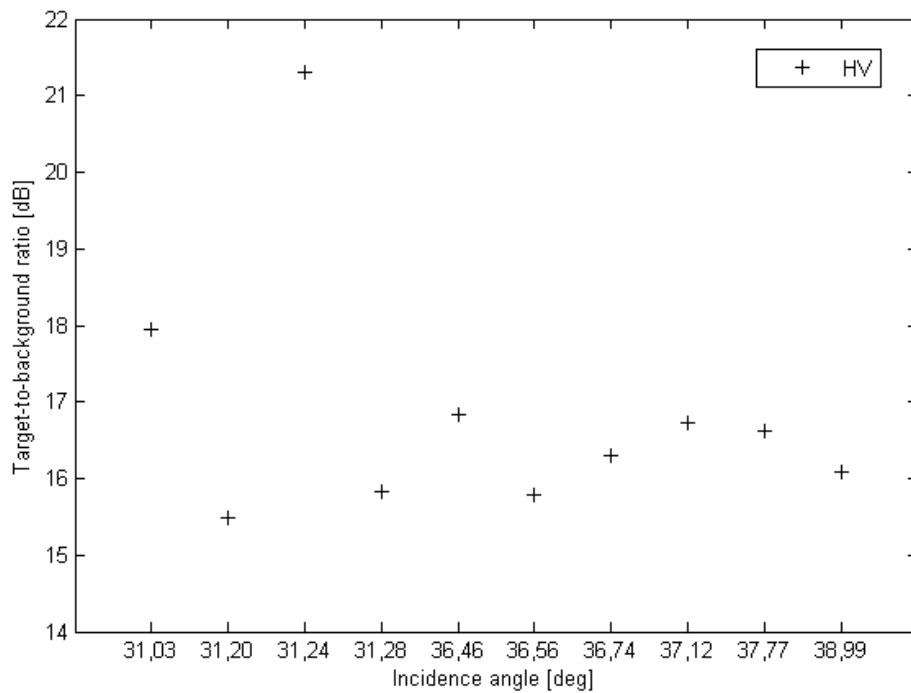


(b) TBR of icebergs in $|S_{HH}|$ polarization.

Figure 6.23: Contrast measures for $|S_{HH}|$ polarization as function of incidence angle.



(a) PBR of icebergs in $|S_{HV}|$ polarization.



(b) TBR of icebergs in $|S_{HV}|$ polarization.

Figure 6.24: Contrast measures for $|S_{HV}|$ polarization as function of incidence angle.

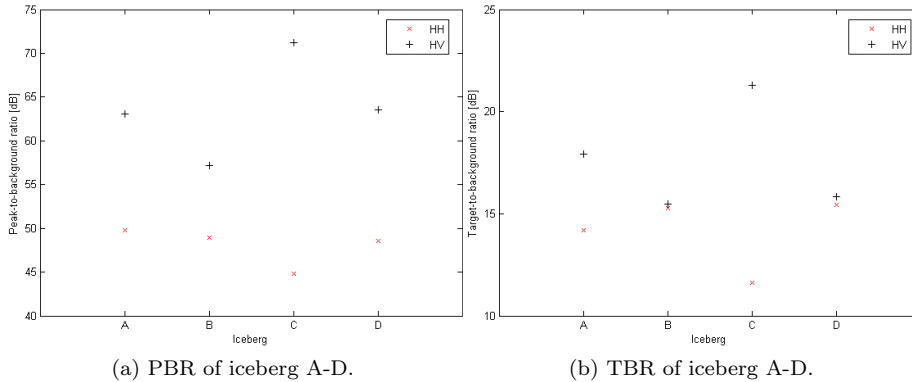


Figure 6.25: Contrast measures for iceberg A-D in two different images with different polarizations.

in the two images. This is possibly due to different orientations relative to the radar, and a compression in range direction. We also notice that different features in the background, such as structures in the ice, and boundaries between different ice types or between ice and ocean, are more prominent in the co-polarization images than in cross-polarization. In several of the subfigures, e.g. 6.26(a), we can see the small high-backscatter objects surrounding the iceberg, that made the segmentation process difficult. A darker area, possibly a shadow, is seen on the far-range side of some of the targets.

Contrast measures and relation to target size

As described earlier, six of the targets in data set 3 are larger than the other targets, and different subimage sizes and segmentation parameters are used for these. A quick comparison of contrast and size can be done by looking at these six compared to the rest of the targets, as is done in figure 6.27.

In figure 6.27 we see that in cross-polarization, all three large icebergs have higher PBR values than the smaller ones, while two of the three have higher TBR values. In co-polarization on the other hand, the larger icebergs do not differ from the smaller ones. As we also have seen in data set 1 and 2,

the contrast seem to increase for larger targets in cross-polarization, especially for PBR, and less so for TBR. For this data set, the co-polarization contrast seem to be unaffected by target size.

Contrast measures and relation to weather conditions

Weather data from the areas of interest at the dates of image acquisitions are summarized in table 5.12. We see that the co-polarization images, image I7 (target 31 - 34) and I9 (target 35 - 40), have wind strengths of ~ 3 m/s and 12 - 40 m/s respectively. From figure 5.11(b) we see that the distance from scene site of I9 to weather station 6 and to weather stations 3 and 4 are approximately the same, so it is difficult to know which measurement (12 m/s, 22 m/s or 40 m/s respectively) is most likely to be correct. As seen in figure 6.22, the PBR and

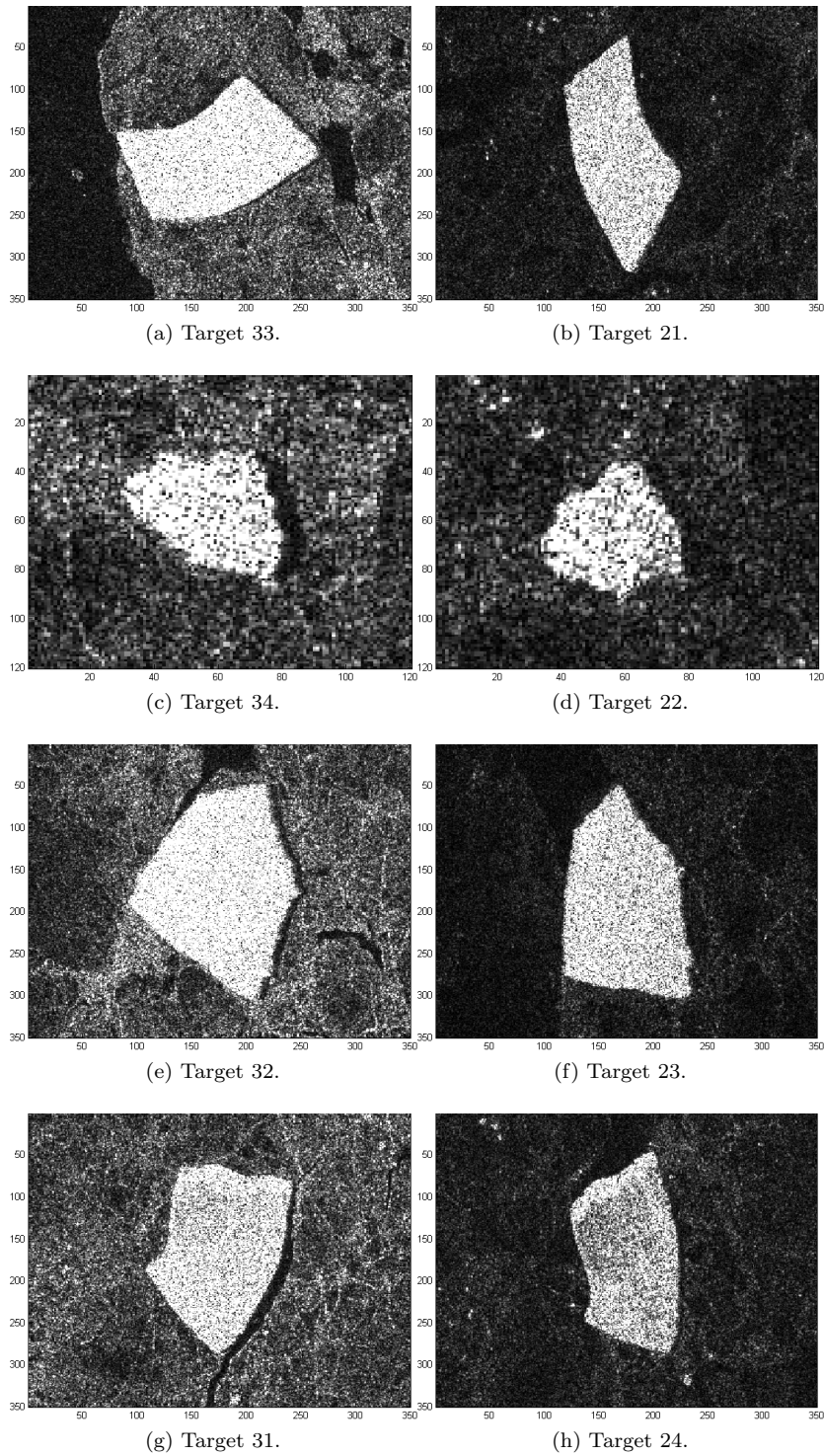


Figure 6.26: Repeated acquisitions of icebergs. Iceberg A in (a)-(b), iceberg B in (c)-(d), iceberg C in (e)-(f) and iceberg D in (g)-(h). $|S_{HH}|$ to the left, $|S_{HV}|$ to the right. RADARSAT-2 Data and Products ©MacDONALD, DETTWILER AND ASSOCIATES LTD. (2010) - All Rights Reserved

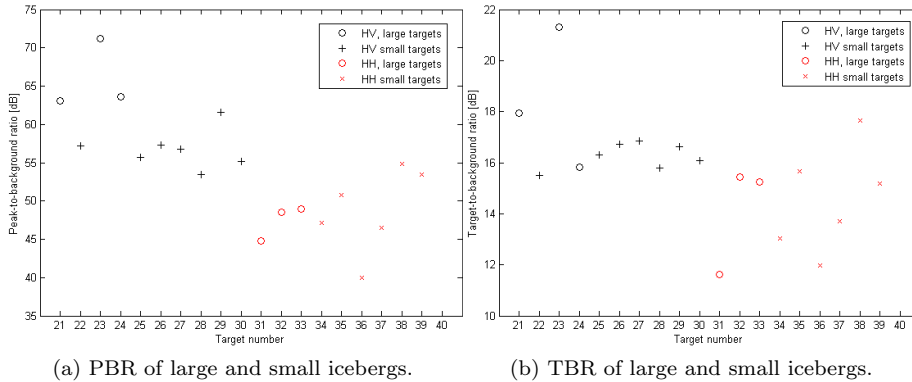


Figure 6.27: Comparison of contrast measures of large and small icebergs.

TBR for the targets in the two co-polarization images are quite well mixed, and it is difficult to see a difference between the targets from the two images that could be related to wind conditions.

The cross-polarization images, image I8 (target 21 - 24) and I10 (target 25 - 30), have wind speeds of 3 - 5 m/s and 5 - 40 m/s respectively. From figure 5.11(b) we see that weather station 7, and hence the measurement of 5 m/s, is closest to the scene site of I10. That means the difference in wind speed between the two cross-polarization images are not so large. Three of the targets in I8 have the highest PBR contrasts of the $|S_{HV}|$ targets, but as pointed out before, this may have to do with the target size. Target 22 do not have larger contrast than many of the targets in image I10, and hence it is more likely that 21, 23 and 24 have high PBR compared to the rest of the targets because of the size and not due to the wind conditions. The same holds for TBR. Based on this data, it can be stated that

the iceberg PBR and TBR does not seem to be affected by changes in wind speed.

6.2.4 Comparison of the data sets

The backscatter properties of oceans, ships, sea ice and icebergs are described in chapter 3. Data set 1 - 3 contain different types of targets in different backgrounds, and the mean values of PBR and TBR based on the data sets are compared in table 6.14. The ratio $|S_{HV}|/|S_{HH}|$ is included in the table, as the ratio between these two channels previously have been found to be a good way to discriminate between ships and icebergs.

If we first compare the contrast of man-made targets in ocean background versus ships in sea ice background (data set 1 and 2), we see that mean PBR is higher for sea ice background than for ocean background, in both channels, $|S_{VV}|$ and $|S_{VH}|$. This is not what we would expect, as ocean areas tend to produce less backscattering compared to sea ice, and hence have a darker appearance in SAR images. Based on this, we would expect the contrast between target and background to be higher in oceans than in sea ice. The TBR mean values

Table 6.14: Comparison of mean values of PBR and TBR in dB for the different data sets. Data set 1, 2 and 3 contain man-made targets in ocean areas, ships in sea ice, and icebergs in unknown background respectively.

	$ S_{VV} $	$ S_{VH} $	$ S_{HH} $	$ S_{HV} $	$ S_{HV} / S_{HH} $
PBR, data set 1	22,37	35,74	25,39	35,66	1,40
PBR, data set 2	47,25	61,93			
PBR, data set 3			48,91	59,50	1,22
TBR, data set 1	20,37	27,68	22,59	27,67	1,22
TBR, data set 2	17,83	19,77			
TBR, data set 3			14,42	16,89	1,17

correspond to this, with larger TBR mean values in data set 1, for both $|S_{VV}|$ and $|S_{VH}|$. As noted before, TBR is a more accurate measure for the backscatter strength as it takes an average of all target pixels, while the peak-value does not say anything about the rest of the target values. In data set 2, we only have four targets. The comparison would be more accurate with more data to compare, and we might get a different result.

If we compare the contrast of man-made targets versus icebergs, i.e. data set 1 and 3, we see that PBR for both $|S_{HV}|$ and $|S_{HH}|$ are higher for iceberg targets than for man-made targets. The opposite is true for TBR, where targets in data set 1 produce better contrasts than the icebergs.

In Howell *et al.* (2004), the area ratio between HH and HV polarization was found to be a good discriminator between icebergs and ships. Even though we look at contrast measures and not area, the contrast have been seen to depend on target size, and the ratio between these two channels are therefore included in this comparison. In table 6.14, we see that the ratio between mean $|S_{HV}|$ and $|S_{HH}|$ is higher for man-made targets than for icebergs both for PBR and TBR.

It should be noted that many of the iceberg targets are larger than the man-made targets. For all data sets, we have seen that size seem to influence the contrast measures, especially for PBR and cross-polarization. This can give rise to the higher mean value of iceberg targets in PBR compared to the man-made targets.

As we know that it is often assumed that $S_{HV} = S_{VH}$, we can also compare ship in ice data (data set 2) with iceberg in ice/ocean (data set 3). If we do that, we see that ships have stronger contrasts than icebergs both for PBR and TBR.

Although more reliable conclusions could be drawn from more comprehensive data sets, these preliminary results show that

the PBR of man-made targets in sea ice is larger than that in ocean background. The opposite is true for TBR. PBR of icebergs are larger than that of man-made targets in ocean in $|S_{HH}|$ and $|S_{HV}|$, while TBR is larger for man-made targets. The fact that the iceberg targets are larger in size than the man-made targets can influence these results. The $|S_{HV}|/|S_{HH}|$ ratio is larger for man-made targets than for icebergs in both PBR and TBR. Comparing ships located in sea ice in $|S_{VH}|$ to iceberg in $|S_{HV}|$ reveals that ships have the largest PBR and TBR.

6.3 Geometric characteristics

So far, contrast measures, i.e. the differences in backscatter strength between target and background, have been discussed. We have seen that many factors affect the PBR and TBR, and the discrimination between different target types may be difficult.

As can be seen in table 5.5, most of the targets in data set 1 are ships, but there are also some oil rigs. Deepsea Bergen, West Alpha and Aker Spitsbergen are rigs (i.e. target 3, 8, 13, 16 and parts of 4 and 9). When looking at table 6.3 and 6.4, and image 6.1 and 6.2, it is clear that the rigs have similar contrast values to the ships. When no ground truth data is available, it will be difficult to discriminate rigs from ships based only on contrast measures. In table 6.14, it is seen that there's a difference between iceberg and man-made target contrasts, especially for PBR where the icebergs have much higher values than man-made targets. However, this difference is likely to decrease when looking at icebergs with sizes comparable to ship sizes. Other features, e.g. for characterizing the shape of an object may then be more helpful for target discrimination.

Hu's 1st moment is defined in section 4.7.3, and is a measure of the elongatedness of an object. Hu's 1st moment is in this project calculated for a subset of the targets, based on ground range corrected images. Results are given in table 6.15.

Table 6.15: Hu's 1st moment for ground-range corrected targets.

Image	Target	Polarization	Target type	Hu's 1st moment
I1	1	$ S_{HV} $	Ship	0,1866
I1	2	$ S_{HV} $	Ship	0,5794
I1	3	$ S_{HV} $	Rig	0,3203
I8	21	$ S_{HV} $	Iceberg	0,2365
I8	22	$ S_{HV} $	Iceberg	0,2468
I8	23	$ S_{HV} $	Iceberg	0,1968
I8	24	$ S_{HV} $	Iceberg	0,2379
I7	31	$ S_{HH} $	Iceberg	0,2930
I7	32	$ S_{HH} $	Iceberg	0,2122
I7	33	$ S_{HH} $	Iceberg	0,2325
I7	34	$ S_{HH} $	Iceberg	0,2613

From table 6.15, we see that the rig (target 3) have higher value than target 1, but lower than target 2. From image 5.3 and table 5.5, we know that target 1 is much smaller than target 2, and this may be the reason for the unexpected low value of Hu's 1st moment for this ship.

Icebergs can have many different shapes, as seen in figure 6.21, and the elongatedness may vary a lot. From table 6.15, it is seen that all the icebergs have values between 0,1968 and 0,2930, which is lower than the moments of the largest ship and the rig. Based on this, we could conclude that

the Hu's 1st moment of the eight icebergs were smaller than the value of the largest ship and the rig, but larger than for the smallest ship. For the smaller ship, the elongated shape is more difficult to segment out due to the inherent

characteristics of SAR images. Hence, the application of Hu's 1st moment may in this context be dependent on ship size. Still, Hu's 1st moment may be useful for discrimination between large ships and smaller ships, or large ships versus other target types.

We should keep in mind that the eight icebergs are really four icebergs imaged twice. As Hu's moments are invariant to scale, translation and rotation, we would expect the two values of each target to be similar. The repeated calculation of Hu's 1st moment for the same icebergs are compared in table 6.16.

Table 6.16: Comparison of Hu's 1st moment of the iceberg targets in different image acquisitions and polarizations.

Iceberg	$ S_{HV} $	$ S_{HH} $
A	0,2365	0,2325
B	0,2468	0,2613
C	0,1968	0,2122
D	0,2379	0,2930

As we can see from table 6.16, the Hu's 1st moment for the same target in different images have quite similar values. For targets B, C and D, the value in $|S_{HH}|$ are slightly higher than the value in $|S_{HV}|$. Hu's 1st moment could be a useful feature in iceberg tracking.

Hu's 1st moment for iceberg A-D in two acquisitions have quite similar values, but have slightly higher values in the co-polarization image for three of the targets.

A comparison between two images of the same polarization would give a better indication as to how large differences one could see between repeated acquisitions of the same targets.

Chapter 7

Conclusions

In this thesis we have studied the characteristics of marine targets in satellite SAR images. The appearance of ships, oil rigs and icebergs have been evaluated with respect to scattering mechanisms, polarimetric information and geometry. PBR and TBR were calculated for different polarization channels and Pauli decomposition components, and possible relations between contrast measures and incidence angle, target size and weather conditions have been investigated. Hu's 1st invariant moment was used as a geometric measure for a subset of the targets.

Three data sets, containing different marine targets in ocean or sea ice background, have been investigated. Data set 1 is the largest data set, with quad-polarimetric images, containing 16 targets, well validated through AIS information. The most comprehensive study is therefore based on this. Data set 2 and 3 contain less data, and hence produce less reliable results.

Scattering Mechanisms

For data set 1, the polarimetric information have been investigated through the Pauli decomposition. The volume scattering component, $|S_{HV} + S_{VH}|$ was found to give the highest mean value of all polarization channels and decomposition components for both PBR and TBR. The double bounce component, $|S_{HH} - S_{VV}|$, was also seen to produce very high contrast values. One reason why the volume scattering component produces the best contrast may be the low ocean backscatter in cross-polarization, enhancing the contrast. Man-made targets are known to give strong double bounce scattering due to numerous corners and edges, so the high response in $|S_{HH} - S_{VV}|$ is expected. These results show that through quad-polarimetric data and polarimetric decompositions, improvements in target contrasts can be obtained.

Contrast measures and polarization

For all three data sets, it was shown that cross-polarization channels produce better contrasts than co-polarization channels, both for man-made targets and for icebergs. The difference between co- and cross-polarization is less for TBR than for PBR. In data set 1, better results were obtained in $|S_{HH}|$ compared to $|S_{VV}|$, and PBR and TBR in $|S_{HV}|$ and $|S_{VH}|$ were found to produce very

similar values, as expected from the reciprocity theorem. These findings are consistent with the results of other studies.

Contrast measures and incidence angle

For man-made targets in oceans (data set 1), it was seen that PBR and TBR increase from incidence angles $\sim 26^\circ$ to $\sim 45^\circ$ in $|S_{HH}|$, $|S_{VV}|$ and $|S_{HH} + S_{VV}|$. This is probably due to the reduction in co-polarization ocean clutter at higher incidence angles. In $|S_{HV}|$, $|S_{VH}|$ and $|S_{HV} + S_{VH}|$, a decrease with incidence angle was seen in PBR and no clear trend found in TBR. This is supported by investigation of repeated acquisitions of the same targets located at different incidence angles.

Cross-polarization contrasts are less superior to co-polarization contrasts at the highest incidence angle, but no break point where co-polarized contrast exceeded the cross-polarized was seen.

For ships in sea ice (data set 2), an indication of increasing PBR with incidence angle is seen for cross-polarization ($|S_{VH}|$).

Contrast measures and target size

All three data sets indicated a target size dependency in the contrast, particularly for cross-polarization (including $|S_{HV} + S_{VH}|$) and PBR, producing stronger contrasts for larger targets. However, man-made targets with significant differences in size were seen to produce similar contrast values.

Contrast measures and weather conditions

An indication of degraded contrast as the wind increases was seen for the targets in ocean background. This is expected as strong winds will roughen the surface and increase the ocean clutter levels. Data set 2 and 3 indicated that the wind strength does not significantly affect the contrast measures in sea ice areas.

Comparison of contrast measures from the different data sets

When comparing man-made targets in sea ice background versus ocean background in $|S_{VV}|$ and $|S_{VH}|$, mean PBR was found to show the largest response in sea ice, while TBR was strongest in ocean areas. Comparison of iceberg targets versus man-made targets in $|S_{HH}|$ and $|S_{HV}|$ indicated that best results are obtained for icebergs in PBR and for man-made objects in TBR. However, the $|S_{HV}|/|S_{HH}|$ ratio was larger for man-made targets than for icebergs in both PBR and TBR. Comparison of contrasts for ships in ice with respect to $|S_{VH}|$, versus icebergs with respect to $|S_{HV}|$, revealed that ships have the largest PBR and TBR.

Geometric measures

Hu's 1st geometric moment is an elongatedness measure, and a possible feature for target discrimination. This feature was evaluated for only a few targets, i.e. two ships, one oil rig and eight icebergs. The small and large ships had values of $\sim 0,19$ and $\sim 0,58$ respectively. The smaller ship is seen to appear more as a point target compared to the larger ship in the SAR image, and the elongated

shape is not maintained in the segmentation, hence the unexpected low value of elongatedness. The icebergs had values in the range from $\sim 0,19$ to $\sim 0,29$ and Hu's 1st moment of the oil rig was $\sim 0,32$, indicating that these targets have less elongated shapes than the largest ship. Hu's 1st moment may hence be a useful feature for discriminating between e.g. large and small ships, or large ships and other marine targets. However, iceberg shape and elongatedness is likely to show a high degree of variation.

7.1 Future work

Some suggestions for further work are proposed here:

- One problem for doing an accurate comparison of the measures between different target types are the lack of data. Quad-polarimetric data containing icebergs would make it possible to investigate the scattering properties of these targets and compare the dominating mechanisms to those found for ship targets in this project. Images containing both ships and icebergs could be basis for a direct comparison of different features, excluding effects from e.g. imaging geometry and weather conditions. The usefulness of features such as Hu's 1st moment for discrimination could hence be better evaluated.
- The investigation of scattering mechanisms could be extended by looking at the Pauli decomposition components for each target pixel, identifying the dominating scattering mechanisms of different parts of the target. The variations in ocean clutter would be excluded, and a more accurate description of a targets scattering mechanisms could be obtained.
- A larger database of ground range projected targets and their corresponding Hu's 1st moment would be interesting in order to get better statistics on the elongatedness measures for different target types. The possibility of using this feature for target classification, identification and/or tracking could then be addressed more properly.
- Several features for target characterization which are not applied in this project are described in chapter 4. Implementation of these in order to evaluate their usefulness in characterization of marine targets could be interesting.
- A better algorithm for detection and segmentation of targets, with less manual interference could be implemented.
- Acquisition of the same target with the same orientation at different incidence angles could be used to make a more accurate examination of the dependency of target contrast on incidence angle.

Appendices

Appendix A

Segmentation parameters

The values of α and β used in the segmentation are seen in table A.1.

Table A.1: Values of α and β for all targets.

Target	α	β
1	9	5
2	12	6
3	15	6
4	15	3
5	15	5
6	9	4
7	9	3
8	10	4
9	9	4
10	13	4
11	17	4
12	15	4
13	18	5
14	9	4
15	8	3
16	20	5
17	8	3
18	7	2
19	9	3
20	6	2
21	4	17
22	3	4
23	5	18
24	3	14
25	2	5
26	3	4
27	2	6
28	3	5
29	3	5
30	3	5
31	2	11
32	3	15
33	2	17
34	3	4
35	3	3
36	3	2
37	2	6
38	4	6
39	2	6
40	2	4

Values for α and β for segmentation of ground range corrected targets are given in table A.2.

Table A.2: Values of α and β for segmentation of ground range corrected targets.

Target	α	β
1	9	5
2	19	6
3	15	7
21	3	14
22	2	7
23	5	12
24	3	17
31	3	10
32	3	15
33	2	17
34	3	5

Appendix B

Image details

Properties of image I1 - I10 are listed in table B.1 - B.10.

Table B.1: Properties of I1.

Date and time	30.04.2010, 17:12:33
Acquisition type	Fine Quad Polarization
Product type	SLC
Incident angle near range	4.44990311e+01 deg
Incident angle far range	4.57694054e+01 deg
Pass direction	Ascending
Antenna pointing	Right
Satellite height	8.019625625000000e+05 m
Slant range near edge	1.069483206300000e+06 m
Number of samples per line	4100
Number of lines	5199
Beam	FQ26
Sampled Pixel Spacing	4.73307896 m
Sampled Line Spacing	5.11282587 m
Line Time Ordering	Decreasing
Pixel Time Ordering	Increasing

Table B.2: Properties of I2.

Date and time	05.08.2010, 16:43:23
Acquisition type	Standard Quad Polarization
Product type	SLC
Incident angle near range	2.57955570e+01 deg
Incident angle far range	2.76038227e+01 deg
Pass direction	Ascending
Antenna pointing	Right
Satellite height	8.021146875000000e+05 m
Slant range near edge	8.795780692585935e+05 m
Number of samples per line	1525
Number of lines	6787
Beam	Q7
Sampled Pixel Spacing	7.98707199 m
Sampled Line Spacing	4.75463104 m
Line Time Ordering	Decreasing
Pixel Time Ordering	Increasing

Table B.3: Properties of I3.

Date and time	04.08.2010, 17:12:36
Acquisition type	Standard Quad Polarization
Product type	SLC
Incident angle near range	4.45035133e+01 deg
Incident angle far range	4.57649269e+01 deg
Pass direction	Ascending
Antenna pointing	Right
Satellite height	8.019492500000000e+05 m
Slant range near edge	1.069532809700000e+06 m
Number of samples per line	1629
Number of lines	7125
Beam	Q26
Sampled Pixel Spacing	1.18326979e+01 m
Sampled Line Spacing	5.11532402 m
Line Time Ordering	Decreasing
Pixel Time Ordering	Increasing

Table B.4: Properties of I4.

Date and time	16.05.2009, 05:16:04
Acquisition type	Fine
Product type	SLC
Incident angle near range	3.32595482e+01 deg
Incident angle far range	3.64500237e+01 deg
Pass direction	Descending
Antenna pointing	Right
Satellite height	8.037648125000000e+05 m
Slant range near edge	9.391626212326979e+05 m
Number of samples per line	6622
Number of lines	10496
Beam	F22
Sampled Pixel Spacing	4.73307896 m
Sampled Line Spacing	4.94963980 m
Line Time Ordering	Increasing
Pixel Time Ordering	Decreasing

Table B.5: Properties of I5.

Date and time	17.05.2009, 14:44:43
Acquisition type	Fine
Product type	SLC
Incident angle near range	3.47725143e+01 deg
Incident angle far range	3.78723412e+01 deg
Pass direction	Ascending
Antenna pointing	Right
Satellite height	8.038882500000000e+05 m
Slant range near edge	9.536174452548996e+05 m
Number of samples per line	6862
Number of lines	10340
Beam	F21
Sampled Pixel Spacing	4.73307896 m
Sampled Line Spacing	5.02275515 m
Line Time Ordering	Decreasing
Pixel Time Ordering	Increasing

Table B.6: Properties of I6.

Date and time	20.05.2009, 14:57:07
Acquisition type	Fine
Product type	SLC
Incident angle near range	3.77495346e+01 deg
Incident angle far range	4.06717072e+01 deg
Pass direction	Ascending
Antenna pointing	Right
Satellite height	8.037880625000000e+05 m
Slant range near edge	9.846001820097560e+05 m
Number of samples per line	7330
Number of lines	10063
Beam	F1
Sampled Pixel Spacing	4.73307896 m
Sampled Line Spacing	5.17993784 m
Line Time Ordering	Decreasing
Pixel Time Ordering	Increasing

Table B.7: Properties of I7.

Date and time	07.12.2010, 02:16:51
Acquisition type	Fine
Product type	SLC
Incident angle near range	3.70746040e+01 deg
Incident angle far range	3.99844971e+01 deg
Pass direction	Descending
Antenna pointing	Right
Satellite height	8.209695000000000e+05 m
Slant range near edge	9.975214883557321e+05 m
Number of samples per line	7210
Number of lines	9849
Beam	F1
Sampled Pixel Spacing	4.73307896 m
Sampled Line Spacing	5.34786606 m
Line Time Ordering	Decreasing
Pixel Time Ordering	Increasing

Table B.8: Properties of I8.

Date and time	10.12.2010, 00:50:05
Acquisition type	Fine
Product type	SLC
Incident angle near range	3.02690430e+01 deg
Incident angle far range	3.35643768e+01 deg
Pass direction	Ascending
Antenna pointing	Right
Satellite height	8.208092500000000e+05 m
Slant range near edge	9.326309718709957e+05 m
Number of samples per line	6106
Number of lines	10672
Beam	F23
Sampled Pixel Spacing	4.73307896 m
Sampled Line Spacing	4.98148489 m
Line Time Ordering	Decreasing
Pixel Time Ordering	Increasing

Table B.9: Properties of I9.

Date and time	08.12.2010, 11:57:37
Acquisition type	Standard
Product type	SLC
Incident angle near range	3.65553169e+01 deg
Incident angle far range	4.22707100e+01 deg
Pass direction	Ascending
Antenna pointing	Right
Satellite height	8.181978750000000e+05 m
Slant range near edge	9.885960678020860e+05 m
Number of samples per line	5878
Number of lines	19204
Beam	S5
Sampled Pixel Spacing	1.18326979e+01 m
Sampled Line Spacing	5.39484882 m
Line Time Ordering	Decreasing
Pixel Time Ordering	Increasing

Table B.10: Properties of I10.

Date and time	08.12.2010, 13:38:47
Acquisition type	Fine
Product type	SLC
Incident angle near range	3.63420525e+01 deg
Incident angle far range	3.93016815e+01 deg
Pass direction	Ascending
Antenna pointing	Right
Satellite height	8.177985625000000e+05 m
Slant range near edge	9.858497149311252e+05 m
Number of samples per line	7090
Number of lines	10074
Beam	F1
Sampled Pixel Spacing	4.73307896 m
Sampled Line Spacing	5.28455782 m
Line Time Ordering	Decreasing
Pixel Time Ordering	Increasing

Appendix C

Results of method from pilot study

The results of the pilot study [50] are shown in table C.1.

The PBR_{PS} calculated from data set 1, using the method from the pilot study, are given in table C.2.

Table C.1: Results from the pilot study [50].

Image	Ship	$ S_{HH} $	$ S_{VV} $	$ S_{HV} $	$ S_{VH} $	$ S_{HH}+S_{VV} $	$ S_{HH}-S_{VV} $	$ S_{HV}+S_{VH} $	$ S_{HV}-S_{VH} $
1	1	10.63	13.06	143.24	138.76	3.86	96.36	154.80	6.94
1	2	14.94	13.99	84.52	84.54	8.31	92.06	94.81	8.34
1	3	12.45	13.29	147.78	144.20	11.60	74.39	170.90	11.01
1	4	7.73	8.97	28.99	27.79	4.28	52.40	30.83	3.52
1	5	14.73	14.64	153.81	153.99	7.46	96.20	166.82	7.46
1	6	15.61	15.65	56.95	52.45	12.62	89.51	58.40	5.63
1	7	12.29	13.07	55.94	53.99	7.81	83.65	59.19	7.23
1	8	10.29	11.77	46.35	44.55	6.88	62.52	51.57	4.16
2	9	11.50	9.80	25.09	23.87	7.60	53.68	30.14	3.88
2	10	14.46	12.51	58.99	60.76	9.79	51.95	72.43	3.81
2	11	14.31	14.64	62.43	57.57	14.03	29.05	78.69	3.82
2	12	10.25	10.28	42.46	41.75	10.05	35.68	50.86	3.66
2	13	17.75	16.88	45.22	46.79	16.71	40.85	58.58	3.69
2	14	14.14	12.81	54.28	55.06	10.38	34.46	67.30	3.33
2	15	15.41	14.63	59.29	58.12	14.92	38.66	74.54	3.31
2	16	22.48	18.84	63.20	67.16	21.37	51.95	93.58	3.16
3	17	10.83	8.17	26.18	26.53	9.30	19.96	29.55	3.66
3	18	11.56	6.84	18.61	18.38	9.14	23.67	21.79	3.12
3	19	16.04	11.93	37.13	35.99	7.63	45.20	42.57	3.34
3	20	8.65	5.07	27.34	29.14	3.78	27.97	32.62	3.29
3	21	9.68	7.06	23.55	21.43	4.79	39.35	25.41	3.51
3	22	7.79	5.41	37.46	37.52	5.59	30.44	42.75	9.60
3	23	9.14	5.49	18.66	18.93	5.79	22.13	22.12	3.58
3	24	50.40	43.14	35.33	41.09	19.34	212.52	44.35	9.49
3	25	8.23	11.10	47.81	45.61	5.42	35.09	52.52	3.59
3	26	17.06	10.32	77.77	78.52	5.39	60.52	88.70	3.66
3	27	44.21	33.91	70.71	73.25	39.05	62.14	83.20	3.36
3	28	14.40	9.67	28.57	29.22	10.03	46.77	33.64	3.90
3	29	41.60	32.08	24.91	26.40	36.79	27.14	29.40	6.98
Mean		16.16	13.97	55.26	54.94	11.38	56.42	64.21	4.97

Table C.2: PBR_{PS} for data set 1, using the method from the pilot study.

Image	Target	$ S_{HH} $	$ S_{VV} $	$ S_{HV} $	$ S_{VH} $	$ S_{HH}+S_{VV} $	$ S_{HH}-S_{VV} $	$ S_{HV}+S_{VH} $	$ S_{HV}-S_{VH} $
1	1	24,55	17,93	32,85	34,11	21,16	44,15	41,83	3,58
1	2	23,85	16,65	56,56	60,62	20,87	46,60	71,02	5,48
1	3	24,03	17,39	56,80	56,03	22,00	47,71	67,95	3,72
1	4	20,14	15,37	55,37	54,55	18,75	44,39	63,39	10,70
1	5	24,13	16,82	37,25	37,57	15,66	50,09	43,36	3,44
2	6	11,36	10,24	136,87	130,70	9,90	61,81	147,60	4,74
2	7	11,32	10,35	121,59	125,57	10,84	49,49	135,88	5,46
2	8	10,02	9,35	107,66	108,11	9,12	62,98	119,25	5,70
2	9	9,58	8,74	117,49	114,34	8,19	61,14	128,49	3,23
2	10	10,82	7,13	48,96	48,99	7,06	33,88	53,82	3,37
3	11	32,95	20,24	83,83	89,43	26,36	53,63	106,33	3,69
3	12	33,79	21,63	87,87	84,70	27,70	56,80	109,10	3,56
3	13	31,57	20,91	93,02	96,54	26,50	68,40	116,06	6,46
3	14	26,49	16,05	39,64	40,15	17,87	30,33	48,51	3,53
3	15	34,68	11,38	40,17	41,11	9,37	58,87	50,30	2,96
3	16	32,52	20,30	95,68	95,11	26,08	69,19	118,27	4,41
Mean		22,61	15,03	75,73	76,10	17,34	52,47	88,82	4,63

Appendix D

Results based on amplitude images

The contrast measures based on the amplitude images for data set 2 and 3 are given in table D.1 and D.2.

Table D.1: PBR_A and TBR_A for data set 2.

Image	Target	Ratio	$ S_{VV} $	$ S_{VH} $
I4	17	PBR	11,95	27,25
I4	18	PBR	11,54	17,02
I5	19	PBR	11,06	29,09
I6	20	PBR	16,03	30,00
Mean		PBR	12,65	25,84
I4	17	TBR,A	8,76	10,85
I4	18	TBR,A	8,39	8,06
I5	19	TBR,A	8,81	11,69
I6	20	TBR,A	10,02	9,59
Mean		TBR	9,00	10,05

Table D.2: PBR_A and TBR_A for targets in data set 3.

Image	Target	Iceberg	Polarization	PBR	TBR
I8	21	A	$ S_{HV} $	27,11	8,42
I8	22	B	$ S_{HV} $	20,92	6,58
I8	23	C	$ S_{HV} $	40,31	12,09
I8	24	D	$ S_{HV} $	27,52	6,45
I10	25		$ S_{HV} $	18,52	6,70
I10	26		$ S_{HV} $	20,01	7,13
I10	27		$ S_{HV} $	19,33	7,05
I10	28		$ S_{HV} $	16,75	6,57
I10	29		$ S_{HV} $	24,50	6,93
I10	30		$ S_{HV} $	17,90	6,62
Mean			$ S_{HV} $	23,29	7,45
I7	31	D	$ S_{HH} $	11,28	4,31
I7	32	C	$ S_{HH} $	13,56	6,65
I7	33	A	$ S_{HH} $	15,71	7,35
I7	34	B	$ S_{HH} $	14,07	5,63
I9	35		$ S_{HH} $	14,50	6,41
I9	36		$ S_{HH} $	8,33	4,29
I9	37		$ S_{HH} $	12,11	5,36
I9	38		$ S_{HH} $	17,87	8,25
I9	39		$ S_{HH} $	16,68	6,05
I9	40		$ S_{HH} $	15,21	5,04
Mean			$ S_{HH} $	13,93	5,93

Bibliography

- [1] Arnesen, T. N., Olsen, R.B., "Literature review on vessel detection", FFI-report 2004/02619, 2004
- [2] Arnesen, T. N., Olsen, R.B., "Vurdering av ENVISAT ASAR for skipsdeteksjon", FFI-report 2004/02121, 2004
- [3] Askne, J., Dierking, W., "Sea Ice Monitoring in the Arctic and Baltic Sea Using SAR", in: "Remote Sensing of the European Seas" (ed. Barale, V., Gade, M.), Springer Science + Business Media B.V., 2008
- [4] Brekke, C., "Automatic screening of Synthetic Aperture Radar imagery for detection of oil pollution in the marine environment", FFI-report 2007/02391, 2007
- [5] Brekke, C., Anfinson, S. N., "Ship detection in Ice-Infested Waters Based on Dual-Polarization SAR Imagery", in: IEEE Geoscience and Remote Sensing Letters, Vol. 8, No. 3, May 2011
- [6] Carl-Cranz-Gesellschaft (CCG); "SAR Principles and Application" (CD), November 2007
- [7] Crisp, D.J., "The State-of-the-Art in Ship Detection in Synthetic Aperture Radar Imagery.", DSTO Information Sciences Laboratory, Australia, May 2004
- [8] Curlander, J.C., McDonough, R.N., "Synthetic Aperture Radar, Systems and Signal Processing", John Wiley & Sons, Inc., 1991
- [9] Directorate of Fisheries, website:
<http://www.fiskeridir.no/register/fartoyreg/?edbid=1989009927>
- [10] Elachi, C., Zyl, J.V., "Introduction to the physics and techniques of Remote Sensing", second edition, John Wiley & Sons, Inc., 2006
- [11] ESA PolSARpro Tutorial: "Part I-Tutorial on Radar Polarimetry", Ch. 4: "Polarimetric Decompositions",
<http://earth.esa.int/polsarpro/tutorial.html>
- [12] Flett, D., Abreu, R.D., Arkett, M., Gauthier, M., "Initial evaluation of RADARSAT-2 for operational sea ice monitoring", in: International Geoscience and Remote Sensing Symposium, 2008

- [13] Greidanus, H., "Satellite Imaging for Maritime Surveillance of the European Seas", in: "Remote Sensing of the European Seas" (ed. Barale, V., Gade, M.), Springer Science + Business Media B.V., 2008
- [14] Howell, C., Youden, J., Lane, K., Power, D., Randell, C., Flett, D., "Iceberg and Ship Discrimination with ENVISAT Multi-Polarization ASAR", in: International Geoscience and Remote Sensing Symposium, 2004.
- [15] Howell, C., Power, D., Lynch, M., Dodge, K., Bobby, P., Randell, C., Vachon, P., Staples, G., "Dual Polarization Detection of Ships and Icebergs - Recent results with ENVISAT ASAR and Data Simulations of RADARSAT-2", in: International Geoscience and Remote Sensing Symposium, 2008
- [16] Hu, M.-K., "Visual Pattern Recognition by Moment Invariants", IRE Transactions on Information Theory 8, p. 179 - 187, 1962
- [17] Huang, Z., Leng, J., "Analysis of Hu's Moment Invariants on Image Scaling and Rotation", in: 2nd International Conference on Computer Engineering and Technology, Volume 7, p. 476-480, 2010
- [18] Jensen, R.J., "Remote Sensing of the Environment, An Earth Resource Perspective", second edition, Pearson Prentice Hall, Pearson Education, Inc., 2007
- [19] Lane, K., Power, D., Chakraborty, I., Youden, J., Randell, C., "RADARSAT-1 Synthetic Aperture Radar Iceberg Detection Performance ADRO-2 A223", in: International Geoscience and Remote Sensing Symposium, Vol.4, 2002.
- [20] Lane, K., Power, D., Youden, J., Flett, D., "Validation of Synthetic Aperture Radar for Iceberg Detection in Sea Ice", in: International Geoscience and Remote Sensing Symposium, 2004.
- [21] Lecture FYS-3001, University of Tromsø, spring 2010
- [22] Lecture, FYS-3023, University of Tromsø, fall 2010
- [23] Liu, C., Vachon, P.W., Geling, G.W., "Improved ship detection with airborne polarimetric SAR data", in: Canadian Journal of Remote Sensing, Vol. 31, No. 1, 2005
- [24] MARISS (European Maritime Security Service): "Analysis of Options for MARISS Services Extension", 2009
- [25] Massom, R. A., "Principal Uses of Remote Sensing in Sea Ice Field Research", in: "Field Techniques for Sea Ice Research" (ed. Eicken, H., Gradinger, R., Salganek, M., Shirasawa, K., Perovich, D., Lepranta, M.), Ch. 3.15, University of Alaska press, 2009
- [26] Nansen Environmental and Remote Sensing Centre (NERSC) and Kongsberg Satellite Services (KSAT) report, "The utilisation of satellite images for the oil in ice experiment in the Barents Sea in May 2009", NERSC Technical Report no. 305, December, 2009
- [27] Natural Resources Canada, Tutorial: "Fundamentals of remote sensing"
<http://www.ccrs.nrcan.gc.ca/resource/tutor/fundam/index.e.php>

- [28] Nixon, M., Aguado, A., "Feature Extraction & Image Processing", Elsevier, 2002
- [29] Norwegian Armed Forces, website:
<http://www.mil.no/sjo/kv/start/fartoyene/article.jhtml?articleID=156016>
- [30] Norwegian Coastal Administration, website: www.kystverket.no
- [31] Norwegian Petroleum Directorate, website:
<http://www.npd.no/no/Kart/Fakta-i-Google-Earth/>
- [32] Norwegian Polar Institute, website: <http://lance.npolar.no/en/>
- [33] Norwegian Space Centre, website: www.romsenter.no
- [34] Offshore.no, website: <http://www.offshore.no>
- [35] Onsott, R., "Antarctic Sea Ice and Icebergs", in: "Synthetic Aperture Radar, Marine User's Manual" (ed. Jackson, C. R., Apel, J.R.), Ch. 19, U.S. Department of Commerce, September 2004
- [36] Onsott, R., Schuman, R.A., "SAR Measurements of Sea Ice", in: "Synthetic Aperture Radar, Marine User's Manual" (ed. Jackson, C. R., Apel, J.R.), Ch.3, U.S. Department of Commerce, September 2004
- [37] Panagopoulos, G., Christoulas, G., Anastassopoulos, V., "Ship Identification Using Signatures from Cross-Polarized SAR Images", proceedings for the 4th WSEAS International Conference on REMOTE SENSING, 2008
- [38] Power, D., Youden, J., Lane, K., Randell, C., Flett, D., "Iceberg Detection Capabilities of RADARSAT Synthetic Aperture Radar", in: Canadian Journal of Remote Sensing, Vol. 27, No. 5, October 2001
- [39] Premaratne, P., Safaei, F., "Ship classification by superstructure Moment Invariants", in: Proceedings of the 5th international conference on Emerging intelligent computing technology and applications, Springer-Verlag Berlin Heidelberg, p. 327-335, 2009
- [40] RADARSAT-2 Brochure, "A New Era in Synthetic Aperture Radar",
http://www.radarsat2.info/about/r2_brochure.pdf
- [41] RADARSAT-2 Product Information Definition, March 2008
- [42] RADARSAT-2, Product details,
http://www.radarsat2.info/product/RS-2_Product_Details.pdf
- [43] RADARSAT-2 Tutorial, "Polarimetric Parameters",
http://www.radarsat2.info/about/polar/polar_parameter.pdf
- [44] RADARSAT-2 website: www.radarsat2.info
- [45] RAdar Tool (RAT), website: <http://radartools.berlios.de/index.php>
- [46] Sandven, S. and Johannesen, O.M., "Sea Ice Monitoring by Remote Sensing", in: "Manual of Remote Sensing: Remote Sensing of the Marine Environment" (ed. James F.R. Gower), third edition, Ch. 8, American Society for Photogrammetry & Remote Sensing, Vol. 6, p. 241-283, 2006

- [47] Scatterometer Climate Record Pathfinder, website:
http://www.scp.byu.edu/current_icebergs.html
- [48] Ships and Oil.com, website:
<http://www.shipsandoil.com/ShipInformation/Sartor%20Shipping/Sartor%20Shipping.htm>
- [49] Silva, T.A.M., Bigg, G.R., "Computer-based identification and tracking of Antarctic icebergs in SAR images", in: Remote Sensing of Environment 94, p. 287-297, 2005
- [50] Skrunes, S., "Characteristics of ships in polarimetric SAR data", Project paper in energy an environment in the north, University of Tromsø, June 2010
- [51] Souyris, J.-C., Henry, C., Adragna, F., "On the Use of Complex SAR Image Spectral Analysis for Target Detection: Assessment of Polarimetry", in: IEEE Transactions on Geoscience and Remote Sensing, vol 41, no 12, December 2003
- [52] Touzi,R., "Calibrated polarimetric SAR data for ship detection", in: International Geoscience and Remote Sensing Symposium, 2000
- [53] Touzi,R., Charbonneau, F., Hawkins, R.K., Murnaghan, K., Kavoun, X., "Ship-Sea Contrast Optimization When Using Polarimetric SARs", in: International Geoscience and Remote Sensing Symposium, 2001
- [54] Touzi,R., Charbonneau, F., "The SSCM for ship characterization using polarimetric SAR", in: International Geoscience and Remote Sensing Symposium, 2003
- [55] Vachon, P.W., English, R. A., Wolfe, J., "Ship signatures in Synthetic Aperture Radar Imagery", in: International Geoscience and Remote Sensing Symposium, 2007
- [56] Vachon, P.W., Wolfe, J., "Validation of ship signatures in Envisat ASAR AP mode data using AISLive, Data acquisition, processing, and analysis results", Defence Research and Development Canada, Ottawa, March 2008
- [57] Wang, H., Huang,Q., Pi, Y., "Polarization Decomposition with S and T matrix of a PolSAR Image", in: International Conference on Communications, Circuits and Systems, 2009
- [58] Jeremy, M., Campbell, J.W.M., Mattar, K., Potter, T., "Ocean Surveillance with Polarimetric SAR", in: Canadian Journal of Remote Sensing, Vol.27, No.4, August 2001
- [59] Zhaoying, H., Jinsong, C., "A review of ship detection algorithms in polarimetric SAR images", in: International Conference on Signal Processing (ICSP) proceedings, 2004

List of Figures

2.1	Geometry of a radar, where A-E indicates flight direction, nadir, swath width, range direction and azimuth direction respectively (figure from [27]).	6
2.2	Geometry of a radar, where A-D indicates incident angle, look angle, slant range distance and ground range distance respectively (figure from [27]).	7
2.3	Echo pulses from target A is recorded by the moving antenna as long as the target is within the radar beam, and the synthesized antenna length is given by B (figure from [27]).	8
2.4	Horizontal (H) and vertical (V) polarization (figure from [27]).	9
2.5	Volume scattering (figure from [27]).	10
2.6	Surface scattering from a smooth surface (A) and a rough surface (B) (figure from [43]).	11
2.7	Double bounce scattering (figure from [27]).	12
3.1	Envisat ASAR, HH-polarization image of the Norne field in September 2003. To the right, some ships and oil rigs can be seen. Several meteorological and oceanographic phenomena are also visible (figure from [2]).	17
3.2	Radar backscatter from ocean areas as function of incidence angle, calculated with CMOD (C-band, VV) for various wind strengths. The radar looks straight into the wind (figure from [2]).	18
3.3	RADARSAT-2 image of ships in different polarizations (figure from [50]).	19
3.4	Summary of contrast measures as function of incidence angle and ship length for both co- and cross-polarization as found in Vachon and Wolfe (2008) (figure from [56]).	23
3.5	RADARSAT-1 (C-band, HH) image of a region near Cape Roberts. The image shows landfast ice, and leads along the coastline due to strong katabatic winds (figure from [35]).	25
3.6	Aircraft SAR image (C-band, VV) from Beaufort Sea during the winter, showing pack ice. The imaged area is approximately 10 km wide and incidence angles range from 20° to 70°. FY, MY and PR denotes First Year, Multi Year and Pressure Ridges respectively (figure from [36]).	26
3.7	SAR response of kilometer-sized icebergs (figure from [35]).	28

3.8	a) Maersk Chegnecto, a 70 m supply vessel. (b) HH data of a. (c) HV data of a. (d) Multi-polarization membership map of a. (e) Large Tabular Iceberg, 160×140 m length/width. (f) HH data of e. (g) HV data of e. (h) Multi-polarization membership map of e (figure from [14]).	30
4.1	Subimage of size 120×120 pixels, with the target in green in the center. The four 30×30 pixels corners in black are used as background measure.	35
4.2	Segmentation of target 1 in HV polarization; (a) original image, (b) image before and (c) after removal of pixels with less than 5 neighbours above the threshold T . RADARSAT-2 Data and Products ©MacDONALD, DETTWILER AND ASSOCIATES LTD. (2010) - All Rights Reserved	37
4.3	Compression of areas in near-range compared to far-range in slant range images (figure from [27]).	39
4.4	Examples of slant range and ground range images of icebergs. RADARSAT-2 Data and Products ©MacDONALD, DETTWILER AND ASSOCIATES LTD. (2010) - All Rights Reserved	40
4.5	Subimages as defined in the pilot study and in the current project.	41
5.1	RADARSAT-2 modes of operation (figure from [40]).	50
5.2	Geographical positions of image I1, I2 and I3 (figures from Google Earth).	52
5.3	Pauli image derived from image I1.	54
5.4	Pauli image derived from image I2.	55
5.5	Pauli image derived from image I3.	55
5.6	Photos of some of the targets present in I1, I2 and I3.	56
5.7	The observation sites for obtaining weather data, and position of image I1, I2 and I3 (figure from Google Earth).	57
5.8	Geographical positions of image I4, I5 and I6 (figure from Google Earth).	58
5.9	K/V Svalbard and R/V Lance and photos taken during the Oil in Ice Experiment (photos from [29], [32] and [26]).	59
5.10	The observation sites for obtaining weather data, and position of image I4, I5 and I6 (figure from Google Earth).	60
5.11	Geographical positions of images and weather stations in data set 3 (figures from Google Earth).	61
6.1	PBR as function of target number.	68
6.2	TBR as function of target number.	69
6.3	Target 6, Norne, in different polarization channels and Pauli decomposition components. RADARSAT-2 Data and Products ©MacDONALD, DETTWILER AND ASSOCIATES LTD. (2010) - All Rights Reserved	70
6.4	Target 10, Ocean prince, in different polarization channels and Pauli decomposition components. RADARSAT-2 Data and Products ©MacDONALD, DETTWILER AND ASSOCIATES LTD. (2010) - All Rights Reserved	71
6.5	PBR as function of incidence angle.	72

6.6	TBR as function of incidence angle.	73
6.7	PBR and TBR for VV and VH polarization at different incidence angles.	74
6.8	PBR and TBR for HH and HV polarization at different incidence angles.	75
6.9	Contrast measures for Ocean Prince in different images and at different incidence angles.	77
6.10	Contrast measures for Norne in different images and at different incidence angles.	79
6.11	Comparison of two acquisitions of Norne. RADARSAT-2 Data and Products ©MacDONALD, DETTWILER AND ASSOCIATES LTD. (2010) - All Rights Reserved	80
6.12	Contrast measures for Aker Spitsbergen in different images and at different incidence angles.	82
6.13	Contrast measures for Island Wellserver in different images and at different incidence angles.	83
6.14	Contrast measures as function of target length.	84
6.15	Contrast measures as function of target number.	87
6.16	Contrast measures as function of incidence angle.	88
6.17	Contrast measures for K/V Svalbard in different images and at different incidence angles.	89
6.18	Contrast measures for R/V Lance in different images and at different incidence angles.	90
6.19	Comparison of two acquisitions of K/V Svalbard. RADARSAT-2 Data and Products ©MacDONALD, DETTWILER AND ASSOCIATES LTD. (2009) - All Rights Reserved	91
6.20	Contrast measures as function of ship length, including mean value of repeated acquisitions.	92
6.21	Examples of iceberg targets. (a)-(d) are in $ S_{HV} $, (e)-(h) in $ S_{HH} $. RADARSAT-2 Data and Products ©MacDONALD, DETTWILER AND ASSOCIATES LTD. (2010) - All Rights Reserved	94
6.22	Contrast measures as function of target number.	96
6.23	Contrast measures for $ S_{HH} $ polarization as function of incidence angle.	99
6.24	Contrast measures for $ S_{HV} $ polarization as function of incidence angle.	100
6.25	Contrast measures for iceberg A-D in two different images with different polarizations.	101
6.26	Repeated acquisitions of icebergs. Iceberg A in (a)-(b), iceberg B in (c)-(d), iceberg C in (e)-(f) and iceberg D in (g)-(h). $ S_{HH} $ to the left, $ S_{HV} $ to the right. RADARSAT-2 Data and Products ©MacDONALD, DETTWILER AND ASSOCIATES LTD. (2010) - All Rights Reserved	102
6.27	Comparison of contrast measures of large and small icebergs. . .	103

List of Tables

4.1	Pauli matrices and corresponding scattering mechanisms [57][11].	33
4.2	Decomposition components and colour channels used for generating Pauli RGB images from quad-polarimetric data.	33
5.1	Properties of the different modes of RADARSAT-2 [40].	50
5.2	RADARSAT-2, Fine Quad-Pol, SLC details [42].	51
5.3	RADARSAT-2, Standard Quad-Pol, SLC details [42].	51
5.4	Number of targets and subimages in data set 1.	53
5.5	Properties of the targets in data set 1.	53
5.6	Weather data for data set 1.	56
5.7	RADARSAT-2, Fine mode, SLC details [42].	57
5.8	Properties of the targets in data set 2 [29][32].	58
5.9	Weather data of data set 2.	59
5.10	RADARSAT-2, Standard mode, SLC details [42].	60
5.11	Overview of the selected targets in data set 3.	62
5.12	Weather data for data set 3.	62
6.1	PBR_A for target 1 - 16.	65
6.2	TBR_A for target 1 - 16.	66
6.3	PBR in dB for target 1 - 16.	67
6.4	TBR in dB for target 1 - 16.	67
6.5	Incidence angles for target 1 - 16.	71
6.6	Contrast measures in dB for Ocean Prince in different images.	76
6.7	Contrast measures in dB for Norne in different images.	78
6.8	Contrast measures in dB for Aker Spitsbergen in different images.	78
6.9	Contrast measures in dB for Island Wellserver in different images.	80
6.10	PBR and TBR in dB for target 17 - 20.	86
6.11	Incidence angles for target 17 - 20.	89
6.12	PBR and TBR in dB for target 21 - 40.	95
6.13	Incidence angles for target 21 - 40.	97
6.14	Comparison of mean values of PBR and TBR in dB for the different data sets. Data set 1, 2 and 3 contain man-made targets in ocean areas, ships in sea ice, and icebergs in unknown background respectively.	104
6.15	Hu's 1st moment for ground-range corrected targets.	105
6.16	Comparison of Hu's 1st moment of the iceberg targets in different image acquisitions and polarizations.	106
A.1	Values of α and β for all targets.	113

A.2	Values of α and β for segmentation of ground range corrected targets.	114
B.1	Properties of I1.	115
B.2	Properties of I2.	116
B.3	Properties of I3.	116
B.4	Properties of I4.	117
B.5	Properties of I5.	117
B.6	Properties of I6.	118
B.7	Properties of I7.	118
B.8	Properties of I8.	119
B.9	Properties of I9.	119
B.10	Properties of I10.	120
C.1	Results from the pilot study [50].	122
C.2	PBR_{PS} for data set 1, using the method from the pilot study. . .	123
D.1	PBR_A and TBR_A for data set 2.	125
D.2	PBR_A and TBR_A for targets in data set 3.	126